Measurement of D^0, D^+, D^{*+} and D_s^+ Production Cross Sections in 920 GeV/c Proton-Nucleus Collisions with HERA-B

Samo Kupper and Marko Starič

May-2006 (updated 17th October 2006)

Abstract

The note presents a measurement of the open charm production in 920 GeV/c pA collisions. The analysis discussed in this note was carried out by the Ljubljana team, and includes measurements of the total and single differential cross sections σ, $d\sigma/dp_T^2$ and $d\sigma/dx_F$, the A-dependence of the cross sections and the leading to non-leading particle asymmetries for the production of D^0, D^+, D_s^+ and D^{*+} mesons.

Contents

1 Introduction

In this note we describe the open charm analysis performed by the Ljubljana group. We measured the production cross sections of the D^0, D^+, D_s^+ and D^{*+} mesons, reconstructed in the following decay channels:

$D^0 \rightarrow K^-\pi^+$

$D^+ \rightarrow K^-\pi^+\pi^+$

$D_s^+ \rightarrow \phi\pi^+ \rightarrow (K^-K^+)\pi^+$

$D^{*+} \rightarrow D^0\pi^+ \rightarrow (K^-\pi^+)\pi^+$

Throughout this note charge conjugate channels are implied. The results of the analysis include total and single differential cross sections σ, $d\sigma/dp_T^2$ and $d\sigma/dx_F$, the A-dependence of the cross sections and the leading to non-leading particle asymmetries.

The layout of this note is as follows. After reviewing the existing experimental data, we present the data sample and the data selection criteria. We then proceed by the determination of the cross sections, leading to non-leading particle asymmetries and the A-dependence of the cross sections. In the fifth chapter we present a measurement of the differential cross-sections and discuss the influence of the kinematical distributions on the total visible cross-sections. We then discuss various sources of systematical errors, present their estimation and determine correction factors for the final cross-section values. Finally, the results of the measurement are presented and discussed.

1.1 Existing experimental data

In the past twenty years several experiments published their measurements on open charm production cross sections in proton-nucleus collisions, covering the proton energy range from 250 GeV to 800 GeV. The experiments are summarized in Table 1. A more detailed overview is given in [1]. With only one exception (E789), these experiments covered the full forward hemisphere in phase space, but the number of collected D mesons is rather low.

Exp.	Target	Beam E_{lab} [GeV]	Phase space coverage	Events	
				D^0	D^+
E769	Be,Al,Cu,W	250	$x_F > -0.1$	136	159
NA16	liquid H_2	360	$x_F > -0.1$	5	10
NA27	liquid H_2	400	$x_F > -0.1$	98	119
E743	liquid H_2	800	$x_F > -0.1$	10	46
E653	emulsion	800	$x_F > -0.1$	108	18
E789	Be, Au	800	$0 < x_F < 0.08,\ p_T < 1.1 GeV/c$	>4000	

Table 1: Experiments measuring the production cross-sections of neutral and charged D mesons in p-A interactions. The table is taken from Ref.[1]

Experiments NA16, NA27 and E743 [2] [3] [4] used the high resolution hydrogen bubble chamber (LEBC) as a target and vertexing device, while tracking, momentum measurement and particle identification utilized a 40 meters long “EHS” spectrometer. They used a simple interaction trigger, provided by wire chambers placed just downstream of LEBC. The charm mesons were identified by their topology (displaced vertex), by observing the charge of the decaying particle and a given number of charged final state particles.

Experiment E653 [5] used a 1.47 cm long emulsion target followed by an 18-plane silicon vertex detector continued by a magnetic spectrometer. The trigger required an interaction in the target and a high p_T muon candidate, detected in the muon spectrometer. Cross-sections were obtained essentially on the basis of semi-muonic decays.

Experiment E769 [6] used a multifoil target, consisting of 250 μm thick Be, Al and Cu foils, as well as 100 μm thick W foils, spaced by 1.6 mm. In total, 26 target foils were used. The detector included an 11-plane silicon vertex detector, two analyzing magnets, drift and multi-wire proportional chambers for tracking, A segmented threshold Cherenkov counter for pion, kaon and proton identification, electromagnetic and hadron calorimeter and muon identification system. The trigger required the total transverse energy in the calorimeters to exceed 5.5 GeV. The charm mesons were identified in fully reconstructed decays to two or three charged final state particles. This experiment is the only one which measured D_s and Λ_c production in p-A collisions, but was able only to give confidence intervals for the cross-section.

Experiment E789 [7] used a thin strip target of Be or Au, 160 μm by 1.8 mm or 110 μm by 0.8 mm in cross section, and a 16-plane silicon vertex detector to measure the secondary vertices of D mesons. An on-line vertex processor selected events with secondary vertices at least 1.02 mm downstream of the target. The decay products were further analyzed by the spectrometer consisting of two magnets and tracking chambers, a ring-imaging Cherenkov detector, electromagnetic and hadronic calorimeters and a muon identification system. This experiment collected the largest open charm data sample, but measured only neutral D mesons. Unfortunately, their coverage of the phase space is rather small, causing a significant systematic uncertainty, when extrapolated to the full phase space, since the extrapolation is model dependent. E789 is the only experiment, which measured the nuclear dependence of the D meson production. Their result, $\alpha = 1.02 \pm 0.03 \pm 0.02$ justifies the assumption of linear dependence of the production cross-section on the atomic number of the target.

The experiments from Table 1 published D meson cross-sections for proton-nucleon collisions, assuming a linear dependence on target atomic number A: $\sigma_{pA} = \sigma_{pN} \cdot A$. Their results, scaled where needed to the full phase space and corrected for the present values of the branching ratios, are summarized in Table 2.

Exp.	Beam E_{lab} [GeV]	$\sigma(D^0)$ [μb/N]	$\sigma(D^+)$ [μb/N]	$\sigma(D^{*+})$ [μb/N]
E769	250	$12.0 \pm 2.7 \pm 1.1$	$6.6 \pm 0.8 \pm 0.6$	$3.8 \pm 1.3 \pm 0.4$
NA16	360	$20.4^{+15.8}_{-8.6}$	$10.6^{+4.8}_{-3.2}$	
NA27	400	18.3 ± 2.5	11.9 ± 1.5	9.2 ± 2.4
E743	800	$22^{+9}_{-7} \pm 5$	$26 \pm 4 \pm 6$	
E653	800	$39 \pm 3 \pm 12$	$31 \pm 9 \pm 13$	
E789	800	$17.7 \pm 0.9 \pm 3.3$		

Table 2: Existing data for D meson total production cross sections in p-A collisions for proton energies from 250 to 800 GeV.

To get the estimates for the cross-sections at the HERA-B energy, which are needed for the "blind" optimization of our analysis cuts, we fit the data points from Table 2. We found a simple parameterization for the energy dependence of the cross-section in Ref. [1]:

$$\sigma(\sqrt{s}) = p_0 \cdot (1 - \frac{p_1}{\sqrt{s}^{p_3}})^{p_2} \tag{1}$$

with $p_1 = 1.2$, $p_2 = 12$ and $p_3 = 0.35$ and only p_0 being free. Fig. 1 shows the data points together with results of the fits. Eq. 1 fits the D^+ and D^{*+} experimental data well, while for the D^0, the data point of E789 had to be excluded in order to get a good fit. * The cross sections extrapolated to the HERA proton energy are summarized in Table 3.

$\sigma(D^0)$	$\sigma(D^+)$	$\sigma(D^{*+})$
45 μb/N	31 μb/N	21 μb/N

Table 3: The cross-sections extrapolated to 920 GeV

Most of the experiments published also measurements of kinematical distributions in x_F and p_T. They typically used the parameterization

$$\frac{d^2N}{dx_F dp_T^2} \propto (1 - |x_F|)^n e^{-bp_T^2} \tag{2}$$

with the two free parameters n and b describing the shapes in x_F and p_T projections of the 2D distribution respectively. Since one could expect some energy dependence of the shapes, we summarize in Table 4 only the results of the three experiments at 800 GeV, closest to our energy. The p_T range of these experiments is relatively small. As one can see from their published distributions, shown in Fig. 2, the limitation for the first two experiments is due to low statistics. For completeness we also show in Fig. 3 the published x_F distributions of E653 and E743.

*One of the reasons for this discrepancy could be an underestimated systematic error due to the extrapolation from the very limited measured part of the phase space to the full phase space as required in the E789 experiment.

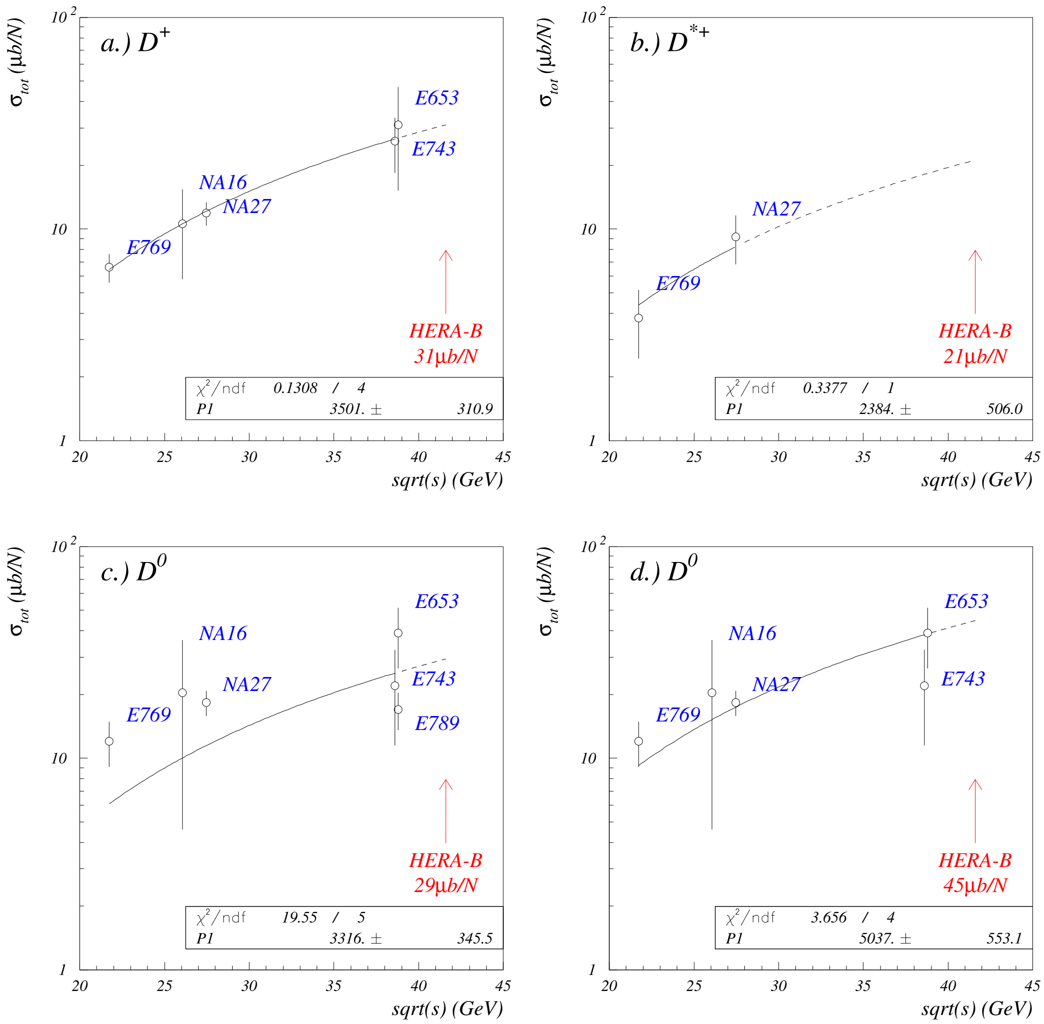

Figure 1: Energy dependence of the cross section for a) D^+, b) D^{*+}, c) D^0 and d) D^0 with the E789 data point excluded from the fit

Exp	events	effective range		n	b
E653	146	$-0.15 < x_F < 0.3$	$p_T^2 < 4$	$6.9^{+1.9}_{-1.8}$	$0.84^{+0.10}_{-0.08}$
E743	31	$-0.1 < x_F < 0.4$	$p_T^2 < 3.5$	8.6 ± 2.0	0.8 ± 0.2
E789	$\sim$2200	$0 < x_F < 0.08$	$p_T^2 < 1.2$		0.91 ± 0.12
Average				7.7 ± 1.4	0.86 ± 0.07

Table 4: Measurements of parameters n and b of Eq. 2 at 800 GeV

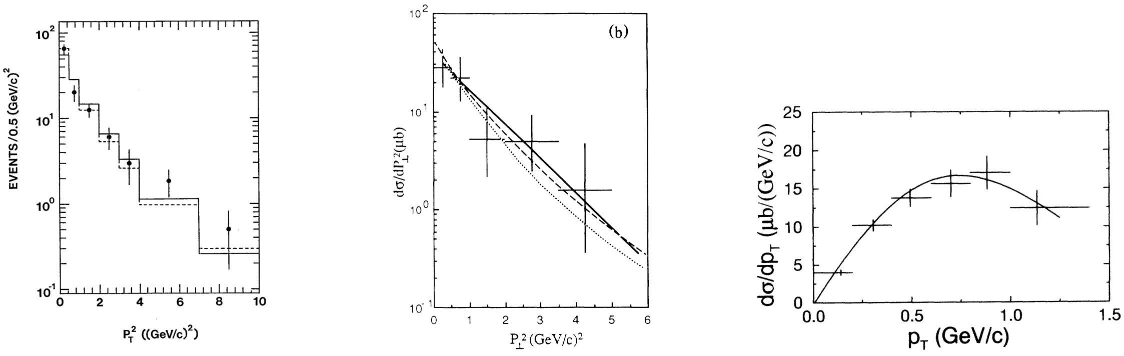

E653 E743 E789

Figure 2: Published measurements of the p_T distributions at 800 GeV.

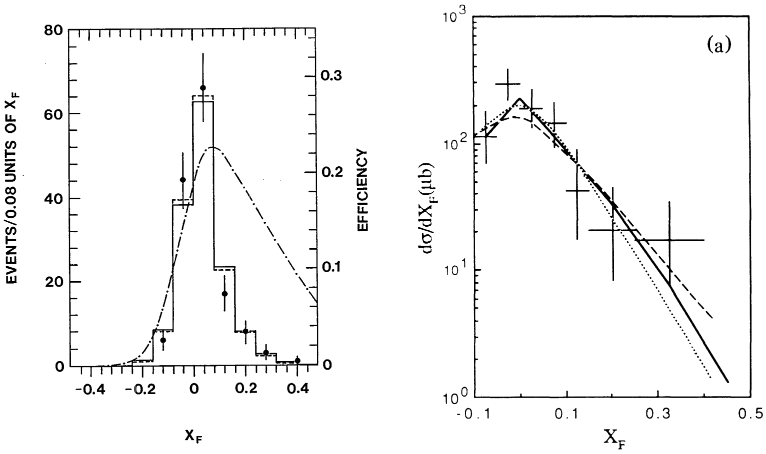

E653 E743

Figure 3: Published measurements of the x_F distributions at 800 GeV.

The p_T^2 distribution with the highest statistics was collected by the E769 experiment at 250 GeV, covering the range of $p_T^2 < 10(GeV/c)^2$. They found that the simple exponential in Eq. 2 did not fit the measurement well and that the b parameter was sensitive to the fit range used. They tried a form, inspired by QCD, with two free parameters, α and β, and with a mass of $m_c = 1.5GeV$:

$$\frac{dN}{dp_T^2} \propto (\alpha m_c^2 + p_t^2)^{-\beta} \tag{3}$$

and found it to fit their measured distribution well over the entire p_T range.

20166	20168	20169	20170	20171	20172	20195	20198
20199	20339	20340	20341	20388	20464	20466	20467
20468	20469	20474	20478	20479	20480	20507	20653
20663	20668	20669	20670	20671	20675	20676	20677
20678	20679	20680	20682	20693	20695	20700	20701
20703	20704	20705	20706	20711	20723	20724	20725
20726	20728	20734	20735	20736	20737	20738	20739
20740	20742	20743	20744	20746	20747	20749	20764
20766	20767	20768	20769	20770	20771	20772	20773

Table 5: Run numbers of the real data used for our analysis

2 Data sample

Our analysis is based on the minimum bias sample, recorded during November and December 2002 and reconstructed with the “reprocessing 5”. It consists of about 180 million events, distributed among four different targets operated in a single wire mode: below1 (C), inner1 (W), below2 (Ti), and inner2 (C). The working frame for the analysis code was ARTE-04-01-r5.

2.1 Run selection

In our analysis we used all runs except the first three (19170, 19179, 19180) from the list of runs for analysis purposes by J. Spengler. The list is accessible by following the link on the Minimum Bias working group web page. Run numbers of the runs used in this analysis are given in Table 5 and a summary of the data statistics and the integrated luminosities is given in Table 6. Runs with the numbers from 20653 to 20773 which were taken during a short period in December (from 9 to 21 December) represent almost 80% of the statistics used in this analysis. This sample is referred to as the *Golden MB data*.

2.2 Monte Carlo samples

For the efficiency determination and for the cut optimizations we used the Monte Carlo simulated data. The D mesons were generated with the PYTHIA 5.7 generator, and the FRITIOF generator was used for the rest of the proton interaction inside the nucleus. The detector response was generated with the standard HBGEANT package. A realistic detector geometry description was used. Detector resolutions and maskings were simulated to the best possible knowledge. During the reconstruction, the signal MC events were mixed with inelastic MC events to account for a Poissonian distribution of the number of interactions. The average measurement rates were well simulated by the mixing. The same ARTE code as for the real data

Target	A	events [$\times 10^6$]		$\mathcal{L}_i$ [μb^{-1}]	
		full sample	Golden sample	full sample	Golden sample
b1 (C)	12.01	69.5	65.1	276.565	257.246
i1 (W)	183.84	67.6	54.8	35.884	28.478
b2 (Ti)	47.88	24.7	22.9	30.904	28.697
i2 (C)	12.01	20.5	0	97.970	0
Sum		182	143	12575	9698

Table 6: Summary of the data statistics and the integrated luminosities used for our analysis. In the last row a weighted sum $\sum A_i \mathcal{L}_i$ is given for the integrated luminosity.

MC sample	No of runs	run numbers (run09_)
$D^+ \to K^-\pi^+\pi^+$	8	1633, 1683 - 1689
$D^0 \to K^-\pi^+$	8	1692 - 1699
$D_s^+ \to \phi\pi^+ \to (K^-K^+)\pi^+$	8	1712 - 1719
$D^{*+} \to D^0\pi^+ \to (K^-\pi^+)\pi^+$	8	1702 - 1709
$c\bar{c}$	16	411, 413-416, 418-428

Table 7: Run numbers of the MC sample used for our analysis

was also used for the reconstruction of the MC.

In our analysis we used the latest MC samples which are tuned at the generator level to get a better agreement of event multiplicities with the real data. Besides the signal MC, we also used $c\bar{c}$ Monte Carlo for the description of the charm background in the D^0 analysis. This MC sample was generated with the older generator settings and does not describe the event multiplicities well.

The information about the MC samples is accessible at the Minimum Bias working group web page. In Table 7 we provide the run numbers of MC used in our analysis and in Table 8 a summary of the MC statistics.

$D^+ \to K^-\pi^+\pi^+$			
wire	Material	No. of decays	$-0.15 < x_F < 0.05$
b1	C	355110	162786
i1	W	452737	207036
b2	Ti	224748	103270
i2	C	205168	94505
Total		1237763	567597
$D^0 \to K^-\pi^+$			
wire	Material	No. of decays	$-0.15 < x_F < 0.05$
b1	C	369638	168980
i1	W	424867	191012
b2	Ti	207661	94150
i2	C	207146	94040
Total		1209312	548182
$D_s^+ \to \phi\pi^+ \to (K^-K^+)\pi^+$			
wire	Material	No. of decays	$-0.15 < x_F < 0.05$
b1	C	137051	64983
i1	W	164110	78770
b2	Ti	83308	39853
i2	C	52599	26746
Total		437168	210352
$D^{*+} \to D^0\pi^+ \to (K^-\pi^+)\pi^+$			
wire	Material	No. of decays	$-0.15 < x_F < 0.05$
b1	C	445166	196224
i1	W	664394	293158
b2	Ti	234493	103450
i2	C	225131	99019
Total		1569184	691851
$c\bar{c}$ events			
wire	Material	No. of events	
b1	C	1106452	
i1	W	2137418	
b2	Ti	702533	
i2	C	738840	
Total		4685243	

Table 8: Summary of the Monte Carlo statistics used for our analysis.

3 Data selection

At the HERA-B energy the charm production cross section is expected to be 2-3 orders of magnitude smaller than the inelastic cross section. Taking into account also relatively small branching ratios for the decay modes into 2 or 3 charged final state particles and a limited acceptance of our detector, one could expect huge backgrounds, if strict data selection criteria are not used. Particle identification, for example, is not sufficient to extract signals. However, the large boost of the center-of-mass system of HERA-B ($\gamma = 22$), causing D mesons to decay several millimeters from the target, combined with a good vertex resolution ($\approx$ 0.5 mm) provides a possibility to distinguish D meson candidates from the particles originating at the primary interaction point. The data selection thus required a detached secondary vertex, formed by tracks not coming from the primary interaction point as well as the identification of kaons and pions.

3.1 Reconstruction of D mesons

Since the detached vertex is required for the ground state D mesons only events with a least one reconstructed primary vertex were selected. The reconstruction was done in the following steps:

Track selection The reconstructed charged tracks were taken from the RTRA table with the following requirements:

- the track is a reconstructed charged track ($fit = 0$)
- the track has enough hits in the VDS and MAIN trackers ($hsi \geq 5$, $hin + hout \geq 10$)
- the track is not a clone ($cmp : uniqpc$ flag is set)
- the track momentum is smaller than 250 GeV/c
- the $\chi^2/n.d.f$ of a track fit is below 10

Particle identification From the selected tracks, lists of positive and negative pions and kaons were formed with the following selection criteria for the RICH likelihoods:

- for pions in D^0, D^+ and D_s^+ reconstruction: $lre + lrmu + lrpi > 0.05$
- for slow pion in D^{*+} reconstruction: no PID was required
- for kaons in D^0 reconstruction: $lrk > 0.5$
- for kaons in D^+ and D_s^+ reconstruction: $lrk > 0.33$

Primary vertex Primary vertices were taken from the RVER table without any requirement. Since the proton interaction point is inside the target wire, which is known with much better accuracy than the primary vertex in the coordinates transverse to the wire, we replaced those two with the target position from the GTAR table. The replacement is done also for the corresponding diagonal elements of the primary vertex covariance matrix, which were replaced with the wire dimensions divided by $\sqrt{12}$. The non diagonal elements of the covariance matrix were set to 0.

Combinations The lists were combined into D^0, D^+ and D_s^+ candidates providing that the tracks forming a combination were different and that each combination was taken only once. The invariant masses of the combinations were calculated and only the candidates with invariant mass in the interval of ± 0.5 GeV around the D meson nominal mass were taken in the further analysis steps. For the D_s^+ candidates, an additional cut was applied on the invariant mass of the K^+K^- pairs: only the candidates with $m(K^+, K^-)$ in the interval of $\pm$20MeV around the ϕ nominal mass were accepted. The D^{*+} candidates were combined from the D^0 candidates and the slow pions after the vertex fit to D^0. Both combinations were made, the right sign (D^0, π^+) and the wrong sign $(\bar{D}^0, \pi^+)$. The wrong sign combinations were used for the combinatorial background estimation in the right sign channel.

Vertex fit A common vertex of each track combination was fitted with the Grover vertexing package. The unconstrained fit was used. The combination was accepted, if the fit was successful and if its χ^2 probability was greater than 0.1%. To reduce the cpu time in the next steps, a cut on the distance *significance* † of the vertex to the wire was applied: the candidate was accepted, if its vertex position was at least 4 sigma downstream the wire. The wire position was taken from the GTAR table.

Primary vertex association The candidate was then associated with the primary vertex. In case of events with multiple reconstructed primary vertices, the one with the smallest impact parameter significance of the D meson candidate was chosen.

Primary vertex refit To avoid a possible bias in the primary vertex position due to tracks from the D meson candidate, the tracks from the D meson candidate were excluded from the associated primary vertex and the primary vertex was refitted. The geometrical fit from Grover, function *GeoFit* was used, since the original fit was also done with this function (see the Grover code).

†With the *significance* we mean the quantity divided by its estimated error given by the covariance matrix

3.2 Analysis cuts

To select the most appropriate variables for discriminating the processes under study (signal events) from the background events, and to determine the optimal cut values in these variables, two data samples were used. For the signal events, we have used MC generated events, while for the background the side bands in the corresponding invariant mass were used, as described in the next section.

The main source of the background arises from combinations of particles emerging from the primary interaction point. This background can be reduced by the following three requirements: (1) the secondary vertex is detached, (2) the tracks forming the secondary vertex did not come from the primary interaction point and (3) the D meson candidate came from the primary interaction point. To fulfill these criteria we used the cuts on the following variables:

- $d(D)$ the distance significance of the secondary vertex to the primary interaction point given by the associated primary vertex
- $b(K), b(\pi)$ the impact parameter significance of a pion or a kaon to the associated primary vertex
- $b(D)$ the impact parameter significance of a D meson candidate to the associated primary vertex

Here the significance of a certain variable refers to the value of the variable divided by its error as estimated in the reconstruction of the event.

Due to high interaction rates more than one primary vertex was found in about 10% of events. In this case, a good detached vertex could be fitted also from two or three tracks coming from different primary vertices. To suppress this kind of background, we used the impact parameter significance to the closest primary vertex $b_m(K)$ or $b_m(\pi)$ instead of impact parameter significance to the associated primary vertex $b(K)$ or $b(\pi)$ [‡].

We found that for the three body decay of D^+, a more effective cut than the cuts on single impact parameter significances of daughter tracks is the cut on their product $b_m(K)b_m(\pi_1)b_m(\pi_2)$. The distributions for the background in real data sidebands and for the MC signal are shown in Fig. 4. This cut also includes implicitly a cut on the distance significance of a secondary vertex, thus the latter is not needed. For two body decays the situation is opposite.

By studying the correlation between the cut on the product of impact parameter significances and the proper life time we found that we could improve the signal significance, if we apply also a cut of the form: $\sqrt[3]{b_m(K)b_m(\pi_1)b_m(\pi_1)} > 4(t - t_0)$, as shown in Fig. 5 by the red line. The proper life time t is in units of the D meson mean life time.

The cuts on the p_T of daughter tracks were also studied and we found, that the cut on the product of the D meson momentum and the transverse momenta of daughter tracks p_{pT} =

[‡]Note that for events with exactly one primary vertex, b and b_m are the same

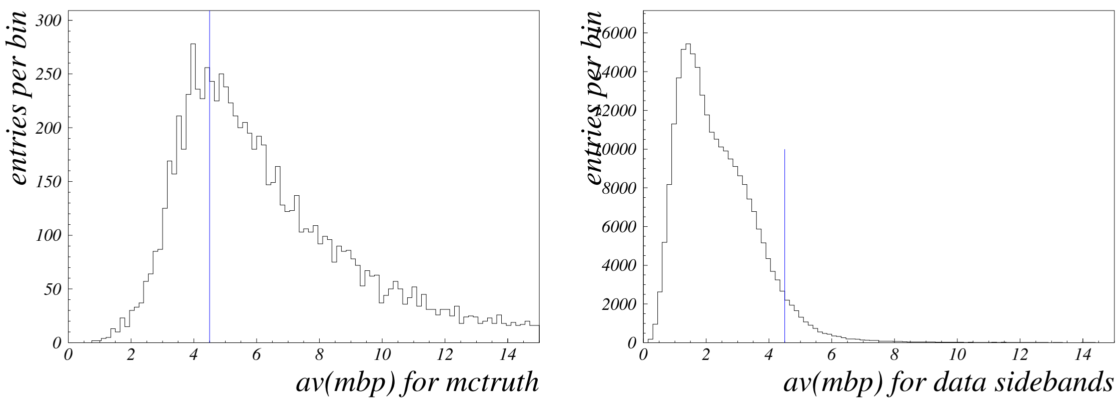

(a) Monte Carlo signal

(b) Real data side bands

Figure 4: Distribution of $\sqrt[3]{b_m(K)b_m(\pi_1)b_m(\pi_1)}$ for Monte Carlo signal (left) and background from real data sidebands (right). The blue line indicates a possible cut.

$p(D)\Pi_i p_T(i)$ is more effective than the cuts on single variables. This kind of cut, when used in addition to the detached vertex cuts, improves the signal significance, but also changes the shape of the background at invariant masses below the signal peak. It is harder to find the appropriate function to describe the shape of the background. The comparison of the p_{pT} distributions of the MC signal and the background in the real data side bands is shown in Fig. 6.

3.3 Optimization of analysis cuts

For each decay mode the optimal cuts were determined by maximizing the signal significance $S/\sqrt{S+B}$ with S being the number of signal events and B the number of background events in a $\pm 3\sigma$ window centered at the D meson nominal mass (signal window). The signal S was taken from Monte Carlo and was scaled to the luminosity of real data by dividing it by the scaling constant f:

$$S = \frac{S_{MC}}{f} \tag{4}$$

The number of the Monte Carlo signal events S_{MC} surviving the cuts was determined by counting the events in the signal window and subtracting the counts in the side bands. The scaling factor f was calculated by:

$$f = \frac{N_{MC}}{N_{data}} \tag{5}$$

where N_{MC} is the number of generated decays in the Monte Carlo and $N_{data} = \sigma Br \sum A_i \mathcal{L}_i$ is the estimation for the number of decays in the real data. For the latter we obtained the estimation for the production cross sections σ from fits to the published D meson cross sections, Table 3. For the D_s^+ we estimated the cross section by taking, according to a theoretical prediction [9], 20% of the sum of D^0 and D^+ cross sections from Table 3.

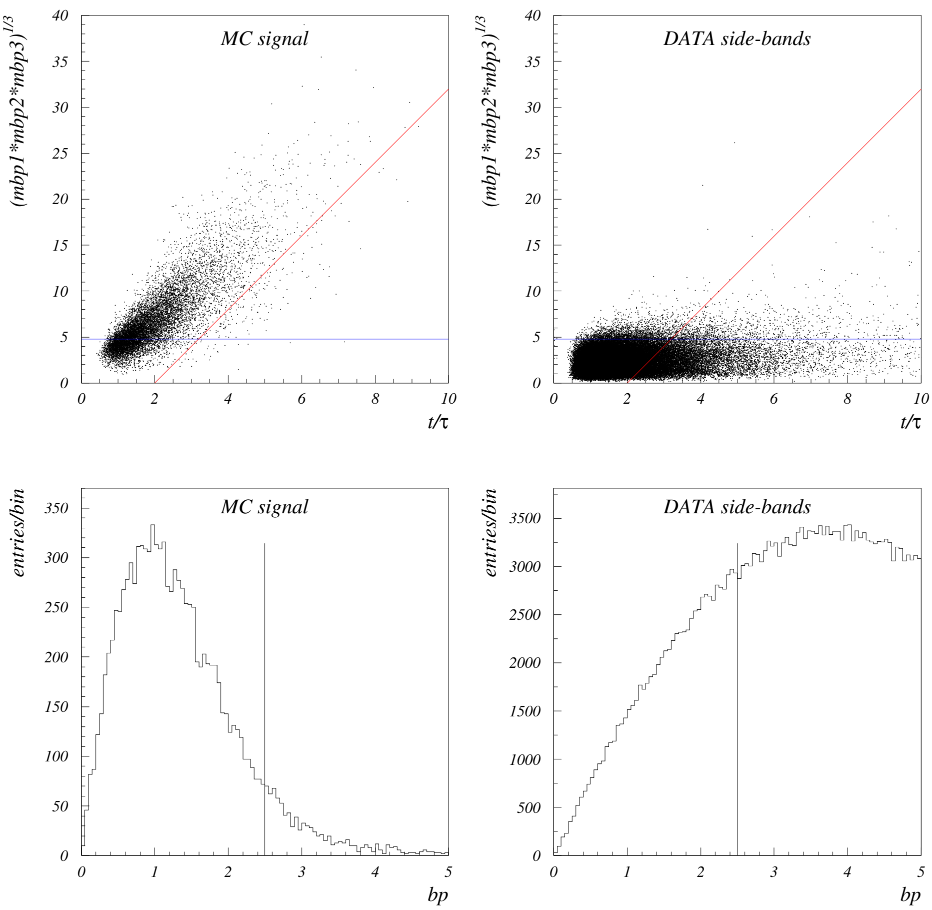

Figure 5: The correlations between geometrical average of the impact parameter significances of the D^+ daughter tracks $\sqrt[3]{b_m(K)b_m(\pi_1)b_m(\pi_1)}$ and the proper life time t/τ (top). The distributions of the D^+ impact parameter significance $b(D)$ (bottom). On the left for Monte Carlo signal and on the right for real data side bands. Possible cuts are indicated by the lines.

In the case of ground state D mesons, the number of background events B was estimated from the real data side bands. A linear extrapolation was used. For the D_s^+ a mass region $|\Delta m_{D^+}| < 50 MeV$, where a peak of the decay $D^+ \to \phi\pi^+$ is expected, was excluded from side bands. To reduce the sensitivity to statistical fluctuations, the side bands were chosen larger than the signal window, thus another scale factor s was introduced, equal to the ratio between the widths of the side band and the signal windows. Similar to eq. 4:

$$B = \frac{B_{sb}}{s} \tag{6}$$

with B_{sb} being the event counts in the side bands.

In the case of the D^{*+} the wrong sign combinations from real data were used to estimate the background in the signal window. As is usually done for this decay, the signal was reconstructed in the mass difference $q = m(K, \pi, \pi_{slow}) - m(K, \pi) - m_\pi$ rather than in the invariant mass of the K, π, π_{slow} combinations. The window sizes and the scaling factors are given in Table 9

Two methods have been used to find the maximum:

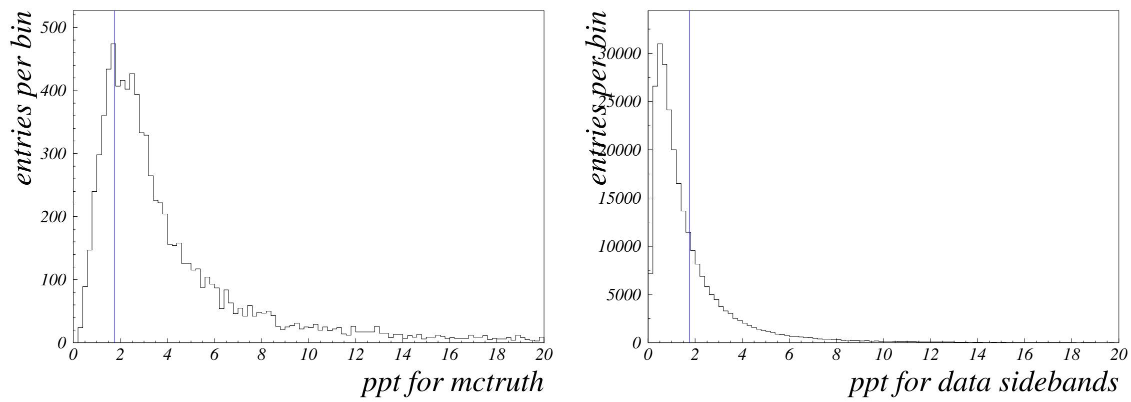

(a) Monte Carlo signal

(b) Data side bands

Figure 6: Distribution of the p_{pT} for the Monte Carlo signal (left) and for the background from real data sidebands (right). The lines indicate a possible cut.

meson	signal window [MeV]	side bands [MeV]	f	s
D^0	$\lvert\Delta m\rvert < 75$	$75 < \lvert\Delta m\rvert < 150$	56	1
D^+	$\lvert\Delta m\rvert < 50$	$50 < \lvert\Delta m\rvert < 300$	35	5
D_s^+	$\lvert\Delta m\rvert < 45$	$45 < \lvert\Delta m\rvert < 450$	129	7.9
D^{*+}	$\lvert\Delta q\rvert < 2.5$		232	1

Table 9: Window sizes and scale factors used in the cut optimization.

Iterative method A loop over cuts is performed. The cuts have been treated as independent and are optimized sequentially. The optimum for a given cut is searched in a reasonable interval by calculating the signal significance in 1000 points. For each cut, the cut value with the highest significance is used in the further calculations. This procedure runs iteratively. Typically three iterations are sufficient to find the maximum.

3D Optimization This procedure has been used for the optimization of three cuts. First, a sufficiently large region of interest is chosen. This region is divided into a matrix of $10\times10\times10$ equally spaced points and the signal significance for each point is calculated. Then the position of the maximum is determined. In the second step, the region of interest is decreased by factor of 5 in each dimension and centered at the position of maximum from the first step, and the maximum finding procedure is repeated.

The analysis cuts are summarized in Table 10. Not all have been optimized: the particle identification, because there is a small discrepancy between data and MC, the cuts on the invariant mass of the intermediate state, because the peak widths are narrower in the MC and the cosine of the angle between K and π in the rest frame of the ϕ. The latter one was chosen so that it cuts $1/2$ of the background while keeping $7/8$ of the signal [§].

In addition to the analysis cuts, the cut on our accessible phase space was also applied. As it is shown in section 5.3 our acceptance in p_T is not limited and the limitation comes only from the acceptance in x_F. We defined the visible range in x_F by the interval, where the acceptance is larger than approximately 10% of its maximum value. Our visible range is:

$$-0.15 < x_F < 0.05 \tag{7}$$

After applying the selection cuts the remaining data was scanned for events with more then one D-meson candidate. For D^0, D^+ and D_s^+ the candidate with the largest decay distance significance $d(D)$ was kept. For the D^{*+} first the candidates were selected, where the intermediate D^0 had the largest decay distance significance. If more combinations used the same D^0 candidate in combination with a different π_{slow} than the candidate with the highest vertex probability was kept.

[§]Because ϕ is a vector while initial and final state particles are scalars, the distribution is proportional to $\cos^2\theta_{K\pi}$.

$D^0 \to K^-\pi^+$	$D^+ \to K^-\pi^+\pi^+$
not optimized	
$pid(K) > 0.5$ $pid(\pi) > 0.05$	$pid(K) > 0.33$ $pid(\pi) > 0.05$
optimized	
$d(D^0) > 6.1$ $b(D^0) < 2.4$ $b_m(K) > 3.4$ $b_m(\pi) > 3.7$	$b(D^+) < 2.5$ $b_m(K)b_m(\pi_1)b_m(\pi_2) > 146$ $\sqrt[3]{b_m(K)b_m(\pi_1)b_m(\pi_2)} > 4(t-t_0),\ t_0 = 1.68$

$D_s^+ \to \phi\pi^+ \to K^-K^+\pi^+$	$D^{*+} \to D^0\pi^+ \to K^-\pi^+\pi^+$
not optimized	
$pid(K) > 0.33$ $pid(\pi) > 0.05$ $\|\Delta m_\phi\| < 10MeV$ $\|\cos\theta_\phi\| > 0.5$	$pid(K) > 0.5$ $pid(\pi) > 0.05$ $pid(\pi_{slow}) \geq 0$ $\|\Delta m_{D^0}\| < 75MeV$
optimized	
$d(D_s^+) > 5.3$ $b(D_s^+) < 2.11$ $b_m(K^-)b_m(K^+)b_m(\pi) > 28.7$ $\sqrt{b_m(\phi)b_m(\pi)} > 0.75(t-t_0),\ t_0 = 1.0$	$b(D^0) < 2.4$ $b_m(K) > 2.1$ $b_m(\pi) > 1.7$ $p_{pT}(D^0) > 17.7$

Table 10: Analysis cuts

3.4 Data signals

The invariant mass distributions that result from combining the particles and applying the selection criteria discussed above are shown in Figs. 8, 9, 10 and 11. Besides the total data sample, the invariant mass distributions for the following subsamples are also presented: particle and anti-particle, the C, W and Ti target materials and the golden and non golden data samples.

The signals were fitted by a Gaussian function while for the background different shapes were used since the shape depends on the type of the D meson. For the D^+ and D_s^+ the background was fitted by an exponential function. The background in the D^0 reconstruction is more complicated and consists of a combinatorial part, fitted by an exponential and a background from partially reconstructed charm decays. This background is appearing left to the D^0 peak. We took the shape of the charm background from the $c\bar{c}$ Monte Carlo after applying the analysis cuts to the events. The histogram was smoothed and normalized to its sum equal to 1 (Fig. 7). The normalization constant was a free parameter in the fit.

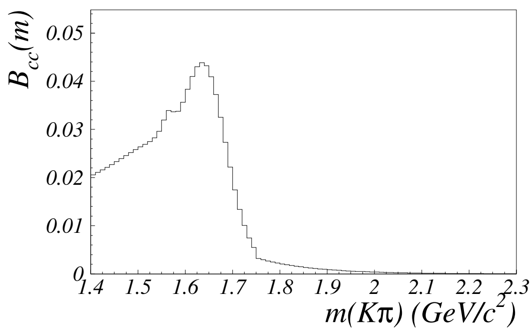

Figure 7: The shape of the $c\bar{c}$ background

In the D_s^+ invariant mass distribution also the Cabibbo suppressed decay of $D^+ \to \phi\pi^+$ is seen (the peak left to the D_s^+ peak). We included this peak in the fit function as an additional Gaussian with its position and its width fixed and only the normalization as a free parameter. The position and the width were fixed to the values from the fit to $D^+ \to K^-\pi^+\pi^+$ invariant mass distribution.

The background in the D^{*+} reconstruction was parameterized as $a(q^{1/2} + bq^{3/2})$ with parameters a and b being free in the fit to the total data sample. In the fits to subsamples, the shape was fixed by taking the value of b from the fit to total data sample and only the normalization parameter a was left free.

To ensure the stability of the fitting procedure, the subsamples of all D meson invariant mass distributions were fitted with a fixed signal position and width, both taken from the fit to total data samples.

The fitted positions and widths are summarized in Table 11. The peak positions are within one standard deviation from the corresponding PDG value, with the exception of D_s^+, which deviates by the two sigmas. Fits to Monte Carlo signals show a bit larger deviations and in the opposite direction compared to the real data. The widths of the signal peaks are for about 30%

	DATA		MC		PDG
meson	m_0 [MeV]	σ_m [MeV]	m_0 [MeV]	σ_m [MeV]	mass [MeV]
D^0	1863±2	21.4±2	1868±0.2	17.0±0.2	1865
D^+	1869±2	17.4±2	1872±0.2	13.8±0.2	1869
D_s^+	1961±4	10.8±4	1971±0.4	12.2±0.4	1969
	q_0 [MeV]	σ_q [MeV]	q_0 [MeV]	σ_q [MeV]	Δmass [MeV]
D^{*+}	6.0±0.2	1.0±0.2	5.99±0.01	0.68±0.01	5.85

Table 11: The fitted positions and widths of the signal peaks in real data and Monte Carlo. For comparison, the PDG value is also given.

sample	D^0	D^+	D_s^+	D^{*+}
total	174.8±16.8	148.2±15.6	11.7±4.0	61.3±13.0
particle	75.9±10.9	54.9±9.4	5.3±2.9	21.0±6.6
anti-particle	99.0±11.9	92.8±11.3	7.2±3.0	40.6±8.3
C	66.1±9.6	52.9±8.4	3.9±2.3	26.6±6.4
W	92.3±11.7	78.8±10.9	7.9±3.4	24.8±7.5
Ti	17.4±5.7	16.7±5.3	0.6±1.0	9.6±4.0
gold	133.7±14.1	116.5±13.1	8.7±3.7	55.6±9.9
non gold	41.2±7.8	31.7±6.8	3.4±2.0	6.2±3.9

Table 12: Number of reconstructed D mesons in the real data.

larger when compared to the Monte Carlo. It becomes true also for the D_s^+ signal, if we take the large error into account. Similar discrepancies were found also in the other HERA-B analyses (J/ψ, K_s).

The numbers of reconstructed D mesons are summarized in Table 12. In total we reconstructed 175 D^0, 148 D^+, 12 D_s^+ and 61D^{*+} decays. Also the signals in all subsamples were found and successfully fitted.

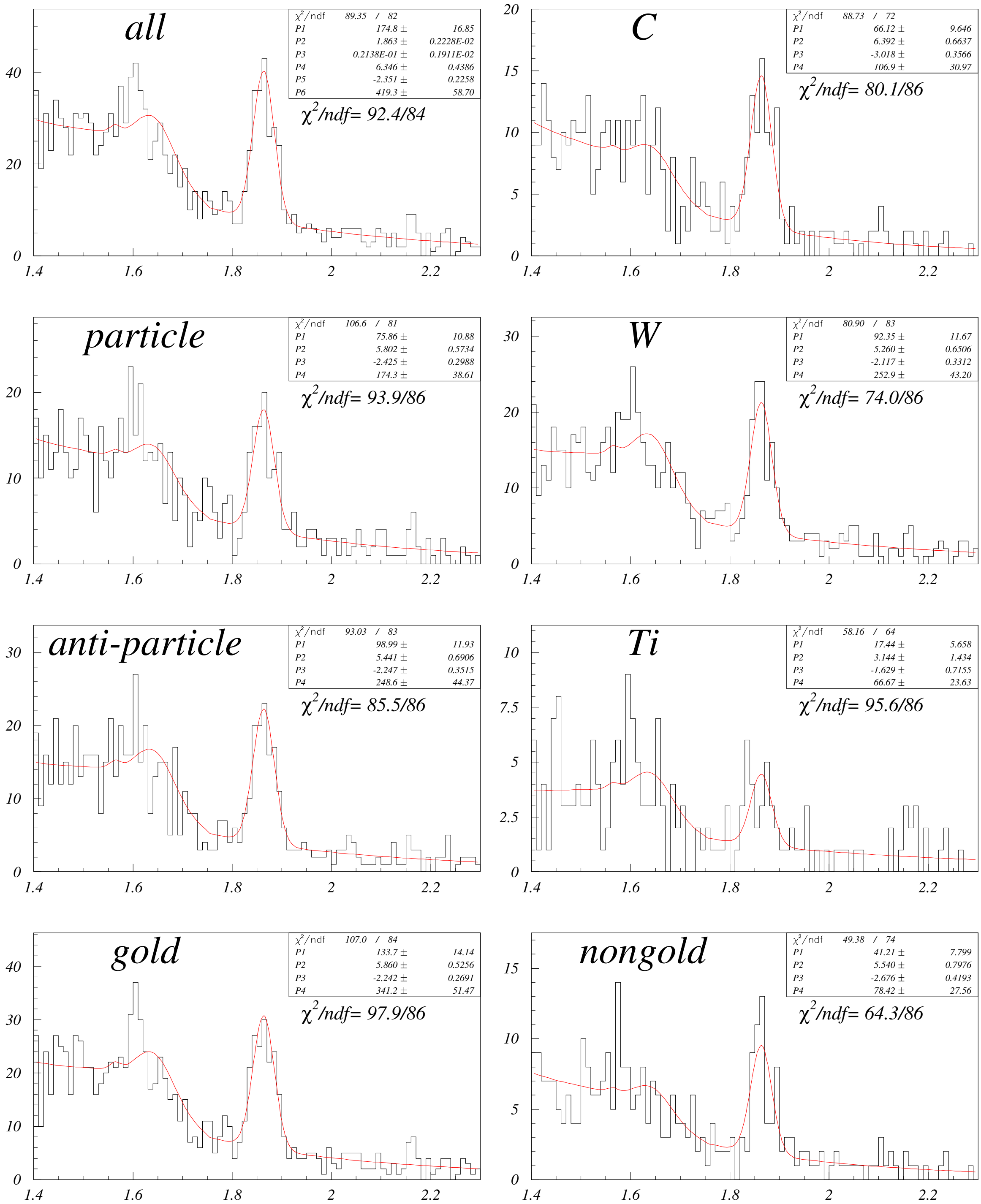

Figure 8: Invariant mass distributions for $D^0 \rightarrow K^-\pi^+$ in the real data for total sample (all) and for seven subsamples. The subsamples were fitted with the peak position and width fixed from the fit to the total sample. Below the statistics box the Pearson's χ^2 of the fit is printed.

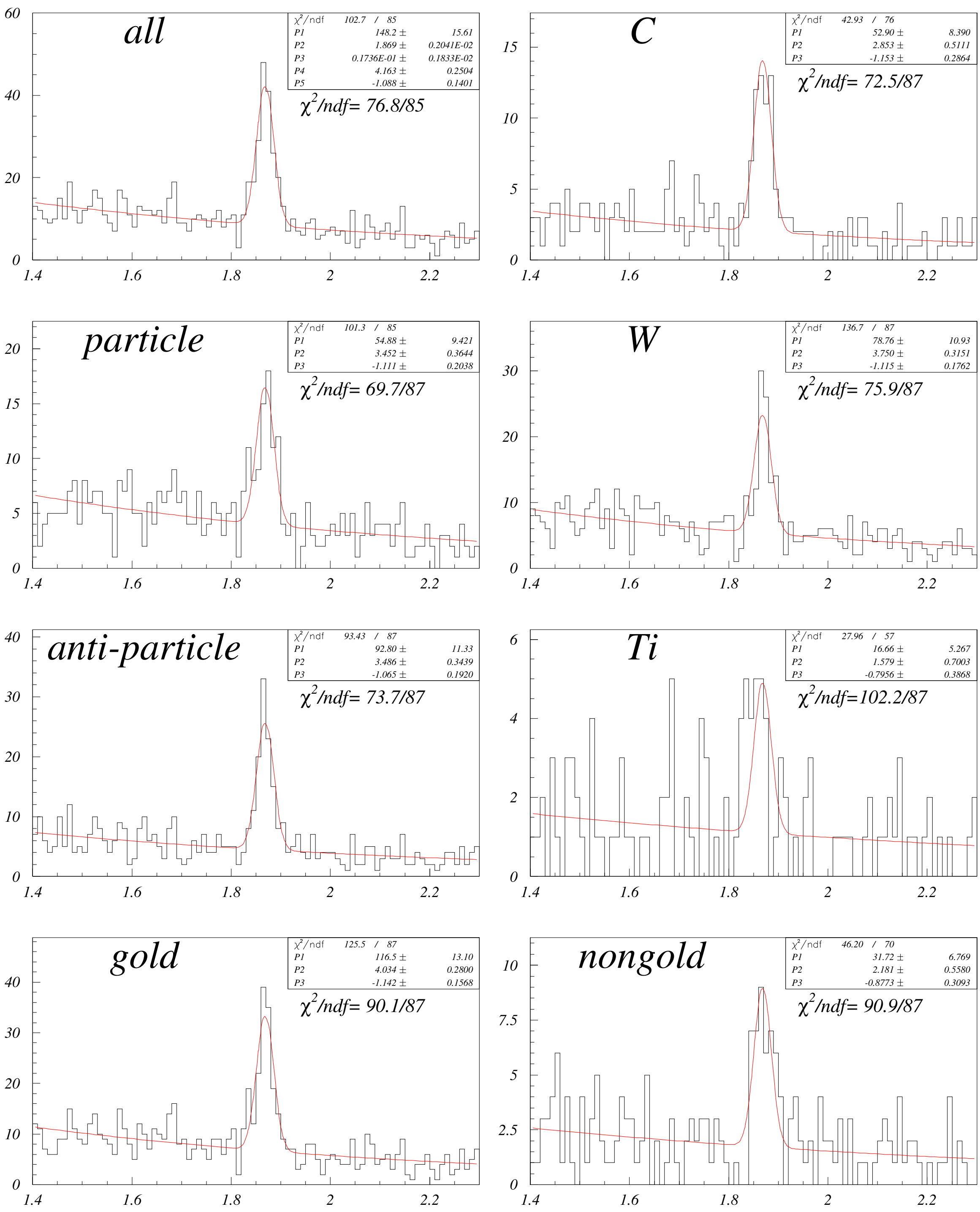

Figure 9: Invariant mass distributions for $D^+ \to K^-\pi^+\pi^+$ in the real data for total sample (all) and for seven subsamples. The subsamples were fitted with the peak position and width fixed from the fit to the total sample. Below the statistics box the Pearson's χ^2 of the fit is printed.

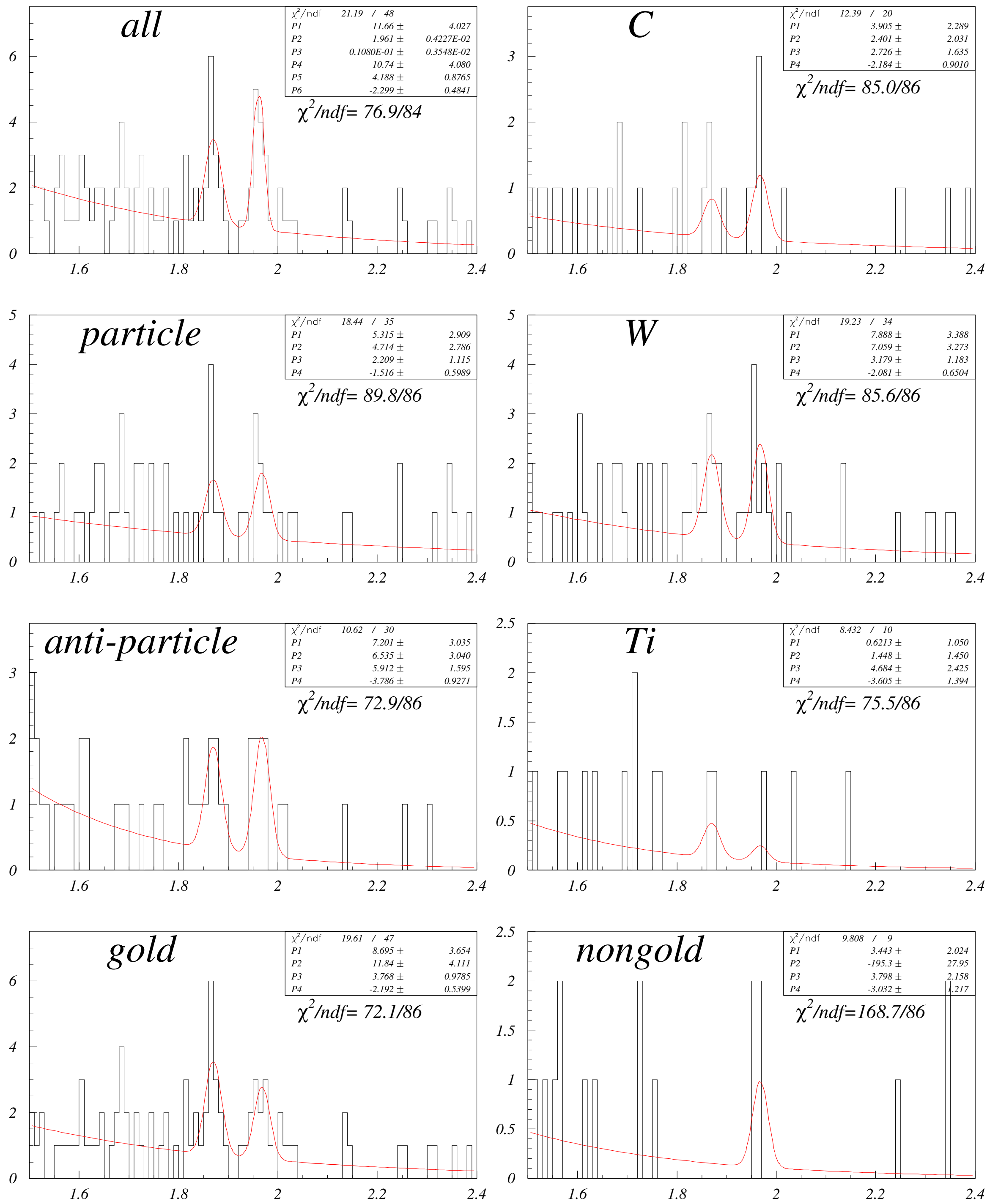

Figure 10: Invariant mass distributions for $D_s^+ \to \phi\pi^+ \to (K^-K^+)\pi^+$ in the real data for total sample (all) and for seven subsamples. Besides the D_s^+ peak at 1.96 GeV also the D^+ peak at 1.87 GeV is seen, corresponding to the Cabibbo suppressed decay $D^+ \to \phi\pi^+$. The subsamples were fitted with the peak position and width fixed from the fit to the total sample. Below the statistics box the Pearson's χ^2 of the fit is printed.

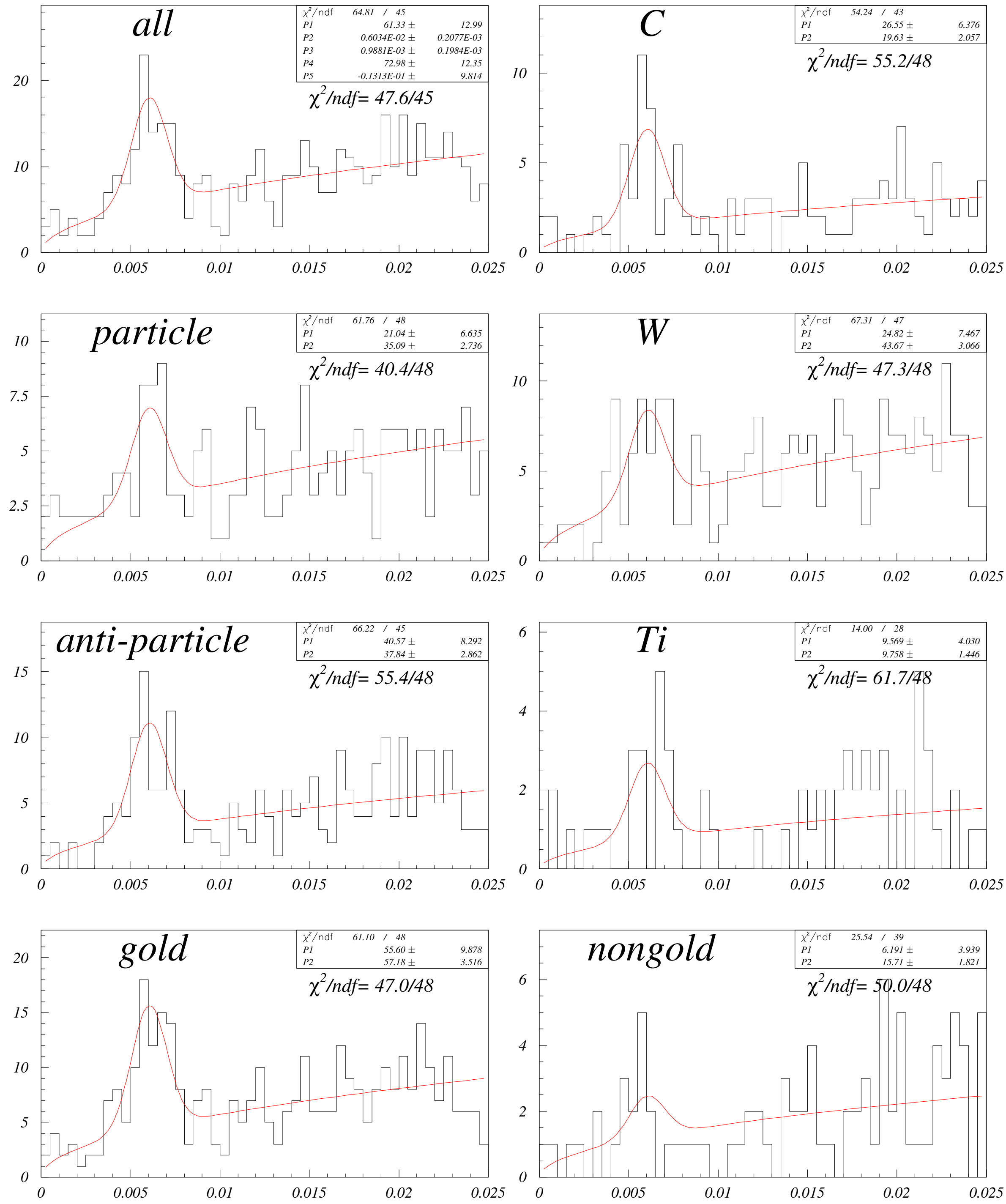

Figure 11: Invariant mass differences for $D^{*+} \rightarrow D^0\pi^+ \rightarrow (K^-\pi^+)\pi^+$ in the real data for total sample (all) and for seven subsamples. The subsamples were fitted with the peak position and width and with background shape fixed from the fit to the total sample. Below the statistics box the Pearson's χ^2 of the fit is printed.

3.5 D meson life times

For the signal consistency checks we measured the D meson proper time distributions. We checked, if the acceptance corrected distributions are exponential and if the fitted life times are in agreement with the PDG values. We used a simultaneous likelihood fit of events in the signal window and in the side bands. The side bands were chosen of the same size as the signal window. The assumption was, that the sidebands contain background events only, while the signal window contains signal and background events. The shape of the signal was parameterized as

$$S(t) = (\frac{N_D}{\tau_D} \cdot e^{-t/\tau_D}) \cdot \epsilon(t) \tag{8}$$

and the shape of the background as

$$B(t) = (\frac{N_{bg}}{\tau_{bg}} \cdot e^{-t/\tau_{bg}} + C) \cdot \epsilon(t) \tag{9}$$

where $\epsilon(t)$ describes the acceptance of the D meson as a function of proper time t and N_D, τ_D, N_{bg} and τ_{bg} being free parameters of the fit. The constant C was set to zero for D^+ and D_s^+ fits, while in case of the D^0 life time fit, it was a free parameter. We assumed the same acceptance both for signal and background events and exponential distribution of proper time also for the background.

The acceptance was determined from the Monte Carlo separately for each target wire and particle anti-particle species, then averaged over particle/anti-particle and over the wires as explained in section 4.2. The acceptances are plotted in Fig. 12.

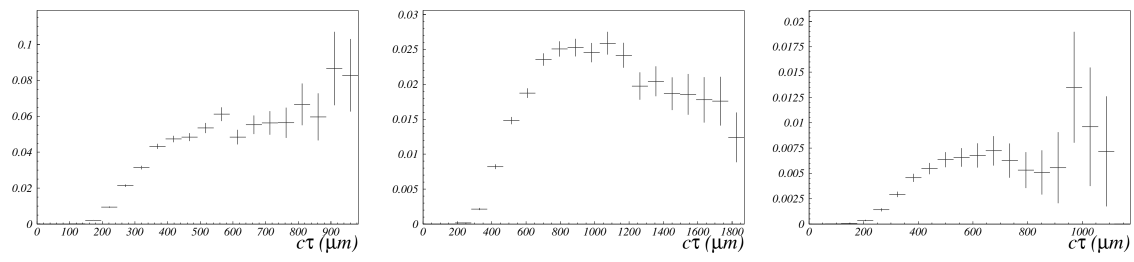

(a) D^0 (b) D^+ (c) D_s^+

Figure 12: Acceptance in proper life time for (a) D^0, (b) D^+, (c) D_s^+.

We fitted simultaneously the signal window distribution with $S(t) + B(t)$ and the sidebands distribution with $B(t)$. The number of free parameters was four in cases of D^+ and D_s^+ and five for D^0. The results of fits are shown in Figs. 13, 14 and 15. Four histograms are shown in each figure: at the top the acceptance uncorrected distributions for signal window and for side bands and at the bottom the acceptance corrected distributions for the signal (=signal window with side

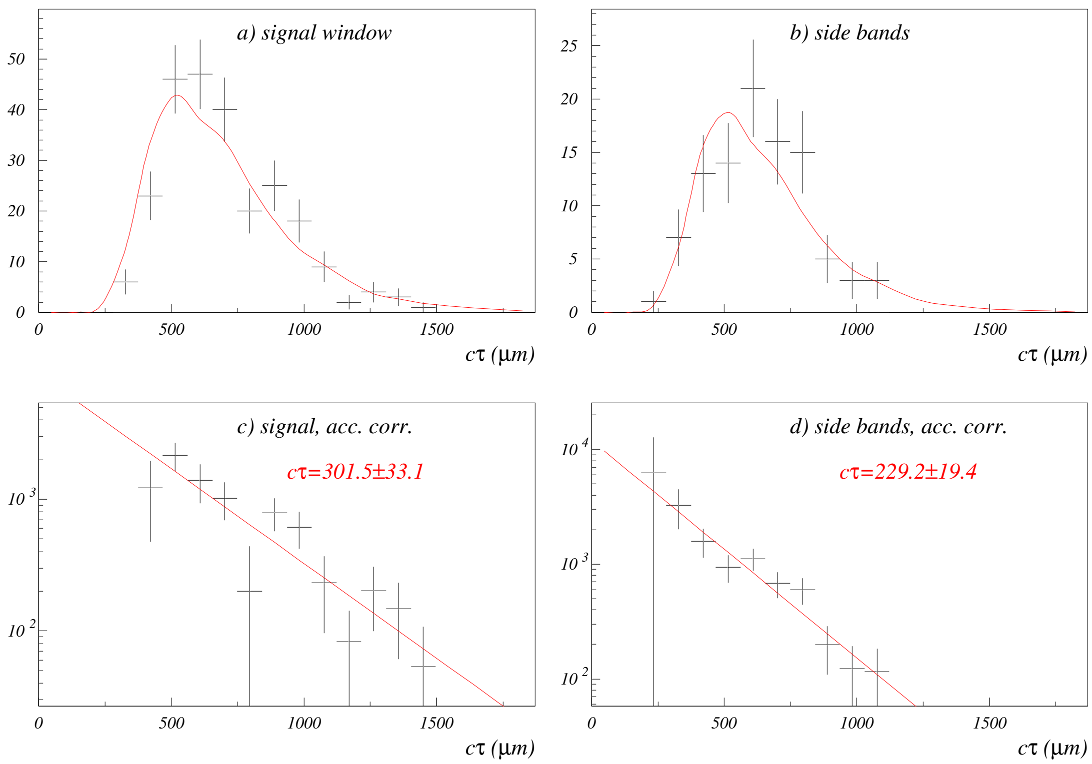

Figure 13: Simultaneous likelihood fit of the D^+ proper time distributions

meson	measured $c\tau$ [μm]	$\chi^2/n.d.f$	PDG $c\tau$ [μm]
D^+	302 ± 33	36/19	311.8
D^0	120 ± 13	36/24	122.9
D_s	165 ± 52	6.2/ 7	149.9

Table 13: Measured D meson life times

bands subtracted) and the background (=side bands). The acceptance corrected distributions for the signals (bottom left plots) are in a good agreement with the exponential distribution.

Our measurement of the life times, the χ^2 of the simultaneous fit and the PDG value of the life times are summarized in Table 13. The results for all three mesons are in a good agreement with the PDG values.

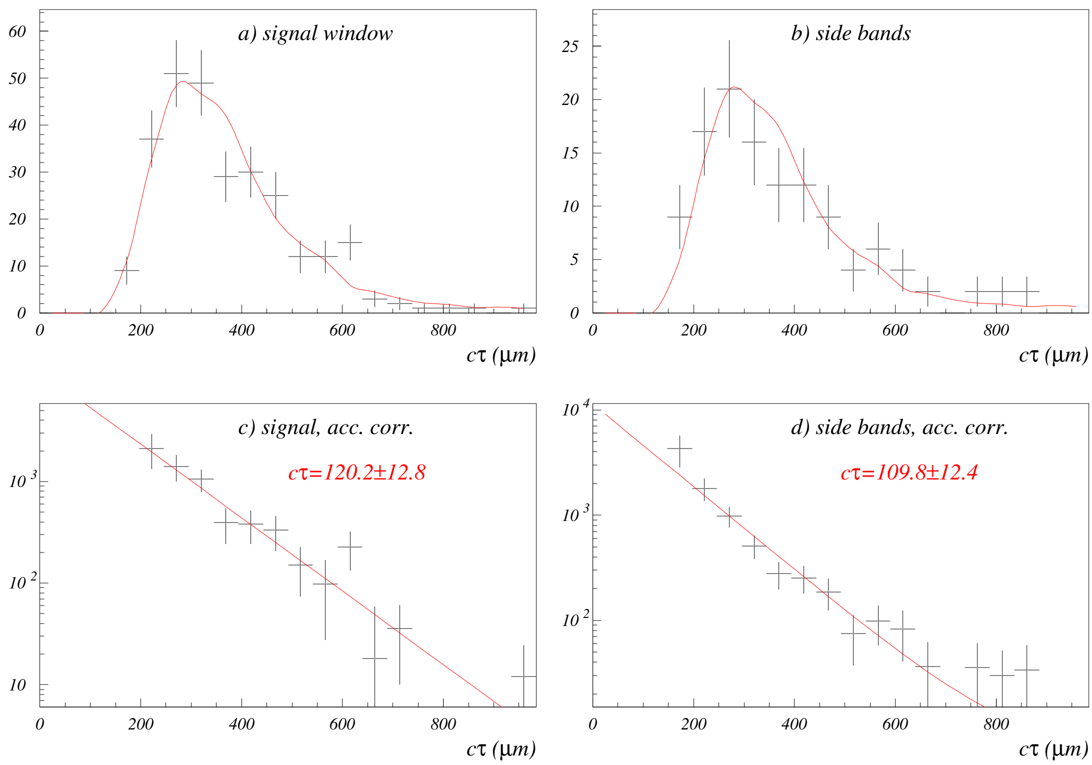

Figure 14: Simultaneous likelihood fit of the D^0 proper time distributions

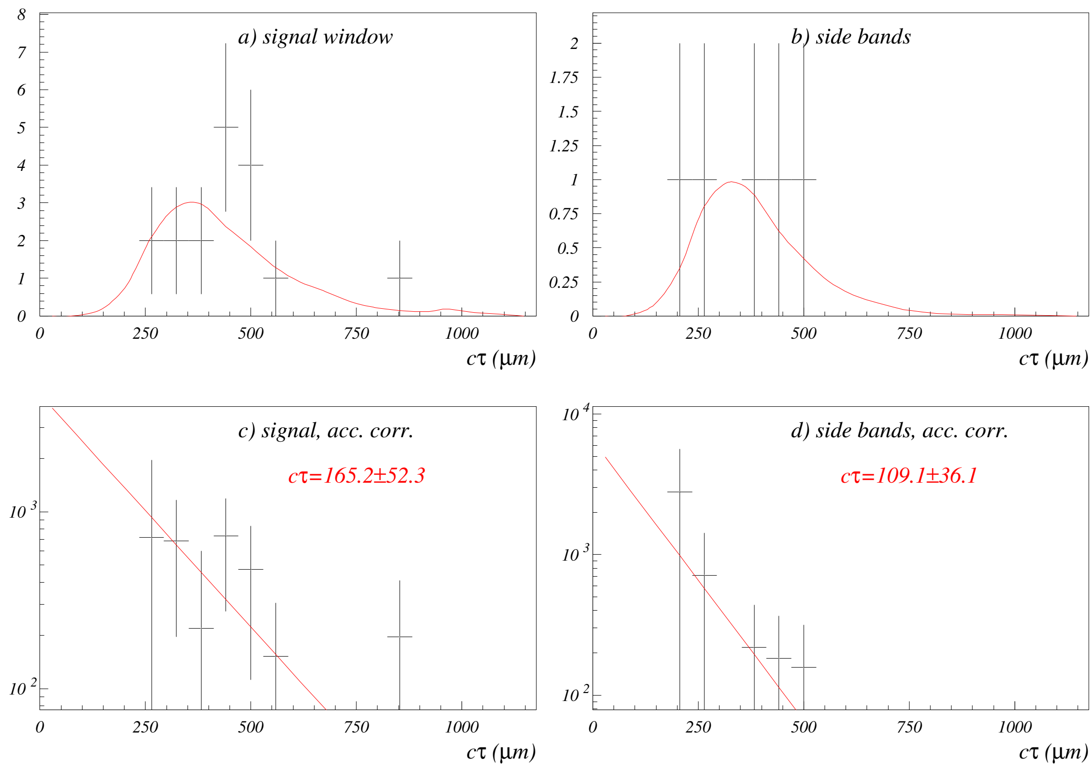

Figure 15: Simultaneous likelihood fit of the D_s^+ proper time distributions

3.6 Other consistency checks

The D_s^+ and D^{*+} are reconstructed in the decays via intermediate states ϕ and D^0 respectively. Intermediate states should be visible in the corresponding invariant mass distributions, when the signal region in the initial state invariant mass distribution is selected and the fit to the intermediate state invariant mass distribution should give the number of events consistent with the number in the initial state peak¶. The invariant mass distributions are shown in Fig. 16. Both intermediate states are well seen.

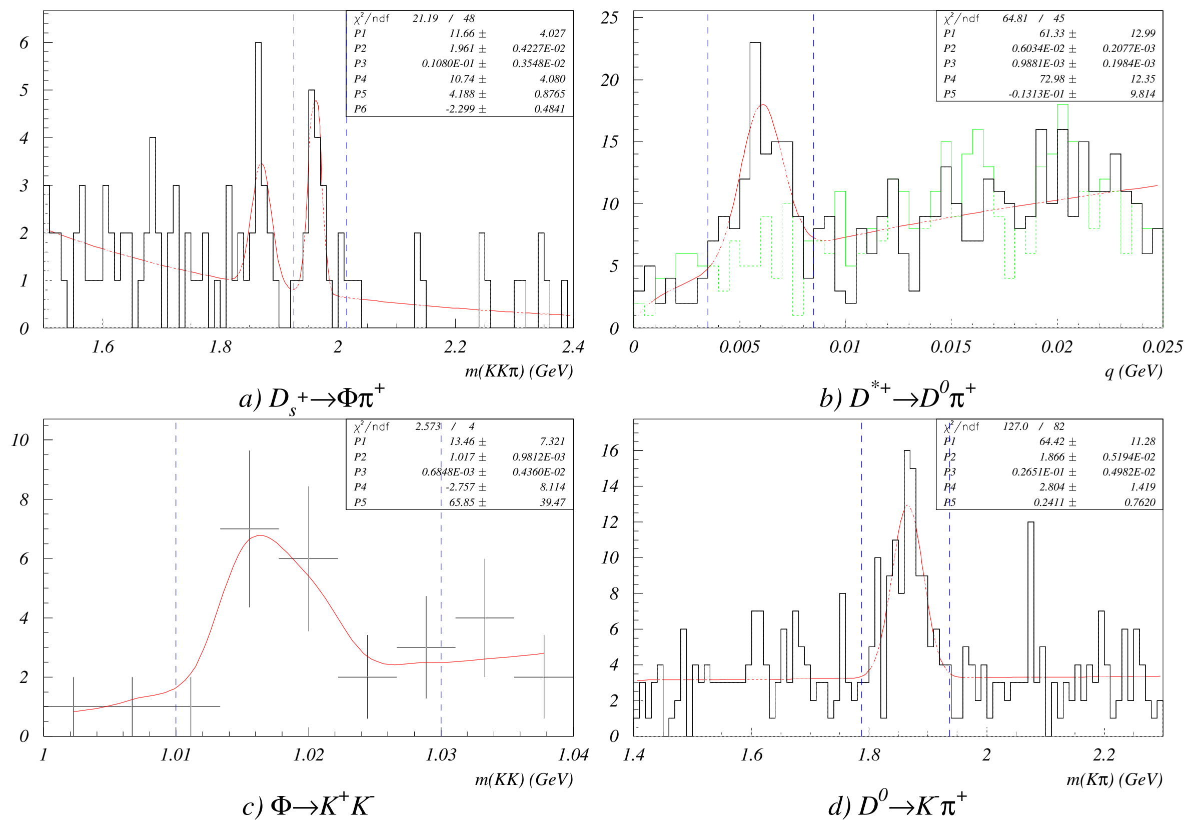

Figure 16: Invariant mass distributions for initial (top) and intermediate states (bottom): (a) $D_s^+ \to \phi\pi^+$, (b) $D^{*+} \to D^0\pi^+$, (c) $\phi \to K^-K^+$, events within D_s^+ peak and (d) $D^0 \to K^-\pi^+$, events within D^{*+} peak. With vertical dashed lines the signal regions used for the complementary plots are marked. In (b) the wrong sign combinations $(\bar{D}^0, \pi^+)$ are also plotted (in green).

In the case of D_s^+ the fit gives 13.5 $\pm$ 7.3 decays $\phi \to K^+K^-$, while in the D_s^+ peak we have 11.7$\pm$4.0 events. The numbers are in a good agreement. We fitted the ϕ invariant mass with a Bright-Wigner equation convoluted with a Gaussian plus a background of the form $a \cdot \sqrt{m - 2m_K} + b \cdot (m - 2m_K)$ where m_K is the kaon mass. The position of the Bright-Wigner

¶It could be slightly larger, since a fraction of the background in the initial state signal region is due to random combinations of the intermediate state and a pion from some other sources equation and the width of the Gaussian were also free parameters of the fit.

We've got a good agreement also for the D^{*+}: 64.4±11.3 events in the D^0 peak and 61.3±12.9 events in the D^{*+} peak. The D^0 background was fitted with a linear function.

Two other checks were done for the D_s^+ signal: the angular distribution of pions with respect to kaons in the rest frame of the ϕ and the consistency of the $D^+ \to \phi\pi^+$ peak. The angular distribution is shown in Fig. 17. It agrees well with the theoretically required $\cos^2\theta_{K\pi}$ dependence. Similarly good agreement we found also for the D^+ peak. The data points were obtained by fitting the invariant mass distribution of $K^-\pi^+\pi^+$ combinations in three bins of $|cos\theta_{K\pi}|$. The position and the width of the signal were fixed.

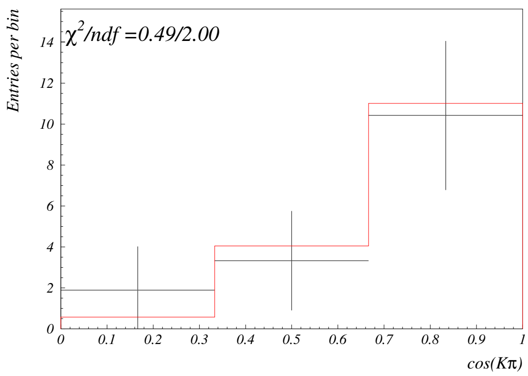

Figure 17: The angular distribution of pions with respect to kaons in the rest frame of ϕ for D_s^+ signal events. The $\cos^2\theta_{K\pi}$ dependence of the $dN/d\cos\theta_{K\pi}$ distribution is plotted in red and is normalized to the same number of events as the data. The χ^2 is also given.

The consistency of the $D^+ \to \phi\pi^+$ signal was tested by estimating the number of reconstructed decays from our measured D^+ cross section in the $D^+ \to K^-\pi^+\pi^+$ decay channel given in Table 17 of section 4.3. The efficiency was determined from the $c\bar{c}$ Monte Carlo and amounts to 0.99±0.25%. By taking the branching fraction of 0.31±0.03% from the PDG and the luminosities from Table 6 we estimated the number to 4.2±1.2. The fit to data gives 10.7±4.1, which is in reasonable agreement with the estimated number (the χ^2 probability is 13%).

4 Total visible production cross sections

In this section the total visible production cross sections are evaluated from the selected D meson data samples, discussed in the previous section. The efficiencies are determined from the signal Monte Carlo, without any corrections to the generated kinematical distributions. The corrections are made later in section 7, after discussion of the kinematical distributions.

4.1 Basic formulae

The visible cross section per nucleus, i.e. the cross section measured in our visible range of $-0.15 < x_F < 0.05$ is given by

$$\Delta\sigma_{pA} = \frac{N_i}{Br \cdot \epsilon_i \cdot \mathcal{L}_i} \tag{10}$$

where N_i is the number of reconstructed D mesons, ϵ_i and $\mathcal{L}_i$ are the efficiency and integrated luminosity for a particular target and Br the branching ratio for a specific decay channel. The cross section for D meson production on a nuclear target of atomic number A is parameterized as

$$\sigma_{pA} = \sigma_{pN} \cdot A^{\alpha} \tag{11}$$

Since our statistics of the D meson data samples is relatively poor, we fitted invariant mass distributions for the total D meson data samples and extracted the production cross sections per nucleon $\Delta\sigma_{pN}$ in the following way. From eqs. 10 and 11 we get for the D meson yield of the target i

$$N_i = Br \cdot \epsilon_i \cdot \mathcal{L}_i \cdot \Delta\sigma_{pN} \cdot A_i^{\alpha} \tag{12}$$

By summing Eq. 12 over all targets and solving it for the production cross section we get

$$\Delta\sigma_{pN} = \frac{N}{Br \cdot \sum_i \epsilon_i \mathcal{L}_i A_i^{\alpha}} \tag{13}$$

where $N = \sum_i N_i$ is the measured D meson yield of the total data sample. The sum in the denominator of Eq. 13 can be rewritten by introducing the average efficiency ϵ, defined by the weighted sum:

$$\epsilon = \sum_i p_i \epsilon_i \quad , \qquad p_i = \frac{A_i^{\alpha} \mathcal{L}_i}{\sum_k A_k^{\alpha} \mathcal{L}_k} \tag{14}$$

Then the Eq. 13 reads

$$\Delta\sigma_{pN} = \frac{N}{Br \cdot \epsilon \cdot \sum_i \mathcal{L}_i A_i^{\alpha}} \tag{15}$$

Alternatively, we can calculate the cross sections per nucleon individually for each target and then calculate the weighted average by using measurement errors. It can be shown (see ref. [8])

that Eq. 15 is a result of the Poissonian likelihood fit to the target subsamples while the weighted average corresponds to the least square fit. In this respect the results obtained with Eq. 15 are statistically more correct than the weighted average.

Since there is no experimental clue for nuclear effects, we assumed a linear A dependence of the production cross sections and set $\alpha = 1$ in eqs. 14 and 15.

4.2 Efficiency determination

The efficiencies were determined from the signal Monte Carlo. The events were processed with the same code and analyzed using the same analysis cuts as for the real data. The efficiencies were calculated separately for particles and anti-particles and for each target wire by

$$\epsilon_i^{+/-} = \frac{n_i^{+/-}}{N_i^{+/-}} \tag{16}$$

where $n_i^{+/-}$ and $N_i^{+/-}$ are the numbers of reconstructed and generated decays respectively in our visible x_F range for the target wire i and particle (+) or anti-particle (-) . The generated decays were counted by identifying the D meson decays in the MTRA table, using the ARTE relations between mother and daughter particles. Thus the numbers given in Table 8 are for a few percent larger that the numbers of generated events, because they include also the decays of the opposite particles into the same channel.

The reconstructed decays were counted by fitting the invariant mass distributions with Gaussian for the signal and a constant (D^0, D_s^+) or a linear function (D^+) for the background. The background in Monte Carlo is much smaller than in the real data. The fit range was limited to 150 MeV around the nominal mass to reduce the systematics due to background parameterization. The exception was D^{*+} where we used the same background parameterization as in the real data and fitted in the same range. For all distributions a maximum likelihood fit was used.

The efficiencies per targets are summarized in Table 14. The efficiencies for the total sample and the subsamples, summarized in Table 15, were calculated from the efficiencies per targets (Table 14) by using eqs. 14 with $\alpha = 1$ and the luminosity data from Table 6. For the samples, where the charge state of a meson was not distinguished, we took the average of charge conjugate efficiencies for the efficiency of a target ϵ_i in Eq. 14

$$\epsilon_i = \frac{\epsilon_i^+ + \epsilon_i^-}{2} \tag{17}$$

4.3 Cross sections

Visible cross sections per nucleon $\Delta\sigma_{pN}$ were calculated with Eq. 15, by setting $\alpha = 1$, from the number of reconstructed events N given in Table 12, known branching fractions Br (Table 16), reconstruction efficiencies ϵ (Table 15) and integrated luminosities $\mathcal{L}_i$ summed over nucleons

meson	b1 (C)	i1 (W)	b2 (Ti)	i2 (C)
D^0	1.324±0.045	1.363±0.040	1.385±0.060	1.265±0.056
$\bar{D}^0$	1.336±0.037	1.452±0.039	1.609±0.055	1.354±0.051
D^+	1.121±0.042	1.139±0.038	1.288±0.058	1.089±0.055
D^-	1.171±0.037	1.151±0.033	1.299±0.048	1.144±0.047
D_s^+	0.432±0.040	0.412±0.038	0.381±0.051	0.537±0.092
D_s^-	0.400±0.033	0.365±0.028	0.469±0.045	0.352±0.043
D^{*+}	1.345±0.042	1.318±0.035	1.379±0.059	1.293±0.058
D^{*-}	1.560±0.038	1.575±0.032	1.735±0.056	1.488±0.053

Table 14: Reconstruction efficiencies in % for individual targets

sample	D^0	D^+	D_s^+	D^{*+}
total	1.388±0.017	1.160±0.016	0.405±0.015	1.456±0.016
particle	1.346±0.025	1.147±0.024	0.426±0.025	1.330±0.023
anti-particle	1.431±0.024	1.173±0.021	0.385±0.018	1.581±0.021
C	1.325±0.024	1.138±0.023	0.423±0.023	1.436±0.023
W	1.407±0.028	1.145±0.025	0.389±0.023	1.447±0.024
Ti	1.497±0.041	1.294±0.038	0.425±0.034	1.557±0.041
golden	1.396±0.019	1.166±0.017	0.403±0.016	1.464±0.017
non golden	1.364±0.021	1.139±0.019	0.415±0.024	1.428±0.020

Table 15: Reconstruction efficiencies in % for different data samples

Branching fractions [%]			
$D^0 \to K^-\pi^+$	$D^+ \to K^-\pi^+\pi^+$	$D_s^+ \to \phi_{\to K^+K^-}\pi^+$	$D^{*+} \to D^0_{\to K^-\pi^+}\pi^+$
3.80±0.07	9.51±0.34	2.16±0.28	2.57±0.05

Table 16: Branching fractions (PDG 2006)

$\Delta\sigma_{pN}$ [μb/N]				
sample	D^0	D^+	D_s^+	D^{*+}
total	26.3±2.5	10.7±1.1	10.6±3.7	13.0±2.8
particle	11.8±1.7	4.0±0.7	4.6±2.5	4.9±1.5
anti-particle	14.5±1.7	6.6±0.8	6.9±2.9	7.9±1.6
C	29.2±4.3	10.9±1.7	9.5±5.6	16.0±3.8
W	26.2±3.3	11.0±1.5	14.2±6.1	10.1±3.0
Ti	20.7±6.7	9.2±2.9	4.6±7.7	16.2±6.8
gold	26.0±2.7	10.8±1.2	10.3±4.3	15.2±2.7
non gold	27.6±5.2	10.2±2.2	13.3±7.8	5.9±3.7

Table 17: Visible production cross sections per nucleon (uncorrected) with statistical errors from the fits to real data invariant mass distributions.

$\sum_i \mathcal{L}_i A_i$ (Table 6). The results are summarized in Table 17. In Fig. 18 we plot the cross sections of five subsamples (C, Ti, W, golden and non golden) and compare them to the cross section of the total sample, represented with the dashed line. With the exception of the non golden subsample of D^{*+}, which cross section is for the two standard deviations smaller, all other subsample cross sections agree within one standard deviation with the cross section of the total sample.

4.4 Leading to non-leading particle asymmetries

The leading particle is defined as the one which has a light quark in common with the beam particle. Thus the leading particles are anti-D mesons $\bar{D}^0$, D^- and D^{*-}, while both charge conjugates of the D_s^+ are, according to the definition, the non-leading particles. The leading to non-leading particle asymmetry is defined as a relative difference of the cross sections

$$A = \frac{\sigma_{LP} - \sigma_{nonLP}}{\sigma_{LP} + \sigma_{nonLP}} \tag{18}$$

The asymmetry depends on the fragmentation mechanism. The PYTHIA version with the settings used for the $c\bar{c}$ Monte Carlo predicts slightly positive values for the asymmetry in the full phase space (9% for D^0 and 6% for D^+ or D^{*+}). PYTHIA also generates different shapes of the x_F distributions: narrower for anti-particles and wider for particles (see section 5.2). Thus the asymmetries measured in a limited x_F range are shifted to even more positive values. Note that for D_s^+, where we only have non-leading particles, we use the same prescription for the above formula, and take its anti-particle D_s^- to be the leading particle. In this case the asymmetry is larger and negative (-25%), and reduces to -6% for the limited x_F range.

Our measurements determined from the cross sections given in Table 17 and PYTHIA predictions are summarized in Table 18. The predictions and the measurements are in a good agree-

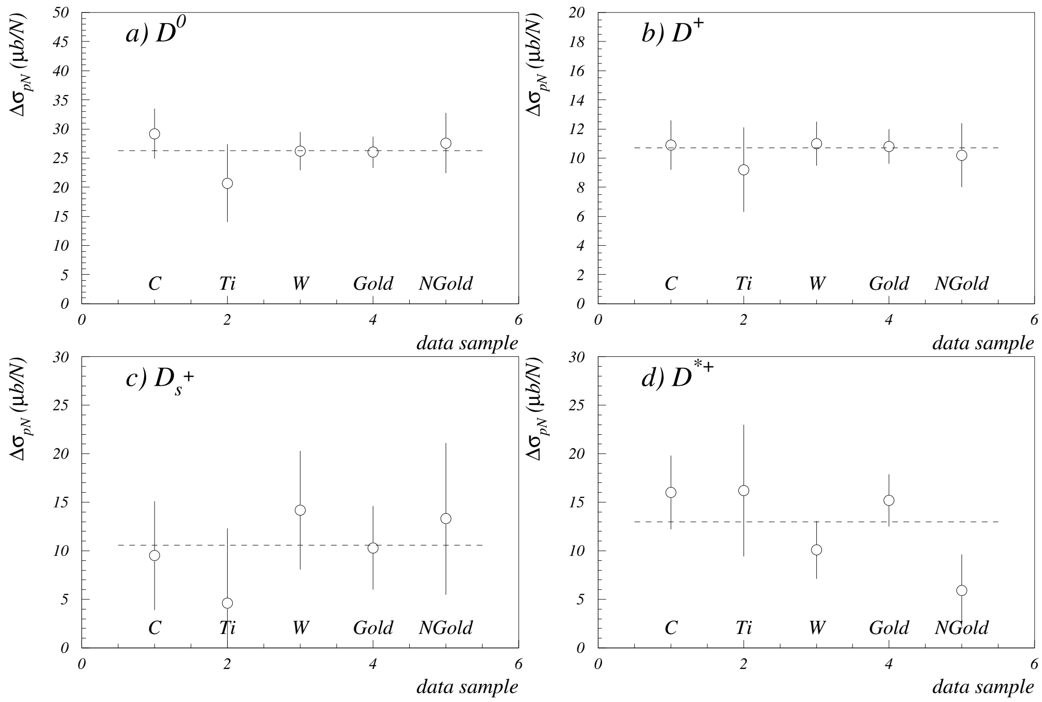

Figure 18: Comparison of the cross sections of the subsamples (points with error bars) with the cross section of the total sample (dashed line).

ment. The weighted average of the D^0, D^+ and D^{*+} asymmetries is 0.18±0.06 ($\chi^2/n.d.f$=1.4/2), i.e. three standard deviations above the zero value and within one standard deviation of the PYTHIA prediction.

	D^0	D^+	D^{*+}	D_s^+
Measurement	0.10±0.09	0.25±0.10	0.24±0.18	0.20±0.33
PYTHIA	0.24	0.22	0.23	-0.06

Table 18: Leading to non-leading particle asymmetries in the range of $-0.15 < x_F < 0.05$. For the D_s^+ the anti-particle cross section was used for σ_{LP} in Eq. 18

4.5 A-dependence of cross sections

The dependence on the atomic number A of the target material is parameterized with Eq. 11. Since we reconstructed the D meson decays in the data samples of three different target materials, we could measure the exponent α in Eq. 11. We used two fitting methods: the least square fit of Eq. 11 to the cross sections per nucleus $\Delta\sigma_{pA}$ and the simultaneous maximum likelihood fit to the invariant mass distributions of individual material data samples. When we calculated the weighted average of parameter α for all four D meson samples, we took only those D^{*+}, for

$\Delta\sigma_{pA}$ [mb]				
target	D^0	D^+	D_s^+	D^{*+}
C	0.35±0.05	0.13±0.02	0.11±0.07	0.19±0.05 (0.23±0.07)
Ti	0.99±0.32	0.44±0.14	0.22±0.37	0.77±0.33 (1.04±0.54)
W	4.81±0.61	2.02±0.28	2.62±1.12	1.86±0.56 (2.30±0.92)

Table 19: Visible cross sections per nucleus (uncorrected). Numbers in parenthesis of the last column are for the subsamples of D^{*+} with D^0 daughter not common to the D^0 samples of the first column.

which the D^0 daughter particle was not reconstructed in the D^0 sample. In this case the number of reconstructed D^{*+} was 46±12 and the visible cross-section 16.9±4.6 μb/N.

Least square fits Eq. 11 was fitted to the measured visible cross sections per nucleus $\Delta\sigma_{pA}$, calculated with Eq. 10 and summarized in Table 19. The data for N_i, Br, ϵ_i and $\mathcal{L}_i$ in Eq. 10 with i being C, Ti or W was taken from Tables 12, 16, 15 and 6 respectively. The fitting was done in PAW with the option "e". The fits are shown in Fig. 19.

Simultaneous maximum likelihood fits With this method the invariant mass histograms for C, Ti and W data samples were fitted simultaneously using the binned maximum likelihood fit (option "le" in PAW). The signals were parameterized with a Gaussian, normalized to the number of events N_i given by Eq. 12

$$S_i(m) = \frac{Br \cdot \epsilon_i \cdot \mathcal{L}_i \cdot \Delta\sigma_{pN} \cdot A_i^\alpha}{\sqrt{2\pi}\sigma_m} e^{-\frac{(m-m_0)^2}{2\sigma_m^2}} \quad , \qquad i = C,\ Ti,\ W \tag{19}$$

The free parameters are the exponent α, the cross section $\Delta\sigma_{pN}$, the peak position m_0 and the width σ_m, and are common to all three data samples. The branching ratio Br, the three efficiencies ϵ_i, integrated luminosities $\mathcal{L}_i$ and the atomic numbers A_i were taken from Tables 16, 15 and 6 respectively.

The backgrounds were parameterized similary to the fits of total data samples. For D^0, D^+ and D_s^+ the combinatorial backgrounds were parameterized by an exponential

$$B_i^{exp}(m) = e^{a_i + b\cdot m} \quad , \qquad i = C,\ Ti,\ W \tag{20}$$

with free parameters a_C, a_{Ti}, a_W describing the normalization and b describing the shape of the background. The parameter b is common to all three samples. The charm background in the D^0 invariant mass was parameterized as

$$B_i^{cc}(m) = \epsilon_i^{cc} \cdot \mathcal{L}_i \cdot \sigma_{cc} \cdot A_i^\alpha \cdot B_{cc}(m) \quad , \qquad i = C,\ Ti,\ W \tag{21}$$

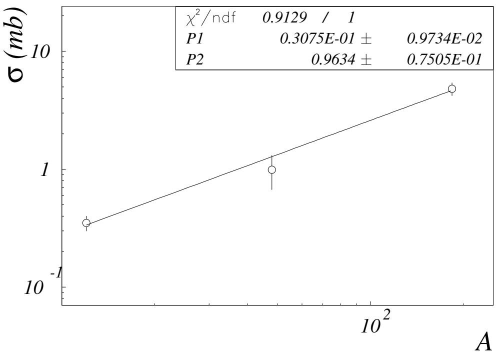

(a) D^0

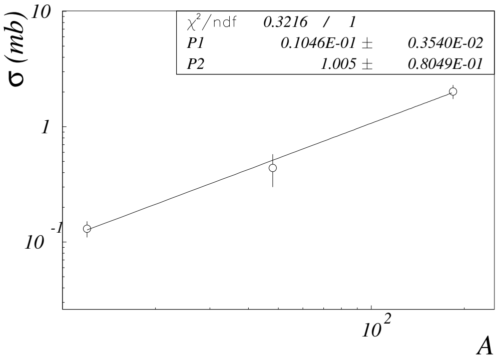

(b) D^+

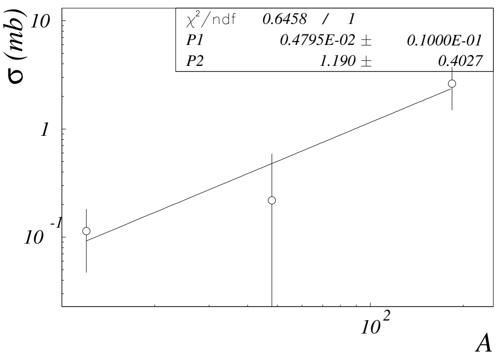

(c) D_s^+

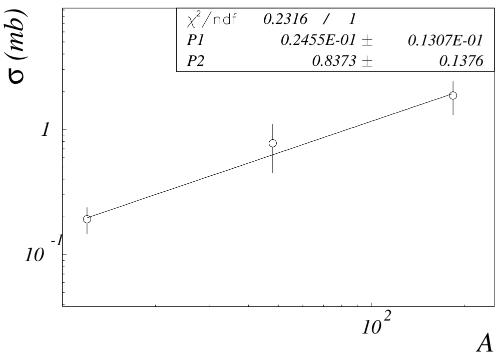

(d) D^{*+}

Figure 19: A-dependence least square fits to cross sections per nucleus from Table 19

with the free parameter σ_{cc} common to all three subsamples and α the same as in Eq. 19. The efficiencies ϵ_i^{cc} were determined from $c\bar{c}$ Monte Carlo as well as the normalized shape $B_{cc}(m)$ of this background.

The peak of the D^+ in the D_s^+ invariant mass was parameterized with the Gaussian of fixed position and width (1.869 GeV, 15 MeV) and with the normalization

$$N_i^{D^+} = \epsilon_i \cdot \mathcal{L}_i \cdot s \cdot A_i^\alpha \ , \qquad i = C,\ Ti,\ W \tag{22}$$

where the free parameter s is common to all three subsamples and the α same as in Eq. 19. The parameter s is proportional to the D^+ cross section. Unfortunately, the statistics of the $c\bar{c}$ Monte Carlo is too low for the determination of $D^+ \to \phi\pi^+$ efficiencies ϵ_i. We approximated them with the values for the D_s^+ decay obtained from signal Monte Carlo.

The background in D^{*+} invariant mass was parameterized as

$$B_i(q) = a_i(q^{1/2} + bq^{3/2}) \ , \qquad i = C,\ Ti,\ W \tag{23}$$

again with free parameters a_C, a_{Ti}, a_W and parameter b common to all three samples.

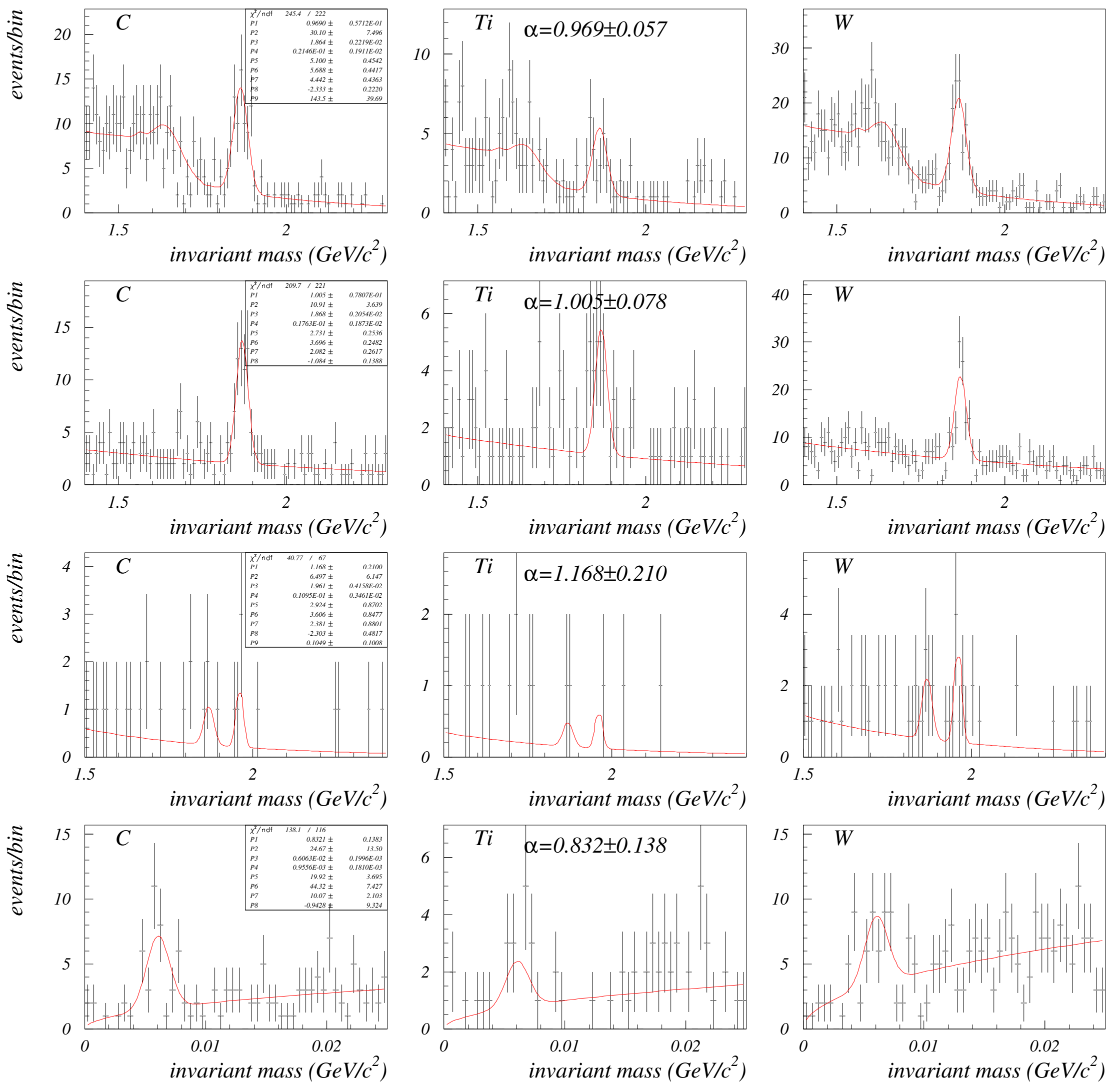

Figure 20: A-dependence simultaneous maximum likelihood fits. From top to bottom: invariant masses of C (left), Ti (middle) and W (right) samples for D^0, D^+, D_s^+ and D^{*+} mesons.

To summarize, the number of free parameters was 8 for D^+ and D^{*+} (α, $\Delta\sigma_{pN}$, m_0, σ_m, a_C, a_{Ti}, a_W, b), and 9 for D^0 and D_s^+ (α, $\Delta\sigma_{pN}$, m_0, σ_m, a_C, a_{Ti}, a_W, b, σ_{cc} or s). The fits are shown in Fig. 20.

The results from both methods are summarized in Table 20. Both methods gave very similar results, but the errors from the likelihood fits are smaller. Our result, $\alpha = 0.98 \pm 0.04$ is compatible with a linear dependence of cross sections and also with the result of E789 [7], $\alpha = 1.02 \pm 0.03 \pm 0.02$.

	α	
Particle	least square	likelihood
D^0	0.963±0.075	0.969±0.057
D^+	1.005±0.080	1.005±0.078
D_s^+	1.190±0.402	1.168±0.210
D^{*+}	0.837±0.138	0.832±0.138
	(0.849±0.179)	(0.847±0.185)
Average	0.975±0.052	0.982±0.044

Table 20: A-dependency parameter α from the least square and from the simultaneous likelihood fits and a weighted average for all four D mesons. For the weighted average the numbers in parenthesis of the fifth row were used. These numbers are for the subsample of D^{*+} with D^0 daughter not common with the D^0 sample.

5 Kinematical distributions

Since at HERA-B the projectiles and the target nuclei are not polarized the kinematics of the produced D mesons is determined by the two dimensional distribution in momentum space $d^2\sigma/\pi dp_T^2 dx_F$, given in the center of mass system (CMS) of the collisions. With p_T and x_F we denoted the transverse and the normalized longitudinal momentum coordinates. The normalized longitudinal momentum x_F (Feynman's x variable) is defined as $x_F = 2p_z/\sqrt{s}$, where p_z is longitudinal momentum and $\sqrt{s}$ the total energy of the collision, both given in the CMS.

With the statistics of about 400 reconstructed D mesons we are not able to measure the two dimensional distribution but only its projections $d\sigma/dp_T^2$ and $d\sigma/dx_F$. Furthermore the phase space (p_T, x_F) is limited by the detector acceptance to the band along p_T with the width of $-0.15 < x_F < 0.05$. This band contains, according to PYTHIA, about 45% of D mesons.

5.1 Parameterization of distributions

5.1.1 Transverse momentum

For the transverse momentum distribution the following parameterizations have been found in the literature

$$\frac{d\sigma}{dp_T^2} \propto e^{-bp_T^2} \tag{24}$$

$$\frac{d\sigma}{dp_T^2} \propto e^{-b'p_T} \tag{25}$$

$$\frac{d\sigma}{dp_T^2} \propto (\alpha m_c^2 + p_T^2)^{-\beta} \tag{26}$$

The exponential parameterization in p_T^2 (eq. 24) was used by most experiments, but was found by E769 [6] to describe the measurements well only for transverse momenta below 1 GeV/c. Above 1 GeV/c the distribution becomes more like exponential in p_T (eq. 25). The last parameterization by eq. 26 was introduced by Frixione [9] and fits the data of E769 well over the entire p_T range. The mass of the c quark m_c in eq. 26 is usually set to 1.5 GeV and the other two parameters α and β are being free in a fit. We found that the errors of the parameters α and β given by the fit are highly correlated and large. The parameterization by eq. 26 can be rewritten into the form used by the HERA-B vector meson analysis: $(1 + (\frac{p_T}{p_0})^2)^{-\beta}$. Also in this parameterization the correlation between parameters p_0 and β remains large. By replacing p_0 with the mean transverse momentum of the distribution $\langle p_T \rangle$ the parameterization reads

$$\frac{d\sigma}{dp_T^2} \propto [1 + (\frac{\sqrt{\pi}\,\Gamma(\beta - \frac{3}{2})\, p_T}{2\,\Gamma(\beta - 1)\, \langle p_T \rangle})^2]^{-\beta} \tag{27}$$

With this parameterization the correlation between the errors of $\langle p_T \rangle$ and β is small. The eq. 27 is more suitable for fitting the data than eq. 26.

Eq. 27 with the fixed exponent $\beta = 6$ is usually used for the parameterization of the J/ψ transverse momentum distributions and reads

$$\frac{d\sigma}{dp_T^2} \quad \propto \quad [1 + (\frac{35\pi\, p_T}{256\langle p_T\rangle})^2]^{-6} \tag{28}$$

It could be easily shown that for large exponents ($\beta \to \infty$) eq. 27 limits towards eq. 24 with parameters $\langle p_T\rangle$ and b related by $b = \frac{\pi}{4}\frac{1}{\langle p_T\rangle^2}$.

5.1.2 Feynman's x variable

Usually the x_F distribution is parameterized with a power-law function:

$$\frac{d\sigma}{dx_F} \propto (1 - |x_F|)^n \tag{29}$$

When compared to the predictions from next-to-leading order QCD calculations this function does not reproduce well the central region. The experimental observation made by E791 [10] in 500 GeV π-A collisions using high statistics of 80k reconstructed D^0 also shows a similar discrepancy. They fitted their data with a function which is an extension of eq. 29 and which uses a power-law function in the tail region and a Gaussian in the central region [‖]

$$\frac{d\sigma}{dx_F} = \begin{cases} Ae^{-\frac{x_F^2}{2\sigma_g^2}} & , \quad |x_F| < x_b \\ A'(1 - |x_F|)^n & , \quad |x_F| \geq x_b \end{cases} \tag{30}$$

To ensure a continuity of the function and its first derivative at $|x_F| = x_b$ the parameters σ_g and the ratio A/A' are related by

$$\sigma_g \quad = \quad \sqrt{\frac{x_b(1 - x_b)}{n}} \tag{31}$$

$$\ln\frac{A}{A'} \quad = \quad n(\frac{x_b}{2(1 - x_b)} + \ln(1 - x_b)) \tag{32}$$

Thus the parameterization by eq. 30 has two free parameters, the exponent n and the boundary variable x_b. The experiment E791 [10] measurement for the boundary variable is $x_b = 0.062 \pm 0.013$.

5.2 Generated distributions with Monte Carlo

We compared the kinematical distributions from Monte Carlo for possible differences between different D mesons, their charge conjugate states and the target materials on which they are produced. We found no difference between the distributions for different targets and only a

[‖]Since in the p-A collisions the distribution should be symmetrical, we omitted the offset parameter from their original parameterization

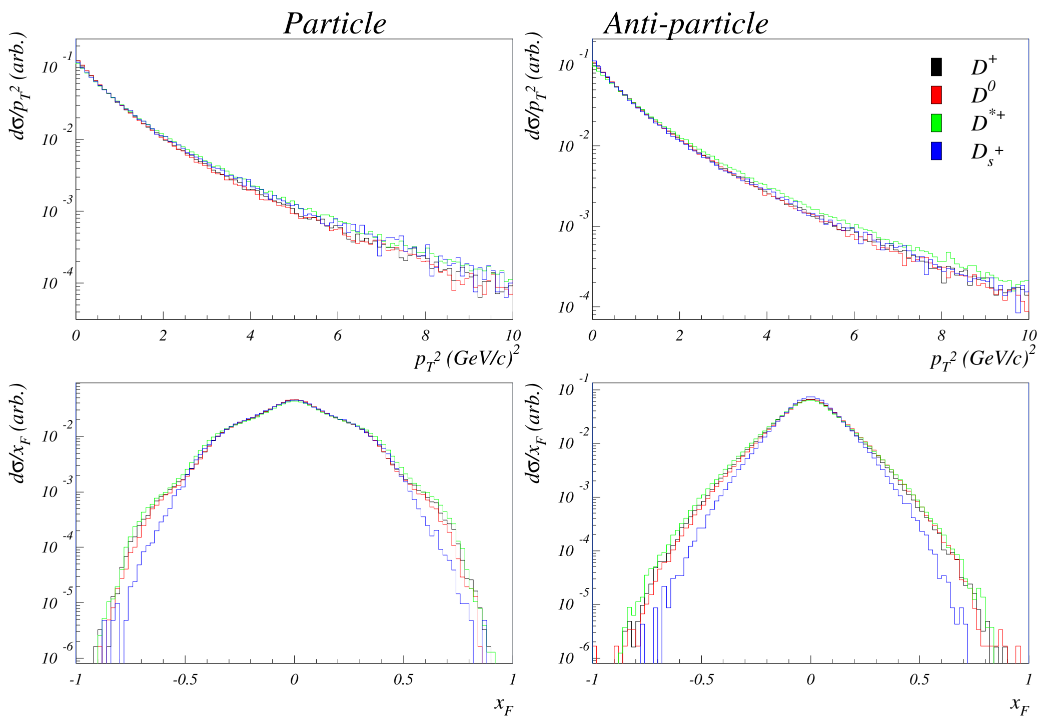

Figure 21: Comparison of kinematical distributions of D mesons in the Monte Carlo.

small difference between distributions for D mesons of equal charge (see Fig. 21). The only noticeable is the narrower distribution in x_F for the D_s^+.

The differences are larger between the charge conjugate states. The largest are the differences in the x_F distributions, which are for anti-particles narrower and smoother. Different are also the mean p_T values, which are larger for anti-particles by 8%.

The parameterizations from the previous section were fitted to kinematical distributions obtained from the Monte Carlo. The p_T distribution of events within $-0.15 < x_F < 0.05$ is best fitted by the parameterization with $\langle p_T \rangle$ and β given by eq. 27 and the worst with the exponential form of eq. 24. The fits are shown in Fig. 22. Also shown is the parameterization of eq. 25 which fits well only for $p_T > 1$ GeV/c and the parameterization with $\langle p_T \rangle$ and the exponent $\beta = 6$, which would fit low statistics data reasonably well.

The x_F distributions obtained from Monte Carlo simulation were fitted with eqs. 29 and 30. The fits are shown in Fig. 23. The power-law parameterization, eq 29 does not reproduce the central region well, while the extended parameterization eq. 30 fits it well. The boundary parameter value from the fit is $x_b = 0.055$ and is consistent with $x_b = 0.062 \pm 0.013$ measured by E791.

With the parameterization of eq. 30 we fitted separately the distributions for both charge conjugate states of D^+ (fig. 24). The fitted exponent n is quite different. The values are 4.4 for particles and 7.1 for anti-particles. The distributions for particles also show "shoulders" at $x_F = \pm 0.3$, which are not modeled with the parameterization.

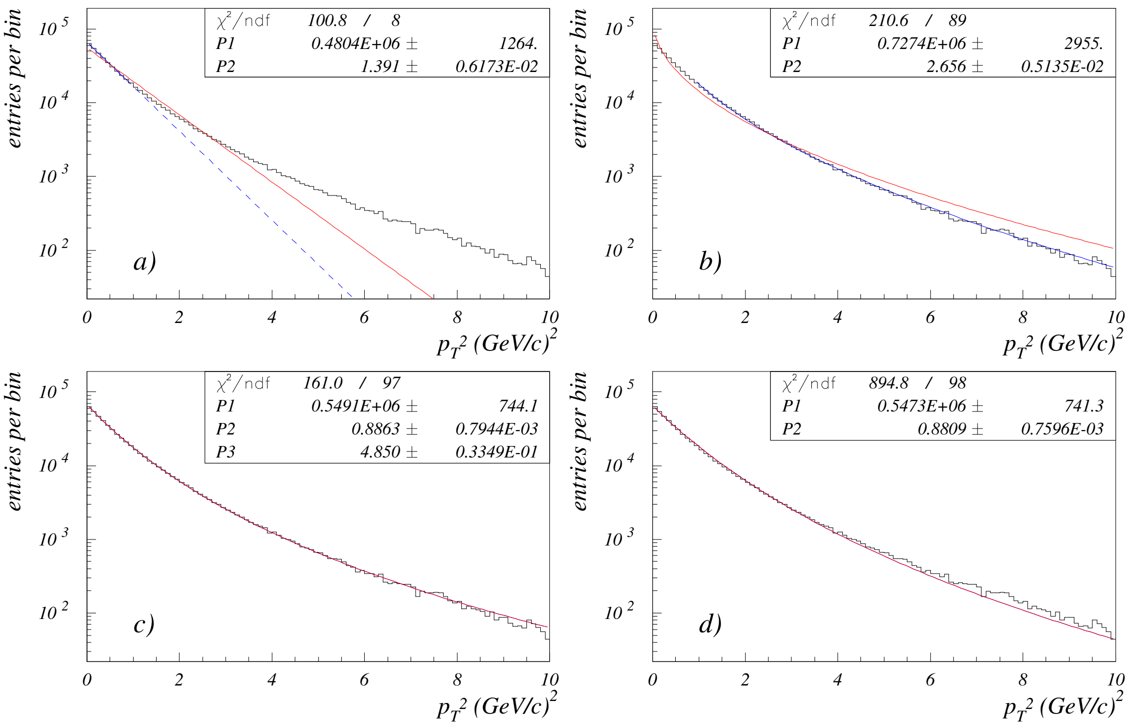

Figure 22: Fits of p_T^2 distribution from D^+ Monte Carlo with different parameterizations: a) eq. 24, b) eq. 25, c) eq. 27 and d) eq. 28. With blue curves in a) and b) fits in the ranges $p_T^2 < 1$ GeV/c and $p_T^2 > 1$ GeV/c respectively are shown.

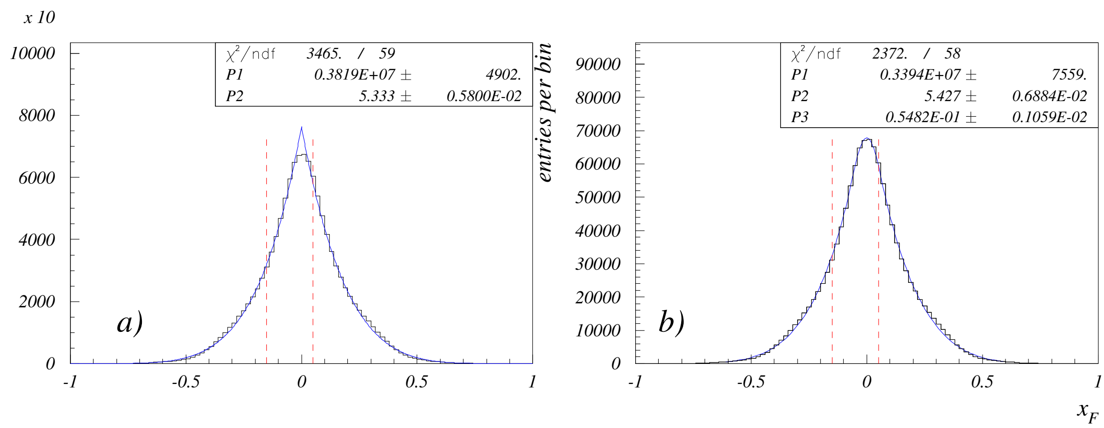

Figure 23: Fits of x_F distribution from D^+ Monte Carlo with different parameterizations: a) eq. 29 and b) eq. 30, both fitted in the range $-0.6 < x_F < 0.6$. With vertical dashed lines the visible range is indicated.

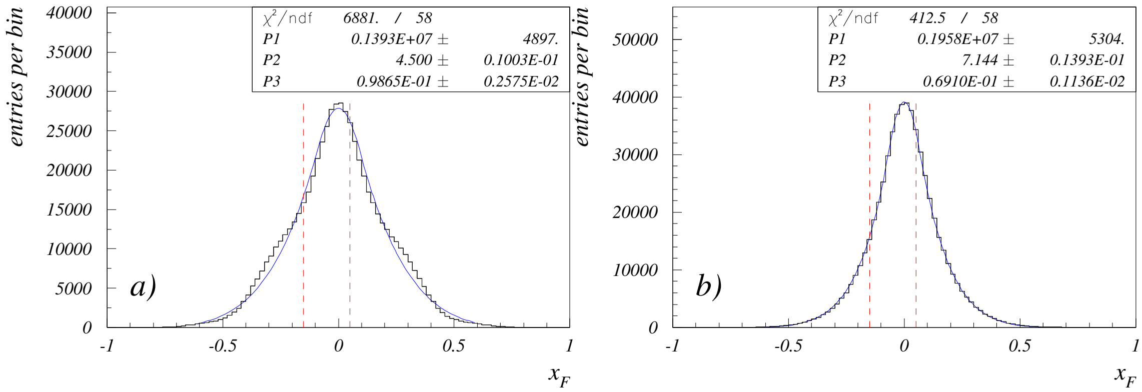

Figure 24: Fits of x_F distribution from D^+ Monte Carlo for a) D^+ and b) D^- mesons. Fitted with eq. 30 in the range $-0.6 < x_F < 0.6$. With vertical dashed lines the visible range is indicated.

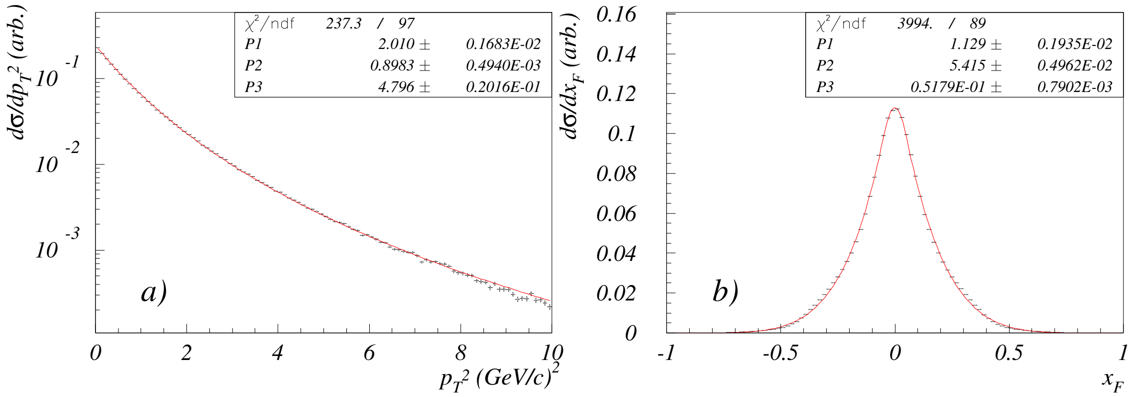

Figure 25: Fits to the normalized distributions of the mixture of D mesons: a) $d\sigma/dp_T^2$ for $D^0/D^+/D^{*+}$ mixture fitted with eq. 27 and b) $d\sigma/dx_F$ for D^0/D^+ mixture fitted with eq. 30.

We also checked the fitting in the range of $-0.10 < x_F < 0.05$. The boundary parameter was fixed to $x_b = 0.062$ of E791, since the fitting range is too small for having this parameter free. The fit resulted in $n = 5.6$ while the result in the wide range of $-0.6 < x_F < 0.6$ is $n = 5.4$. The fit with the power-law gave a considerably smaller value of $n = 4.4$.

Finally we fitted the distributions for a mixture of D mesons, corresponding to that in the real data for the measurements of $d\sigma/dp_T^2$ and $d\sigma/dx_F$. Fits with eq. 27 for the p_T^2 and with eq. 30 for the x_F distributions are shown in Fig. 25. The parameter values from the fits are summarized in Table 21.

$d\sigma/dp_T^2$		$d\sigma/dx_F$	
$\langle p_T \rangle$	β	n	x_b
0.898	4.80	5.42	0.052

Table 21: Fitted parameters for D meson mixtures.

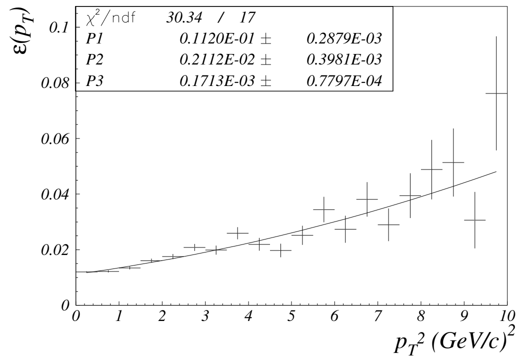

(a) D^0

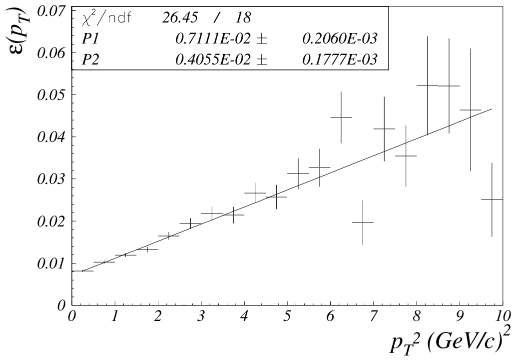

(b) D^+

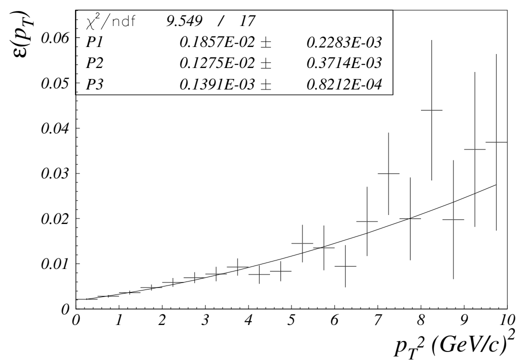

(c) D_s^+

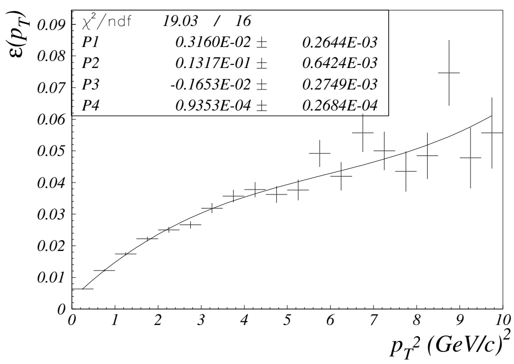

(d) D^{*+}

Figure 26: Acceptance in p_T^2

5.3 Acceptances

The acceptances were determined in bins of p_T^2 and x_F from signal Monte Carlo with the method explained in section 4.2. The only difference was in the method of counting the reconstructed decays, where we did not fit the invariant mass distributions, but counted the events in the signal window and subtracted the counts in side bands, or for D^{*+} subtracted the wrong sign combinations in the signal window.

The acceptances in p_T^2, presented in Fig. 26, show a quadratic dependence for D^0 and D_s^+, a linear for D^+, while the acceptance of D^{*+} is a bit more complicated. We fitted it with the 3^{rd} order polynomial. Since the acceptances are not constant in p_T, the total cross section measurements clearly depend on the assumed shape of the p_T distribution.

The acceptances in x_F are shown in Fig. 27. The data points were fitted with a function

$$\epsilon(x) = Ce^{\frac{(x-x_0)^2}{2\sigma^2}(A+Bx)} \tag{33}$$

Contrary to the p_T^2, the acceptances in x_F are limited to a relatively small central region, which

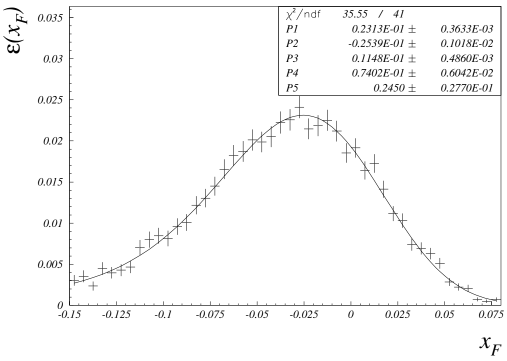

(a) D^0

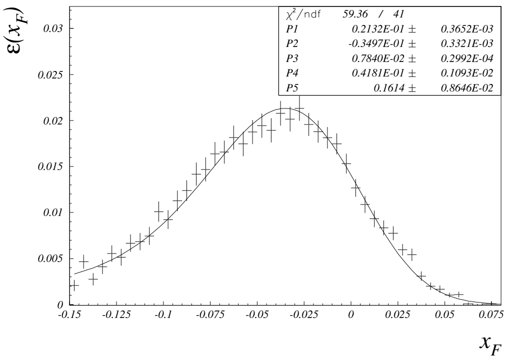

(b) D^+

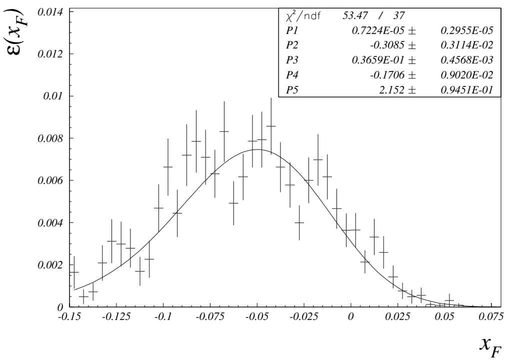

(c) D_s^+

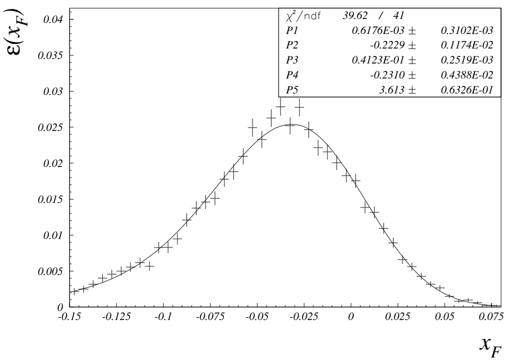

(d) D^{*+}

Figure 27: Acceptance in x_F

is slightly shifted to the negative values of x_F. The maxima are at -0.03, except for the D_s^+ with the maximum at -0.05. We chose for the visible range the interval of $-0.15 < x_F < 0.05$ for all four D mesons.

For the determination of $d\sigma/dp_T^2$ and $d\sigma/dx_F$ we used the fitted functions and not the data from bins.

5.4 Measurement of $d\sigma/dp_T^2$

To extract the parameters of a given parameterization of the $d\sigma/dp_T^2$ distributions we used a simultaneous maximum likelihood fit of events in the signal window and in the side bands. We fitted separately the D^0, D^+ and D^{*+} data samples, as well as all three data samples simultaneously. The D_s^+ data sample was excluded, because of its low statistics. We fitted all four parameterizations, given by eqs. 24, 25, 27 and 28.

The procedure was the same as was used for the life time fits in section 3.5. The events in the invariant mass signal window and the events in the side bands ** were first histogrammed in p_T^2 and then the histograms were simultaneously fitted. We had two histograms per D meson data sample: one for the events in the signal window and the other for the events in the side bands. The side bands were of the same size as the signal window and the size was chosen wide enough to include all signal events: ± 75 MeV for D^0, ± 50 MeV for D^+ and ± 3 MeV for D^{*+}.

The number of D mesons in a given p_T^2 bin is according to eq. 13 by taking $\alpha = 1$

$$N_D(p_T^2) = Br \cdot \epsilon(p_T^2) \cdot \sum_i \mathcal{L}_i A_i \cdot \frac{d\sigma}{dp_T^2} \Delta p_T^2 \tag{34}$$

where $\epsilon(p_T^2)$ is the acceptance, determined in the previous section from the Monte Carlo, Δp_T^2 the bin size of the histograms and

$$\frac{d\sigma}{dp_T^2} = \Delta\sigma_{pN} P(p_T) \tag{35}$$

the parameterization of the differential cross section with one of the normalized functions of eq. 24, 25, 27 or 28. The $\Delta\sigma_{pN}$ is the visible cross section and was also a free parameter in the fit. The normalization constants of the parameterizations can be easily calculated. The normalized parameterizations are:

$$\begin{aligned}
P(p_T) &= b \cdot e^{-bp_T^2} && (36)\\
P(p_T) &= \frac{b'^2}{2} \cdot e^{-b' p_T} && (37)\\
P(p_T) &= (\beta - 1)A^2 \cdot [1 + (A\, p_T)^2]^{-\beta}\ , \qquad A = \frac{\sqrt{\pi}\,\Gamma(\beta - \frac{3}{2})}{2\,\Gamma(\beta - 1)\,\langle p_T \rangle} && (38)\\
P(p_T) &= 5A^2 \cdot [1 + (A\, p_T)^2]^{-6}\ , \qquad A = \frac{35\pi}{256\langle p_T \rangle} && (39)
\end{aligned}$$

Our default parameterization was the one with $\langle p_T \rangle$ and β given by eq. 38, which fits the Monte Carlo very well and was proven by E769 to fit the data in their entire p_T range.

The distribution of background events $N_{bgr}(p_T^2)$ was assumed to be the same in shape and normalization for the signal window and side bands. Several parameterizations, listed in Table 22, were fitted first to the distributions of the events from side bands. They all fit well. We chose the one among those with 2 free parameters which gave the smallest χ^2/ndf. These were function No.1 for D^0 and D^+ and function No.2 for D^{*+}.

Finally we fitted simultaneously the events in the signal window with a function $N_D(p_T^2) + N_{bgr}(p_T^2)$ and the events in the side bands with a function $N_{bgr}(p_T^2)$. The free parameters with our default parameterization, when we fitted D meson data samples separately, were $\langle p_T \rangle$, β, $\Delta\sigma_{pN}$ for the signal and A and B for the background. With the simultaneous fit to all three data samples, the parameters $\langle p_T \rangle$ and β were common, while the σ_{pN}, A and B were used for each D meson data sample individually, thus the number of free parameters was 11.

**for D^{*+}: wrong sign combinations in the signal window

No.	Function $N_{bgr}(p_T^2)$
1	$e^{A+Bp_T^2}$
2	$e^{A+Bp_T^2}\epsilon(p_T^2)$
3	$e^{A+Bp_T^2}(1+Cp_T^2)$
4	$e^{A+Bp_T^2+Cp_T^4}$
5	$A(1+Bp_T^2)^{-6}$
6	$A(1+Bp_T^2)^{-6}\epsilon(p_T^2)$
7	$A(1+Bp_T^2)^{-6}(1+Cp_T^2)$
8	$A(1+Bp_T^2)^{-C}$

Table 22: Parameterizations for the p_T distribution of background events

data sample	$\langle p_T \rangle$ [GeV/c]	β	χ^2/ndf	$\langle p_T \rangle$, $\beta = 6$	χ^2/ndf
D^0	1.03±0.09	3.3±1.1	0.59	1.03±0.07	0.67
D^+	1.07±0.06	30±76	0.83	1.04±0.06	0.78
D^{*+}	1.03±0.11	8.7±10.1	1.13	1.02±0.11	1.10
$D^0/D^+/D^{*+}$	1.03±0.04	6.4±2.8	0.82	1.03±0.04	0.81

Table 23: Fitted parameters on real data samples.

The simultaneous fit of all three D meson data samples with default parameterization (eq. 38) is shown in Fig. 28. The resulting parameters $\langle p_T \rangle$ and β are summarized in Table 23 together with a χ^2 of the fits. Fits to all data samples gave good χ^2. Compared to the Monte Carlo (Table 21), the $\langle p_T \rangle$ is significantly larger on real data, while β is within one standard deviation equal to the Monte Carlo value. The statistics of individual D meson data samples is a bit too low for fitting with both parameters $\langle p_T \rangle$ and β being free, and resulted in a large error of the parameter β. We repeated the fit with the fixed value of $\beta = 6$. As one can see from Table 23, the parameter $\langle p_T \rangle$ has not changed much.

By subtracting the histograms of side band events from the histograms of signal window events we determined the visible differential cross sections. From eq. 15 we derived

$$\frac{d\sigma}{dp_T^2} = \frac{\frac{\Delta N}{\Delta p_T^2}}{Br \cdot \epsilon(p_T^2) \cdot \sum_i \mathcal{L}_i A_i} \tag{40}$$

where ΔN is the number of signal events in a bin at p_T^2 and of the size Δp_T^2 and $\epsilon(p_T^2)$ is the acceptance for that bin. The differential cross sections are plotted in Fig. 29. The fit of eq. 38 is also shown.

The total visible cross sections can be determined in three ways: (1) by summing the data points of Fig. 29 and multiplying the sum with the bin size, (2) from the simultaneous likelihood fit, since $\Delta\sigma_{pN}$ is a free parameter in the fit and (3) by determining the new efficiencies

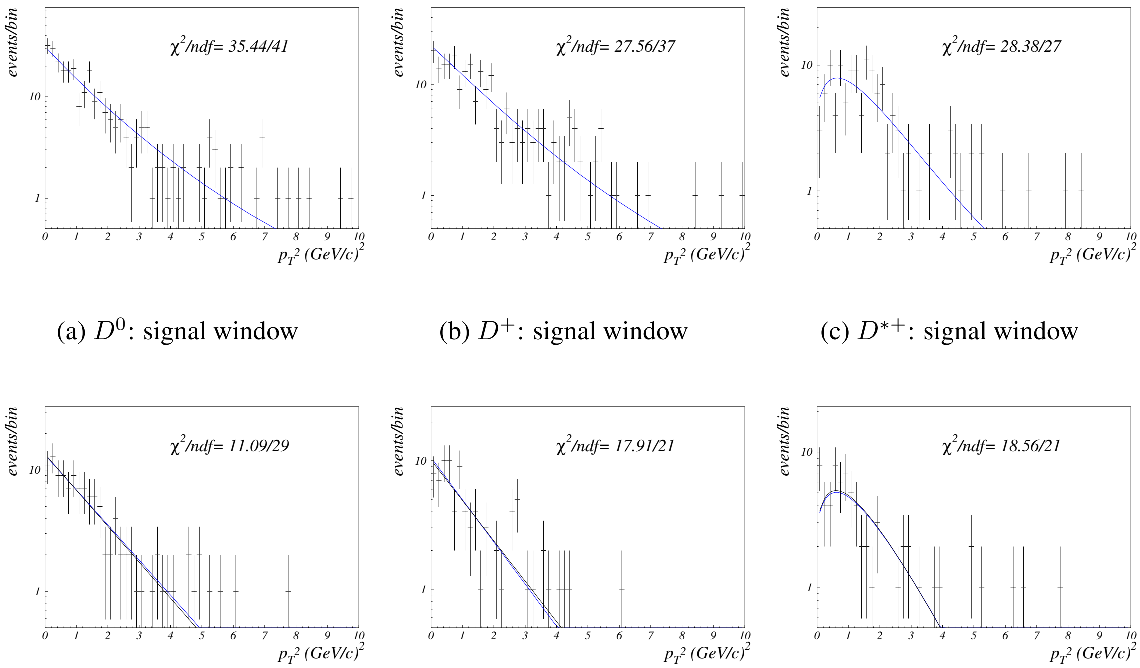

(a) D^0: signal window (b) D^+: signal window (c) D^{*+}: signal window

(d) D^0: side bands (e) D^+: side bands (f) D^{*+}: side bands

Figure 28: Simultaneous maximum likelihood fit of all three data samples.

$\Delta\sigma_{pN}$ [μb/N]			
	(1) by sum	(2) from fit	(3) re-weighted
D^0	22.6±3.0	22.9±2.9	24.7±2.4
D^+	9.4±1.3	9.5±1.3	9.8±1.0
D^{*+}	8.2±3.7	10.5±2.5	11.2±2.4

Table 24: Visible cross sections determined with three different methods (see text).

from re-weighted Monte Carlo and correcting the cross sections from Table 17 accordingly, as is explained in section 5.6. The cross sections determined in the three different ways are summarized in Table 24. The results of all three methods are in a reasonable agreement. The smallest statistical error have the cross sections determined with the method (3) because the background was fitted in the wide invariant mass range. On the other hand the results obtained with the method (1) are independent of the parameterization of the distribution.

The exponential parameterizations in p_T^2 (eq. 36) and in p_T (eq. 37) have also been fitted to the data (Fig. 30). The result of the fit with eq. 36 depends on the fit range, as one can see from Fig. 30. This fact is important when comparing our result with the results of other experiments, because the p_T ranges were different. By restricting the fitting range to p_T^2 <3 (GeV/c)^2 our result of $b = 0.84 \pm 0.10$ is in a good agreement with the measurements of the three experiments

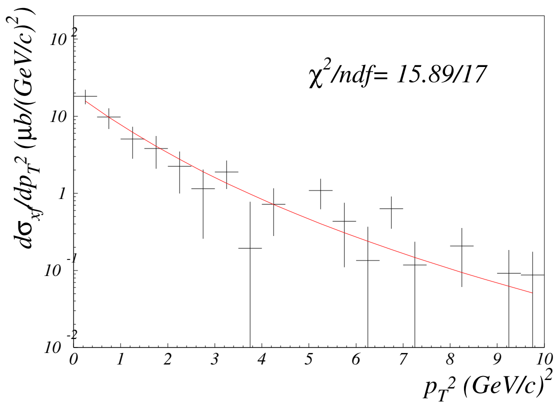

(a) D^0

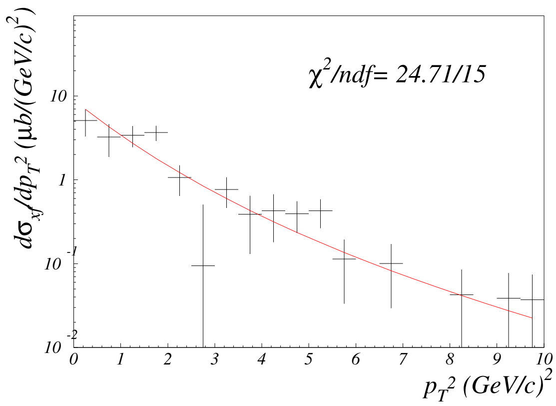

(b) D^+

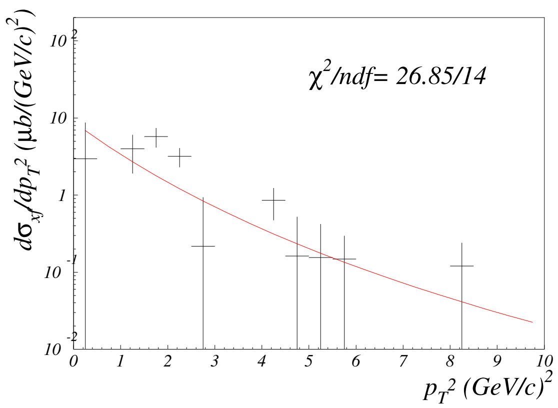

(c) D^{*+}

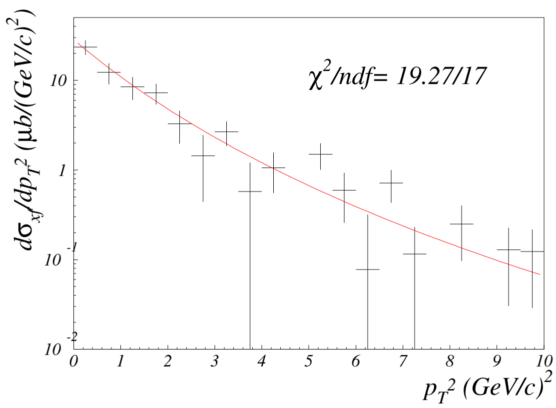

(d) D^0 + D^+

Figure 29: Differential visible cross sections $d\sigma/dp_T^2$, with the fit of eq, 38 performed simultaneously on all three D meson data samples. The cross section (d) is a sum of (a) and (b).

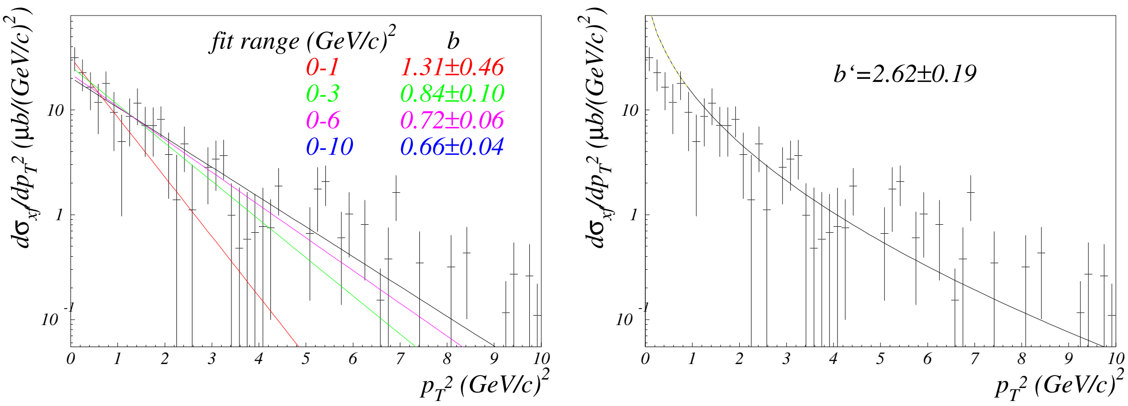

(a) Fits with eq. 24

(b) Fit with eq. 25 for $p_T > 1$ GeV/c

Figure 30: Fits with exponential parameterizations.

at 800 GeV listed in Table 4, which measured the distribution up to 3-4 (GeV/c)^2.

5.5 Measurement of $d\sigma/dx_F$

The simultaneous maximum likelihood fit of the events in the signal window and sidebands was also used for the fits to the $d\sigma/dx_F$ distribution. The background was parameterized with the same function as had been used for the parameterization of acceptances and is given with eq. 33. We fitted this function first to the data points of the side band events and got the values of parameters x_0, σ, A and B. Then in the simultaneous fit only the normalization parameter C was free.

The distribution of signal events was parameterized with the extended power low parameterization given by eq. 30. The boundary parameter x_b was fixed to the value measured by E791 ($x_b = 0.062$), because the range of $-0.15 < x_F < 0.05$ is too small to have this parameter free. By multiplying this parameterization by the acceptance $\epsilon(x_F)$, determined from Monte Carlo and shown in Fig. 27 we constructed the function for fitting the distribution of reconstructed signal events $N_D(x_F)$. Similarly to the fits in the previous section, we fitted simultaneously the events in the signal window with the function $N_D(x_F) + N_{bgr}(x_F)$ and the events in the side bands with the function $N_{bgr}(x_F)$, parameterized by eq 33.

We fitted simultaneously D^0 and D^+ data samples. The free parameters were the exponent n, the two signal normalizations A_{D^0} and A_{D^+} and the two background normalizations C_{D^0} and C_{D^+}. The fit is shown in Fig. 31. The fitted exponent n is 7.5±3.2 and agrees well with the results of E653 and E743 summarized in Table 4, but is consistent also with the Monte Carlo value of 5.4.

We fitted the data sets also at different boundary parameters x_b. As expected, the exponent is quite sensitive to the choice of the boundary parameter (see Table 25). Unfortunately, the

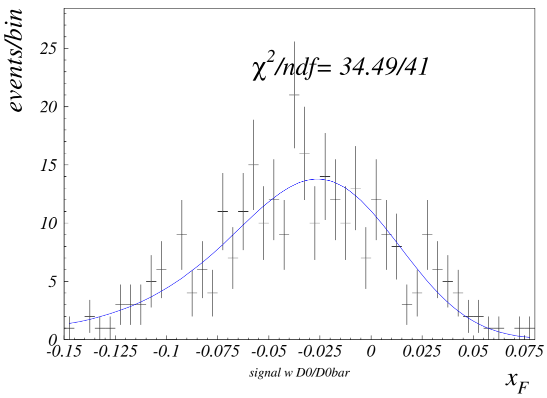

(a) D^0 signal window events

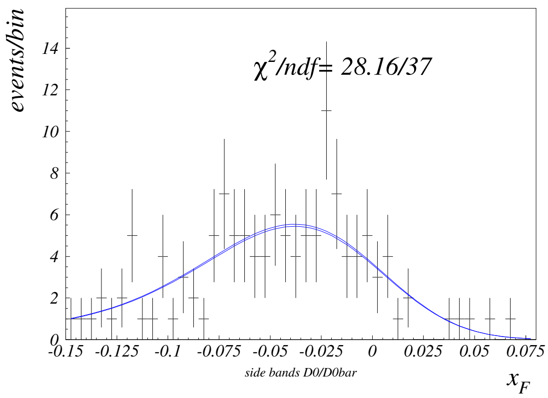

(b) D^0 side band events

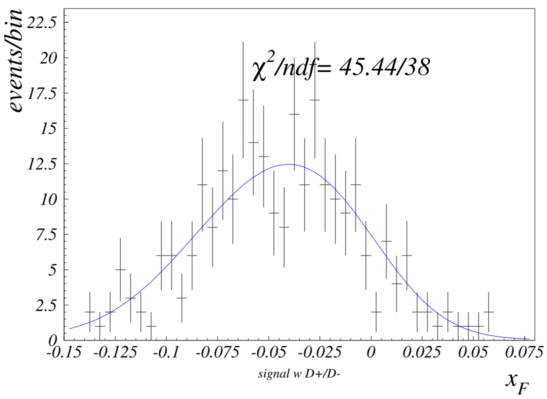

(c) D^+ signal window events

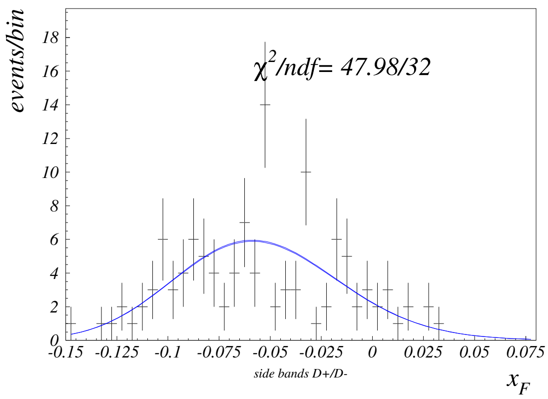

(d) D^+ side band events

Figure 31: Simultaneous maximum likelihood fit of D^0 and D^+ data samples.

x_b	n	χ^2/ndf
0.000	4.6±2.2	0.95
0.040	6.1±2.7	0.94
0.050	6.7±2.9	0.94
0.062	7.5±3.2	0.94
0.070	8.0±3.5	0.93
0.100	10.4±4.4	0.94

Table 25: Fitted exponent n at different values of the parameter x_b

x_F range of our data sets is too small to be competitive in this measurement with the other experiments.

With the expression similar to eq. 40 we determined the differential cross section $d\sigma/dx_F$ in several bins in the accessible range. The plots are shown in Fig. 32 together with the fits with different values of x_b.

5.6 Re-weighting of Monte Carlo events

The x_F distribution measured by E653 and E743 and the p_T distribution determined from our data differ to the distributions generated with PYTHIA. Since the acceptance depends on both kinematical variables, the kinematical distributions in the signal Monte Carlo have to be re-weighted in order to determine the efficiencies correctly.

The weights were determined from the normalized distributions for the real data and for the Monte Carlo events $P_{DATA}(x)$ and $P_{MC}(x)$ respectively with $x \equiv p_T$ or $x \equiv x_F$. We used the same parameterizations for the Monte Carlo and the real data distributions. For the p_T distributions the parameterization with eq. 38 was used, while for the x_F distributions to study the systematics both parameterizations were taken; the power law parameterization given with eq. 29 and the extended one with eq. 30. The errors on the measured parameters were used for the estimation of the systematic error.

The weights were calculated as the ratio of normalized distributions

$$w(x) = \frac{P_{DATA}(x)}{P_{MC}(x)} \tag{41}$$

The parameter values for P_{MC} were taken from fits to the mixture of D mesons (Table 21) and the values for P_{DATA} from the measurements. The parameters are summarized in Table 26 and the weights are plotted in Fig. 33. Note that the weights are the same for all D meson samples. In this respect small differences in distributions between different D mesons and their charge conjugate states remain after re-weighting. We think, that this is more correct than to re-weight all Monte Carlo D meson samples to the same distribution, since no measurements exist which would prove that the distributions are the same.

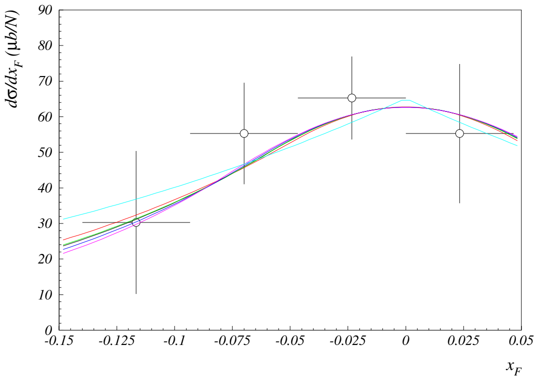

(a) D^+

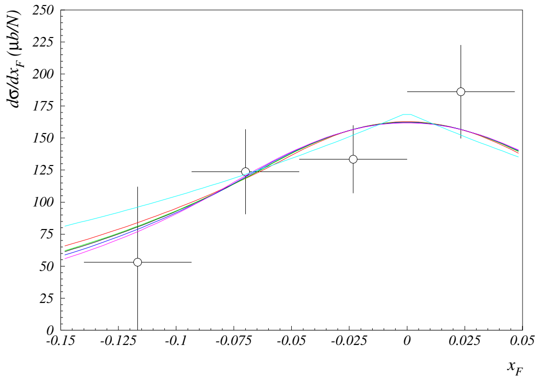

(b) D^0

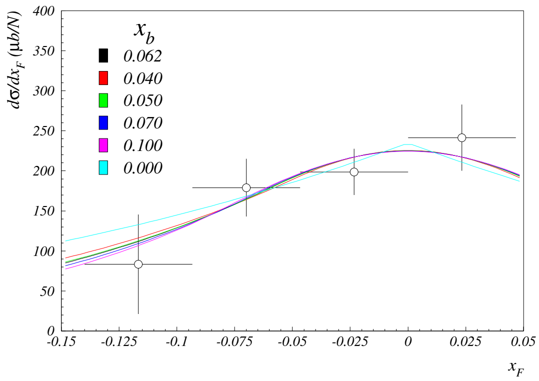

(c) $D^+ \ + \ D^0$

Figure 32: Differential cross sections $d\sigma/dx_F^2$ with fits for different values of boundary parameter x_b.

	$\langle p_T \rangle$	β	n	x_b
MC	0.898	4.80	5.42 (5.33)	0.052
DATA	1.03±0.04	6.4±2.8	7.7±1.4	0.062

Table 26: Parameter values used for the determination of weights. The value for n written in parenthesis was used with the power law parameterization eq. 29.

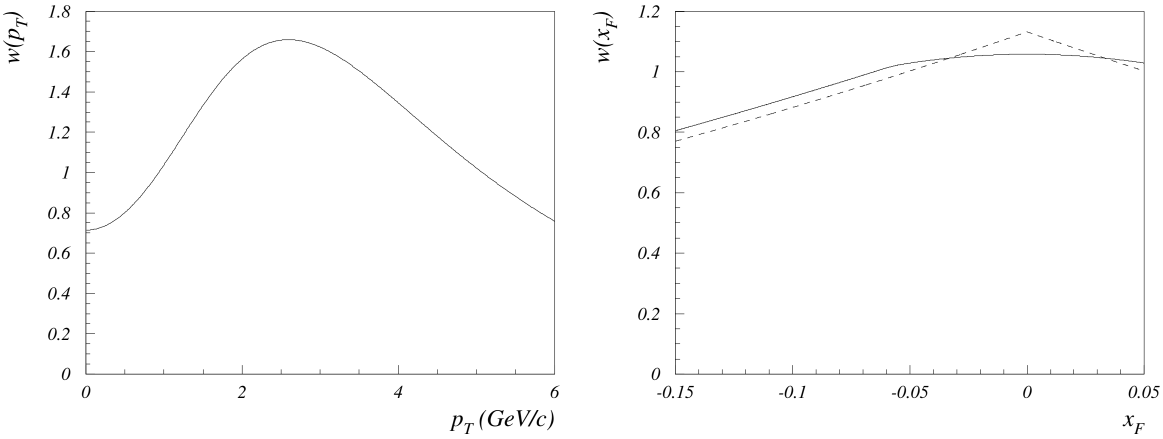

Figure 33: Weights for the p_T distribution (left) and weights for the x_F distribution (right). The dashed curve are the weights calculated from the power law parameterization eq. 29.

To determine the efficiency correction factors we calculated the efficiencies from unweighted and from weighted Monte Carlo by following the same procedure as explained in section 4.2. The difference was in the counting procedure of reconstructed decays: we used the side band subtraction method and not a fit to the invariant mass distribution. The number of reconstructed and the number of generated decays in eq. 16 was in the case of re-weighted Monte Carlo obtained by summing the weights of the D mesons.

The efficiency correction factors were summarized in Table 27. The errors were obtained by calculating the factors for the particular parameter at the values shifted by one standard deviation up and down from its central value and taking the half of the resulting difference. The errors resulting from variation of $\langle p_T \rangle$ and β were added in quadrature.

The difference between correction factors for both charge conjugate states as well as the difference between different wire samples are negligible compared to the estimated errors, thus the same correction factors can be used for all subsamples of a particular D meson.

The difference arising from the two parameterizations of the x_F distribution is also small compared to the errors, as one can see from Table 27. We have chosen the correction factors obtained with extended power law parameterization eq 30 and added the difference in quadrature to the error. The products of both correction factors, e.g. the overall correction factors for efficiencies are summarized in Table 28.

5.7 Visible fraction

In order to extrapolate the measurements to the full phase space we need to determine the fraction of D mesons in the visible range defined by $-0.15 < x_F < 0.05$. By using the measured value of the exponent $n = 7.7 \pm 1.4$ we calculated the visible fraction from both parameterizations. The visible fractions obtained from the power low parameterization eq. 29 and from the

meson	p_T	x_F (eq. 30)	x_F (eq. 29)
D^0	1.063±0.025	1.023±0.015	1.032±0.018
D^+	1.107±0.038	1.017±0.010	1.020±0.011
D_s^+	1.178±0.090	1.006±0.002	1.003±0.001
D^{*+}	1.165±0.050	1.023±0.015	1.030±0.017

Table 27: Correction factors obtained from re-weighting of distributions in p_T and x_F.

D^0	D^+	D_s^+	D^{*+}
1.087±0.032	1.126±0.040	1.185±0.091	1.192±0.055

Table 28: Overall efficiency correction factors from re-weighting of kinematical distributions.

extended power law parameterization eq. 30 are 0.558±0.051 and 0.542±0.048 respectively. The difference is small compared to the error, estimated from the error of parameter n. For the extrapolation we decided to use the average of both numbers:

$$f_{vis} = 0.55 \pm 0.05 \tag{42}$$

For comparison, the visible fractions given by the signal Monte Carlo are 0.45, 0.44, 0.46 and 0.43 for D^0, D^+, D_s^+ and D^{*+} respectively.

6 Systematic errors

In this section the systematic uncertainties are determined for the following measurements: total visible production cross sections, cross section ratios, A-dependence parameter α and leading to non-leading particle asymmetries.

6.1 Total visible cross sections

The total systematic uncertainties are according to Eq. 15 composed of contributions from event counting, branching fractions, integrated luminosity and reconstruction efficiency. Furthermore, the uncertainty of the reconstruction efficiency can be divided into contributions from Monte Carlo statistics, track reconstruction efficiency, particle identification efficiency, analysis cuts and the contribution from the reweighting of kinematical distributions.

6.1.1 Event counting

A source of the systematic uncertainty is the parameterization of the combinatorial background. We used the exponential shape for D^0, D^+ and D_s^+, but a linear or a quadratic function could also be fitted well. The number of fitted events with the three different parameterizations are presented in Table 29. The systematic error of the event counting was estimated as a maximal deviation of the number of events and amounts to 3.4%, 2.6% and 6% for the D^0, D^+ and D_s^+, respectively.

For the D^{*+} the estimation of the counting error was done by fitting the wrong sign events with the same parameterization as for the background in the right sign events and using the resulting shape in a fit to the right sign events. The systematic uncertainty was estimated to 9.7%.

Meson	exp.	linear	quadratic	rel. error
D^0	174.8	168.9	173.4	3.4%
D^+	148.2	144.4	145.1	2.6%
D_s^+	11.7	12.4	10.9	6.0%

Table 29: Fitted number of events with exponential, linear or quadratic parameterizations of the combinatorial background.

6.1.2 Branching fractions

The uncertainties of the branching fractions (Table 16) are 1.8%, 3.6%, 13% and 1.9% for the D^0, D^+, D_s^+ and D^{*+}, respectively.

6.1.3 Integrated luminosities

Uncertainties on the integrated luminosities were taken from the HERA-B Minimum bias web page. The individual relative errors for C, Ti and W are 4.8%, 5.0% and 3.8%, respectively and a common scaling error is 2%. With the standard error propagation and assuming that the individual errors are uncorrelated, we obtained an error of 2.7% on the integrated luminosities summed over nucleons $\sum_i A_i \mathcal{L}_i$. By adding in quadrature a common scaling error of 2% we estimated the systematic uncertainty to 3.4%.

6.1.4 Efficiency

Monte Carlo Statistics The systematic uncertainties due to Monte Carlo statistics were calculated from the first row of Table 15 and amount to 1.2%, 1.3%, 3.7% and 1.1% for the D^0, D^+, D_s^+ and D^{*+}, respectively.

Track reconstruction efficiency The track reconstruction efficiency was tested separately for VDS and OTR using $K_s^0 \to \pi^+\pi^-$ decays. One of the pions was reconstructed from VDS (or OTR) and ECAL informations only. Applying the same procedure to Monte Carlo data, we obtained an uncertainty of the track reconstruction efficiency of 1.5% per track. The systematic uncertainties are 3% for D^0 and 4.5% for D^+, D_s^+ and D^{*+}.

Particle identification Particle identification efficiencies were tested by using the reconstructed decays of K_s^0, ϕ and $\Lambda(\bar{\Lambda})$ as sources of pions, kaons and protons. The same procedure was applied on the real data and on the inelastic Monte Carlo. Only the tracks within the acceptance of the RICH were considered. The momentum dependent identification efficiencies are shown in Fig 34. The real data efficiencies are for about 5% lower compared to the Monte Carlo efficiencies, regardless of particle type and likelihood cuts. The same discrepancy was obtained also for protons. We investigated further this discrepancy. Larger event multiplicities on the real data are not the reason. By reweighting the Monte Carlo events to the multiplicity of real data the efficiencies decreased by only 0.5%. We attributed the lower efficiency on the real data to the angular resolutions of the track segments in the OTR, which seem to be underestimated by the Monte Carlo. Oppositely, the track segments in the VDS are well modeled by the Monte Carlo (see next paragraph).

We calculate the momentum dependent correction factors to the particle identification efficiency as the ratio of the efficiencies extracted from the real data and on the Monte Carlo simulated data, i.e. as the ratios of the histograms shown in Fig. 34. These correction factors are then used to the determine the correction factors of the reconstruction efficiency for each of the D mesons. From the momentum distributions of pions and kaons obtained from signal Monte Carlo after the analysis cuts, we calculated the average correction factors for pions and kaons from different D mesons. We obtained nearly the same value (within 0.5%) of 0.95 per

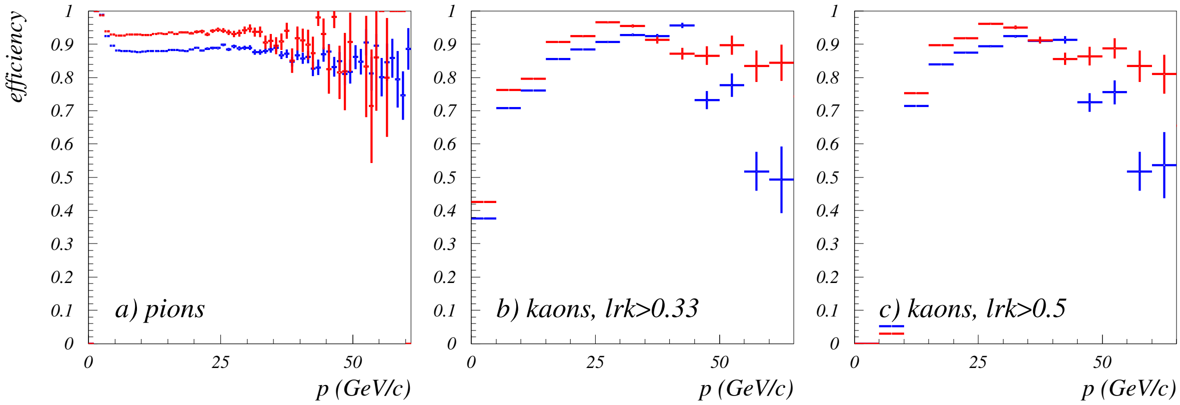

Figure 34: Comparison of the particle identification efficiencies between real data (blue) and Monte Carlo (red) for pions from K^0_s and kaons from ϕ decays.

D^0	D^+	D^+_s	D^{*+}
0.90	0.86	0.86	0.90

Table 30: Correction factors for the reconstruction efficiencies due to particle identification efficiency mismatch.

identified particle. We correct the D meson reconstruction efficiencies by using the above factor and assign a systematic uncertainty of 2% per identified particle. The correction factors are summarized in Table 30.

Analysis cuts The stability of analysis cuts is discussed in Appendix A. By the determination of cross sections in a relatively wide range around the optimal cuts we obtained the cross section variations of 9%, 5%, 11% and 17% for the D^0, D^+, D^+_s and D^{*+}, respectively. These variations when compared to the statistical errors of 10%, 11%, 34% and 22% are all smaller. Since the data samples at different cuts are not the same, the variations include statistical fluctuations as well. In such case it is not easy to disentangle statistical fluctuations from possible systematic effects. We decided not to use the above numbers for the estimation of systematic uncertainties.

Since the analysis cuts were performed on the significances, the two quantities have to be well reproduced with the Monte Carlo: the track resolutions, when extrapolated to the targets and the estimated track errors given by a covariance matrix. We studied both on samples of 100k pion candidates each and from several runs. The pion candidates were selected with the same criteria as used for the analysis. Both quantities were compared to the inelastic Monte Carlo (runs 09_302 and 09_304).

The track resolutions were studied on the basis of their impact parameters with respect to the reconstructed wire. Deviations of several percents were observed. The largest are for the

VDS	20199 (C)	20653 (C)	20768 (C)	20341 (W)	20680 (W)	average	smeared
1	0.97	0.99	0.95	1.07	0.98	0.99	1.05
2	1.05	1.03	1.09	1.05	1.09	1.06	1.04
3	1.03	1.05	1.05	1.04	1.04	1.04	1.03
4	0.99	1.00	1.00	0.98	0.98	0.99	1.05
5	1.01	1.01	1.00	1.02	1.01	1.01	1.04
6	1.02	1.00	1.02	1.01	1.03	1.02	1.04

Table 31: Ratio between DATA and MC of impact parameters to the reconstructed wire, the average and the effect of smearing the parameters tx and ty by 10%. The last column refers to the ratio of smeared and original Monte Carlo.

tracks starting at the VDS superlayers 2 and 3 (Table 31). Similar deviations for superlayers 2 and 3 were obtained, if we smeared the track parameters tx and ty on Monte Carlo by 10% of the corresponding covariance matrix element [††]. We estimate, that the Monte Carlo describes the track resolutions to a better than 10% accuracy.

By smearing the tracks in the signal Monte Carlo by 10% and by comparing the efficiencies of un-smeared and smeared Monte Carlo, we estimated this contribution to the systematic uncertainty of the cross section to 2.8% for the D^0, 2.2% for the D^+, 4.4% for D_s^+ and 2.6% for D^{*+}.

The estimated track errors were studied on the basis of their impact parameter errors, calculated from the covariance matrices of the track and of the primary vertex. The distributions from inelastic Monte Carlo were compared to the distributions from real data for each VDS super-layer and in 10 inverse momentum bins in the range 0 - 0.5 (GeV/c)$^{-1}$. A very good agreement was found. The mean of the distributions deviated by less than 1%. The systematic uncertainty of the cross sections was estimated by changing the values of all significances (d, b, b_m) on which we cut by $\pm 1\%$ and taking for the error the half of the difference in resulting reconstruction efficiency. The contributions to the systematic uncertainties are 1.6%, 1.6%, 2.0% and 0.1% for the D^0, D^+, D_s^+ and D^{*+}, respectively.

We studied also the impact of the event multiplicity. With the old Monte Carlo, where the multiplicities were considerably lower (40% for the hits in RICH and 15% for the number of long tracks) the efficiencies were higher by about 1%. With the new Monte Carlo, which was used for this analysis, the event multiplicities agree with the ones observed on the real data much better (see Appendix B), thus we consider this contribution to be negligible.

The total systematic uncertainty of cross sections arising from analysis cuts is estimated to be 3.2%, 2.7%, 4.8% and 2.6% for the D^0, D^+, D_s^+ and D^{*+}, respectively.

[††] A gaussian random number with sigma equal to 46% of the covariance matrix element was added.

Source	D^0	D^+	D_s^+	D^{*+}
Monte Carlo statistics	1.2%	1.3%	3.7%	1.1%
Track reconstruction	3.0%	4.5%	4.5%	4.5%
Particle identification	4.0%	6.0%	6.0%	4.0%
Analysis cuts	3.2%	2.7%	4.8%	2.6%
Re-weighting	2.9%	3.6%	7.7%	4.6%
Total	6.7%	8.8%	12.3%	8.1%

Table 32: Summary of systematic uncertainties of reconstruction efficiency.

Source	D^0	D^+	D_s^+	D^{*+}
Event counting	3.4%	2.6%	6.0%	9.7%
Branching fractions	1.8%	3.6%	13%	1.9%
Luminosity	3.4%	3.4%	3.4%	3.4%
Efficiency	6.7%	8.8%	12.3%	8.1%
Total	8%	11%	19%	13%

Table 33: Summary of systematic uncertainties of visible cross sections

Reweighting of kinematical distributions The systematic uncertainties due to re-weighting of kinematical distributions were estimated in section 5.6 by varying the parameter values according to their errors. The results are given in Table 28. The uncertainties were estimated to be 2.9%, 3.6%, 7.7% and 4.6% for the D^0, D^+, D_s^+ and D^{*+}, respectively.

6.1.5 Summary of systematic uncertainties

The systematic uncertainties of the reconstruction efficiencies are summarized in Table 32 and the uncertainties of visible cross sections in Table 33. The systematic uncertainties of visible production cross sections are estimated to be 8%, 11%, 19% and 13% for the D^0, D^+, D_s^+ and D^{*+}, respectively.

6.2 Cross section ratios

To the systematic errors of the cross-section ratios the following effects contribute: uncertainties in event counting and branching ratios, the error due to the finite Monte Carlo statistics and systematic errors from the analysis (track reconstruction, particle identification, analysis cuts and re-weighting), while the error in luminosity cancels. The errors due to the uncertainties in the track reconstruction and particle identification efficiencies cancel only partially because of the different number of particles in the final state. We note that in case of the ratio D^{*+}/D^0 there is no contribution from particle identification because we applied no identification requirements

Source	D^+/D^0	D^{*+}/D^0	$D_s^+/(D^0+D^+)$
Event counting	4.3%	10.0%	6.3%
Branching ratio	4.0%	0.5%	13%
Monte Carlo statistics	1.8%	1.6%	3.7%
Track reconstruction	1.5%	1.5%	1.0%
Particle identification	2.0%	0.0%	1.4%
Analysis cuts	0.6%	1.4%	1.7%
Re-weighting	1.0%	2.0%	4.5%
Total	6%	11%	16%

Table 34: Summary of systematic uncertainties of cross section ratios.

for the slow pion in the decay of the D^{*+}. The uncertainty in track reconstruction and particle identification efficiency for the ratio $D_s^+/(D^0+D^+)$ was estimated with a toy Monte Carlo.

The effect of the analysis cuts was determined in a similar way as for the cross sections (see section 6.1.4 for details) by calculating the ratio of efficiencies with the smeared Monte Carlo to the ratio determined with original efficiencies. The effect of the uncertainty in the covariance matrix was estimated by a simultaneous $\pm 1\%$ variation of all significances on which we cut. In the same way the effect of the re-weighting of the kinematical distributions was evaluated by changing the re-weighting factors by $\pm 1\sigma$.

The resulting contributions are summarized in Table 34, and amount in total to 6%, 11% and 16% for the cross section ratios for D^+/D^0, D^{*+}/D^0 and $D_s^+/(D^0+D^+)$, respectively.

6.3 A-dependence parameter α

Only two sources contribute to the measurement of the A-dependence parameter α, the luminosity per wire and the Monte Carlo statistics in the calculation of the efficiency. For the calculation of this systematic error the cross section per nucleus was calculated with a toy Monte Carlo, using Eq. 10. To estimate the contribution of the error on α, the efficency for each target was smeared with the statistical errors given in Table 15. The resulting cross sections per nucleus for the three target materials was then fitted with Eq. 11 to get the value of the parameter α for each meson. A weighted average was calculated for the four values to get the common value of α.

This procedure was repeated 10000 times. The values for the parameter α of those fits was then fitted with a gaussian. The standard deviation of the gaussian was taken as the contribution to the systematic error on α. The same procedure was repeated also by smearing the luminosities of the targets by their errors given in chapter 6.1.3. The contributions to the systematic error on α are summarized in Table 35

Source	D^0	D^+	D^{*+}	D_s^+	total
Monte Carlo Statistics	1.0%	1.1%	0.8%	3.3%	0.6%
Luminosity	2.5%	2.5%	2.5%	2.7%	2.5%
Total	2.7%	2.7%	2.6%	4.2%	2.6%

Table 35: Summary of the systematic uncertainties for the A-dependence parameter α

6.4 Leading to non-leading particle asymmetries

The only contribution to the systematic uncertainty comes from Monte Carlo statistic. From the definition of leading to non-leading particle asymmetry with Eq. 18 we calculated the error by standard error propagation method. The absolute systematic uncertainties of the asymmetries are 0.01, 0.01, 0.01 and 0.04 for the D^0, D^+, D^{*+} and D_s^+, respectively.

7 Results

7.1 Corrected cross sections

By using the correction factors from the re-weighting of the kinematical distributions (Sec. 5.6) in Monte Carlo and for the efficiency of the RICH (Sec. 6.1.4) we can derive the final values of the cross sections. The two correction factors are extracted from Table 28 and Table 30, and their products, the final correction factors, are listed in Table 36.

D^0	D^+	D_s^+	D^{*+}
0.98	0.97	1.02	1.07

Table 36: Final correction factors for the reconstruction efficiencies.

From the cross sections from Table 17 the final cross sections in our visible range are calculated by dividing these values with the correction factors. The cross sections (in μb/N) are: 26.8±2.6±2.1, 11.0±1.1±1.2, 10.4±3.6±2.0 and 12.1±2.6±1.6 for the D^0, D^+, D_s^+ and D^{*+}, respectively. The extrapolation to the full x_F range was calculated using the factor $f_{vis} = 0.55 \pm 0.05$ from Eq. 42. The error on the factor was added to the systematic errors from Table 33. The corresponding total cross sections (in μb/N) are: 48.7±4.7±5.9, 20.0±2.0±2.9, 18.9±6.5±4.0 and 22.0±4.7±3.5. The results are summarized in Table 37.

These results can be compared to previous experimental studies. Figure 35 shows the comparisons for all the four D-mesons. The fit has been performed with the formula given in Eq. 1. All our results agree well: D^0 and D^{*+} are within one standard deviation, D^+ is 1.8 standard deviations below the value from the fit. The measured cross section for D_s^+ production is in good agreement with the 90% confidence level limit published by the experiment E769, and also with the unpublished measured point from the same experiment (PhD thesis [11])[‡‡].

[‡‡]To compare the D_s^+-results we scaled the E769 cross sections with the factor $\frac{1.72}{2.16}$ to account for the different branching fraction of the decay $D_s^+ \to \phi\pi^+$ used by E769

$\sigma[\mu b/N]$				
	D^0	D^+	D_s^+	D^{*+}
visible range	26.8±2.6±2.1	11.0±1.1±1.2	10.4±3.6±2.0	12.1±2.6±1.6
full x_F	48.7±4.7±5.9	20.0±2.0±2.9	18.9±6.5±4.0	22.0±4.7±3.5

Table 37: Cross sections in the visible x_F range and extrapolated to full phase space

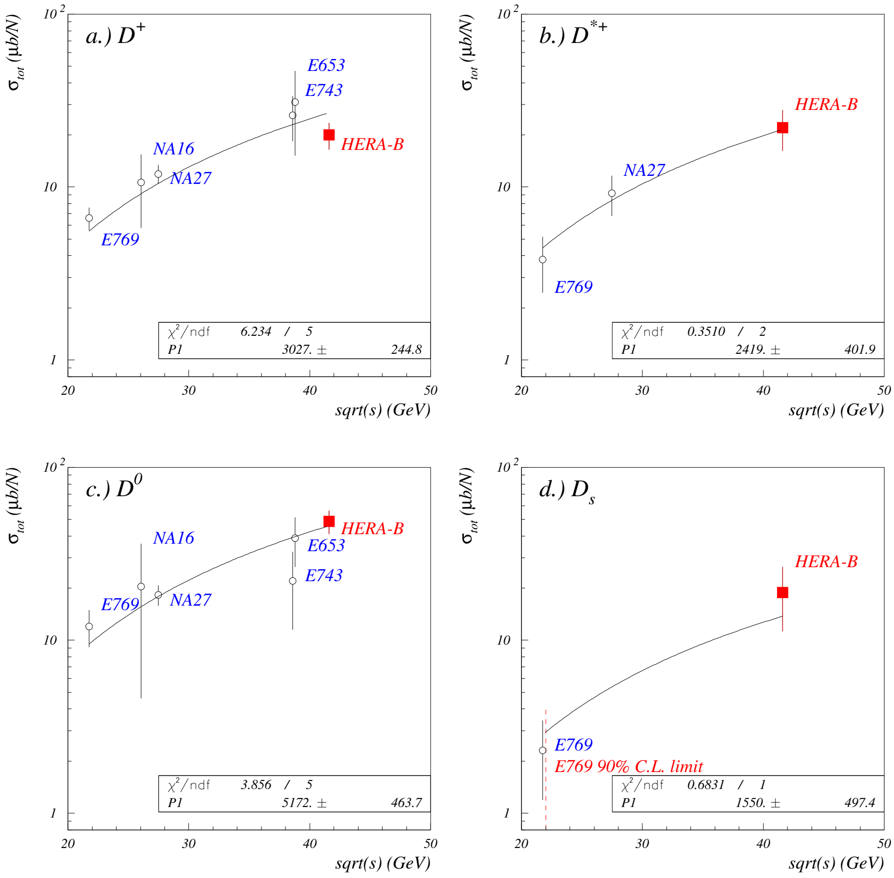

Figure 35: Comparison of the results with previous experiments.

7.2 Cross section ratios

The ratio $\sigma(D^+)/\sigma(D^0)$ can be predicted by a simple model. From the isospin invariance we expect the same number of generated charged and neutral D-mesons. Because of the three different polarization states for vector mesons we expect three times more vector D-mesons than scalar D-mesons. Taking into account, that the charged vector meson D^{*+} decays with the probability of about 1/3 into $D^+\pi^0$ and with about 2/3 into $D^0\pi^+$, while the neutral vector meson D^{*0} always decays into D^0 and a light particle, one can calculate the ratio $\sigma(D^+)/\sigma(D^0) = 1/3$. In a similar way the prediction $\sigma(D^{*+})/\sigma(D^0) = 1/2$ can be derived.

The cross section ratios calculated from the results in Table 37 are summarized in Table 38, a comparison with previous experiments is presented in Fig. 36. The value for the ratio $\sigma(D^+)/\sigma(D^0) = 0.41 \pm 0.06 \pm 0.02$ is within the errors in agreement with the average of the previous experiments. The ratio $\sigma(D^{*+})/\sigma(D^0) = 0.45 \pm 0.11 \pm 0.05$ is in good agreement with the results of E769 and NA27. Both ratios are also in agreement with the predictions of the simple isospin model. Our result for the ratio $\sigma(D_s^+)/(\sigma(D^0) + \sigma(D^+)) = 0.28 \pm 0.10 \pm 0.05$ is in agreement within one standard deviation with the predicted value of 0.20 [9] and within 1.5 standard deviations with the world average value of 0.13±0.04 of measurements in e^+e^-

D^+/D^0	D^{*+}/D^0	$D_s^+/(D^+ + D^0)$
0.41±0.06±0.02	0.45±0.11±0.05	0.28±0.10±0.05

Table 38: Cross section ratios

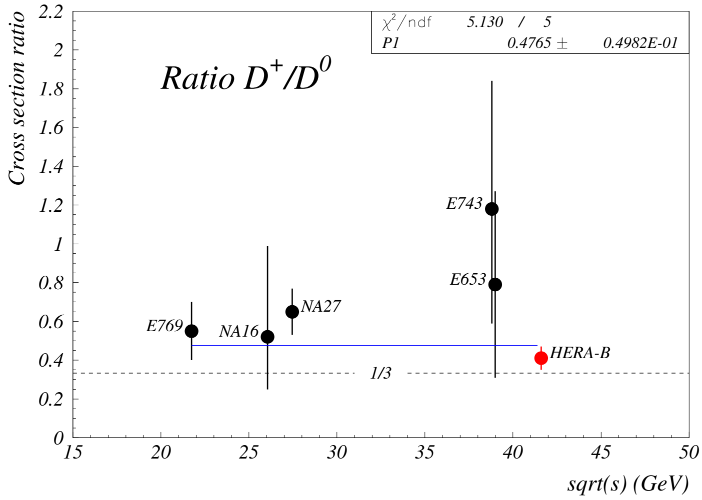

Figure 36: Comparison of the results with previous experiments.

collisions[12].

7.3 Leading to non-leading particle asymmetries

The leading to non-leading particle asymmetries are presented in Table 39 together with the predictions of PYTHIA. The PYTHIA values for all D-mesons are in good agreement with the measured results.

	D^0	D^+	D^{*+}	D_s^+
Measurement	0.10±0.09±0.01	0.25±0.10±0.01	0.24±0.18±0.01	0.20±0.33±0.04
PYTHIA	0.24	0.22	0.23	-0.06

Table 39: Leading to non-leading particle asymmetries in the range of $-0.15 < x_F < 0.05$. For the D_s^+ the anti-particle cross section was used for σ_{LP} in Eq. 18

7.4 A-dependence parameter α

The result for the A-dependence is $\alpha = 0.98 \pm 0.04 \pm 0.03$. The only previously published measurement in pA reactions is the result of E789, $\alpha = 1.02 \pm \pm 0.03 \pm 0.02$. Our value is of about the same accuracy and in good agreement with this result. It is also in agreement with the assumption of linear dependence of cross sections, $\alpha = 1$.

8 Summary

We measured the total and single differential cross sections σ, $d\sigma/dp_T^2$ and $d\sigma/dx_F$, the A-dependence of the cross sections and the leading to non-leading particle asymmetries for the production of D^0, D^+, D_s^+ and D^{*+} mesons in pA collisions at the proton energy of 920 GeV.

The total cross sections (in μb/N) are: 48.7±4.7±5.9, 20.0±2.0±2.9, 18.9±6.5±4.0 and 22.0±4.7±3.5 for the D^0, D^+, D_s^+ and D^{*+}, respectively, in good agreement with previous measurements.

The measured values for the ratio $\sigma(D^+)/\sigma(D^0) = 0.41 \pm 0.06 \pm 0.02$ and $\sigma(D^{*+})/\sigma(D^0) = 0.45 \pm 0.11 \pm 0.05$ are in agreement with the average of the previous experiments, and with the predictions of the simple isospin model. Our result for the ratio $\sigma(D_s^+)/(\sigma(D^0) + \sigma(D^+))$= 0.28±0.10±0.05 is in agreement within one standard deviation with the prediction of 0.2 [9] and within 1.5 standard deviations with the world average value of 0.13±0.04 of measurements in e^+e^- collisions [12].

The result for the A-dependence, $\alpha = 0.98 \pm 0.04 \pm 0.03$, is again in good agreement with the previous measurement, as well as with the assumption of a linear dependence of cross sections, α=1. The measured leading to non-leading particle asymmetries are in good agreement with the predictions derived from PYTHIA.

A Stability of cuts

The stability of the cuts was tested with two methods:

1. By varying one cut while the others were fixed at their optimized values
2. By calculating all combinations of cuts within a 3 dimensional (for D^+) or 4 dimensional (D^0, D^{*+} and D_s^+) matrix and keeping only those with relative significance larger than 90% of the value at optimal cuts. For D_s^+ the limit was chosen at 95% of the value at optimal cuts because of the small statistics of the signal.

The results of the first method are presented in Figs. 37a, 38a, 39a and 40a. The cuts used in the various optimizations are summarized in Table 10. For each reconstructed type of meson, each cut is presented in a separate plot, which shows the relative cross sections σ/σ_{opt} presented with circles and error bars as a function of the cut. The relative significance s/s_{opt} is shown as a dashed blue line and the relative efficiency ϵ/ϵ_{opt} as a solid red line. The horizontal dashed line shows the normalization. The cut value at the highest significance is indicated with an arrow. The cross section is calculated as the ratio of the number of reconstructed events in real data and Monte Carlo. The cross section, the efficiency and the significance are normalized to the values, where the significance is at its maximum. All stability plots show a stable behavior of the cross section. The variations do not exceed 15 %.

For the second type of stability plots, two histograms are presented per optimization, one for each D-meson type: The relative cross section σ/σ_{opt} is plotted as a function of the relative significance s/s_{opt} and the distribution of the cross sections for all cut combinations is shown, where the relative significance exceed 90%. The mean and the r.m.s. of these distributions are indicators of the systematic error on the cross section coming from the cut optimization. The results are shown in Figs. 37b, 38b, 39b, 40b and the results are summarized in Table 40. The mean value of the cross sections for D^+ and D^0 is close to the value at the optimized cuts, while for D_s^+ and D^{*+} the mean is lower for about one sigma.

	mean	r.m.s
D^0	1.00	0.09
D^+	1.02	0.05
D^{*+}	0.93	0.17
D_s^+	0.86	0.11

Table 40: The mean and the r.m.s. of the distributions of the relative cross sections calculated on a multi-dimensional matrix.

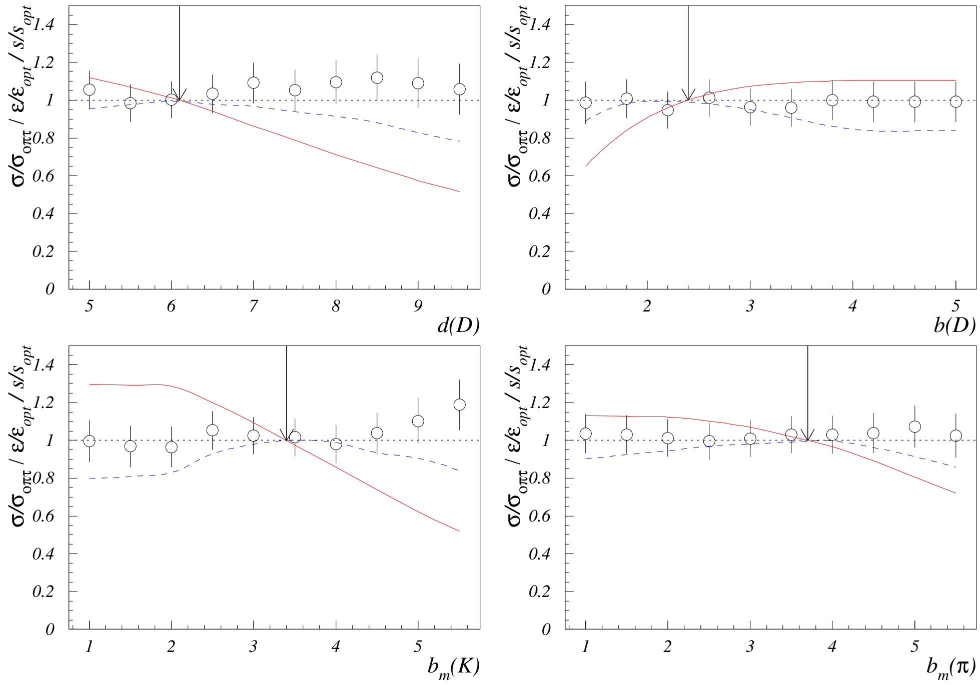

(a) With method 1

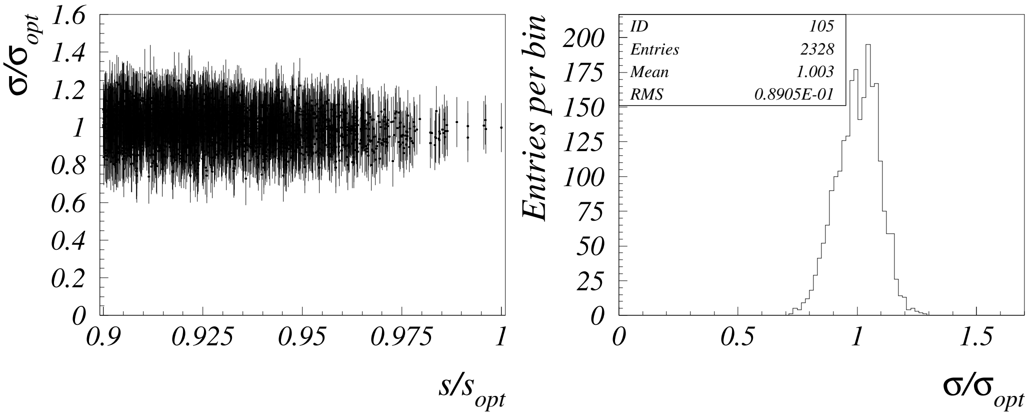

(b) With method 2

Figure 37: Stability of analysis cuts in the reconstruction of $D^0 \to K^-\pi^+$.

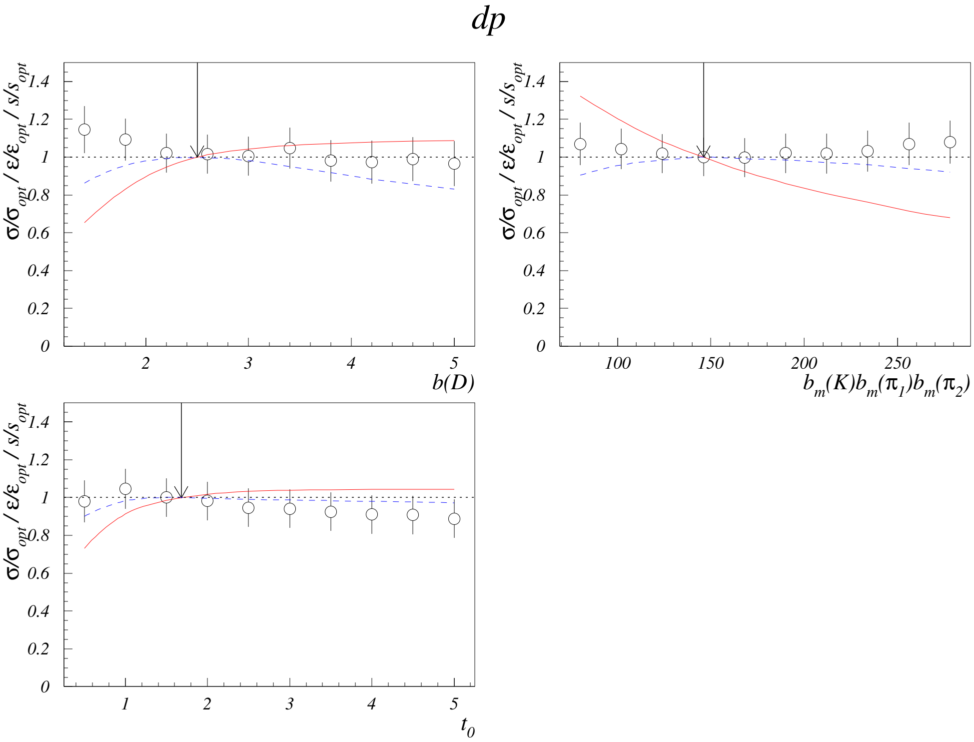

(a) With method 1

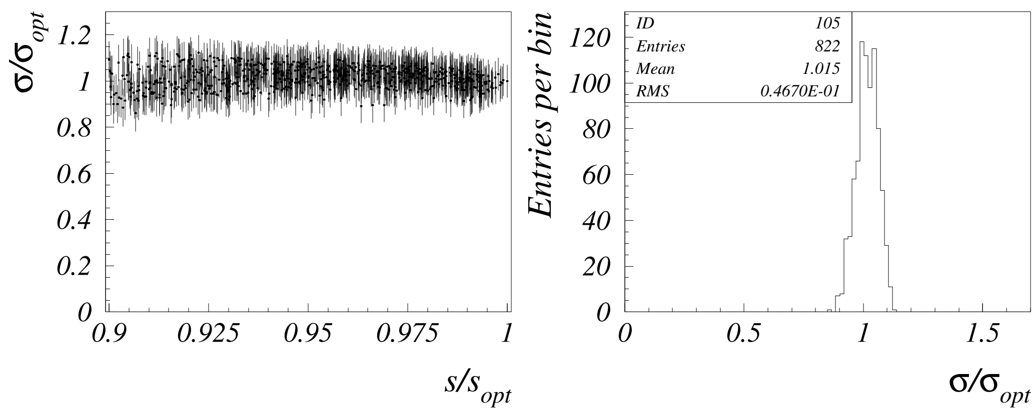

(b) With method 2

Figure 38: Stability of analysis cuts in the reconstruction of $D^+ \to K^-\pi^+\pi^+$.

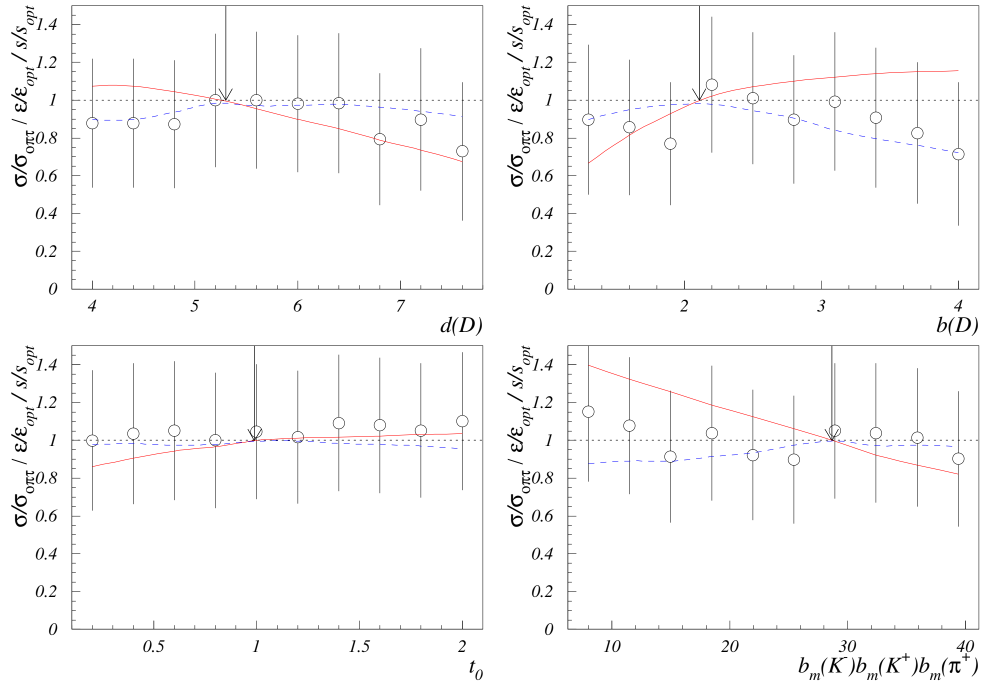

(a) With method 1

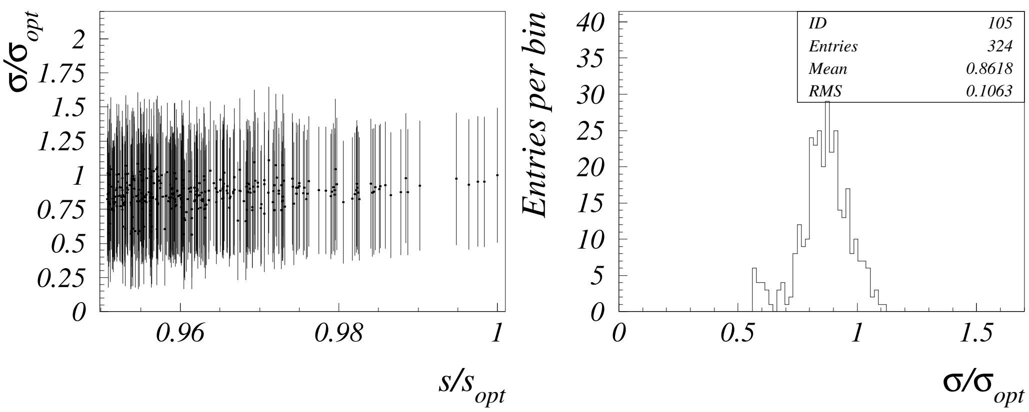

(b) With method 2

Figure 39: Stability of analysis cuts in the reconstruction of $D_s^+ \to K^-K^+\pi^+$.

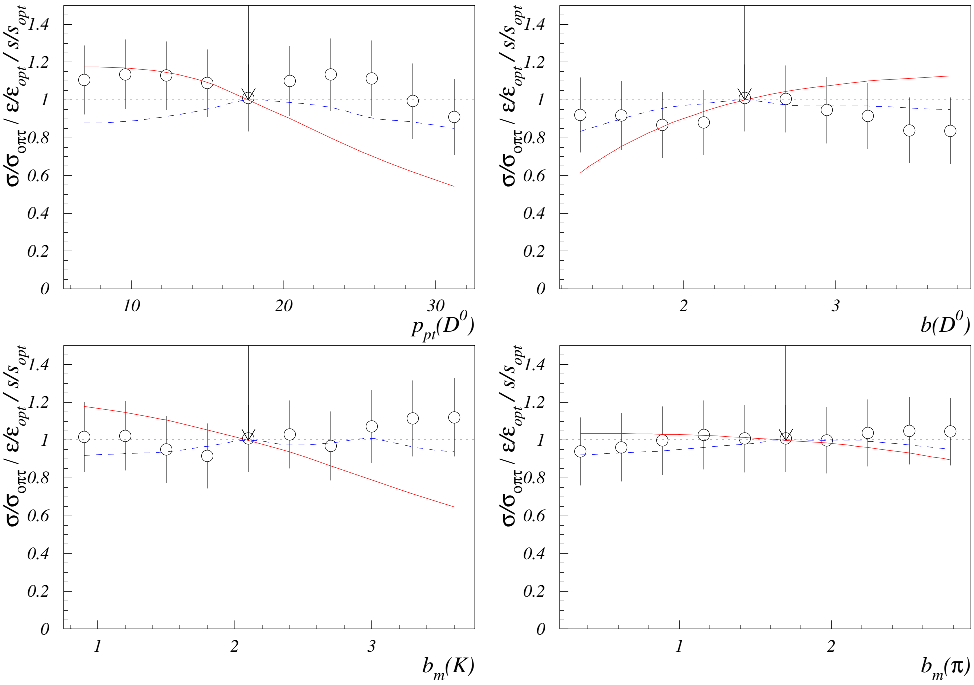

(a) With method 1

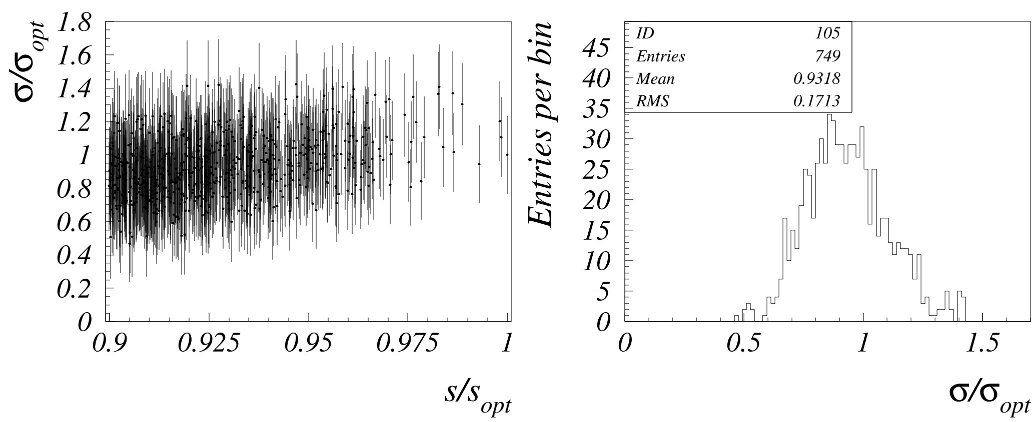

(b) With method 2

Figure 40: Stability of analysis cuts in the reconstruction of $D^{*+} \to D^0\pi \to K^-\pi^+\pi^+$.

meson	signal window [MeV]	side bands [MeV]
D^0	$\|\Delta m\| < 75$	$75 < \|\Delta m\| < 150$
D^+	$\|\Delta m\| < 50$	$50 < \|\Delta m\| < 100$
D_s^+	$\|\Delta m\| < 33$	$45 < \|\Delta m\| < 66$
D^{*+}	$\|\Delta q\| < 2.5$	

Table 41: Window sizes used in the comparison.

B Comparison between MC and data

The agreement between real data and Monte Carlo was checked by comparing the distributions of some relevant variables after the analysis cuts had been applied. To get the distribution for signal events of a given variable, two histograms were filled first: one with events from the signal window and the other one with the events from sidebands. Then the distribution for side bands was subtracted from the distribution for signal window. The window sizes are summarized in Table 41. For D^{*+} instead of sidebands the wrong sign combinations in the signal window were used.

Since the fractions of generated signal events per wire differ from that in real data, for the Monte Carlo we filled the histograms separately for each wire and then took the weighted sum, with the weights:

$$f_i = p_i/n_i \tag{43}$$

where $p_i = \frac{A_i\mathcal{L}_i}{\sum_i A_i\mathcal{L}_i}$ is the fraction of signal events in real data for i^{th} wire (assuming linear A-dependence) and $n_i = \frac{N_i}{\sum_i N_i}$ is the fraction of Monte Carlo events per wire i. The distribution from Monte Carlo was finally normalized to the same number of events as in the real data and plotted together with the real data distribution. Real data are shown with error bars and Monte Carlo with error boxes. For each distribution also the $\chi^2/n.d.f.$ was calculated and printed in each plot. It was calculated by:

$$\chi^2 = \sum_i \frac{(n_i^{DATA} - n_i^{MC})^2}{\sigma_i^2} \tag{44}$$

where n_i is the i^{th} bin content and σ_i the error for real data bins.

The following distributions have been checked:

- Event multiplicities (Fig. 41)
- Momentum (Figs. 42, 43 and 44)
- Transverse momentum (Figs. 45 and 46)

- Impact parameter significance of kaons and pions (Figs. 47 and 48)
- Product of cuts (Fig. 49)
- Impact parameter significances of D-mesons (Fig. 50)
- Distance significances (Fig. 51)

For all distributions a good agreement between the real data and Monte Carlo has been found.

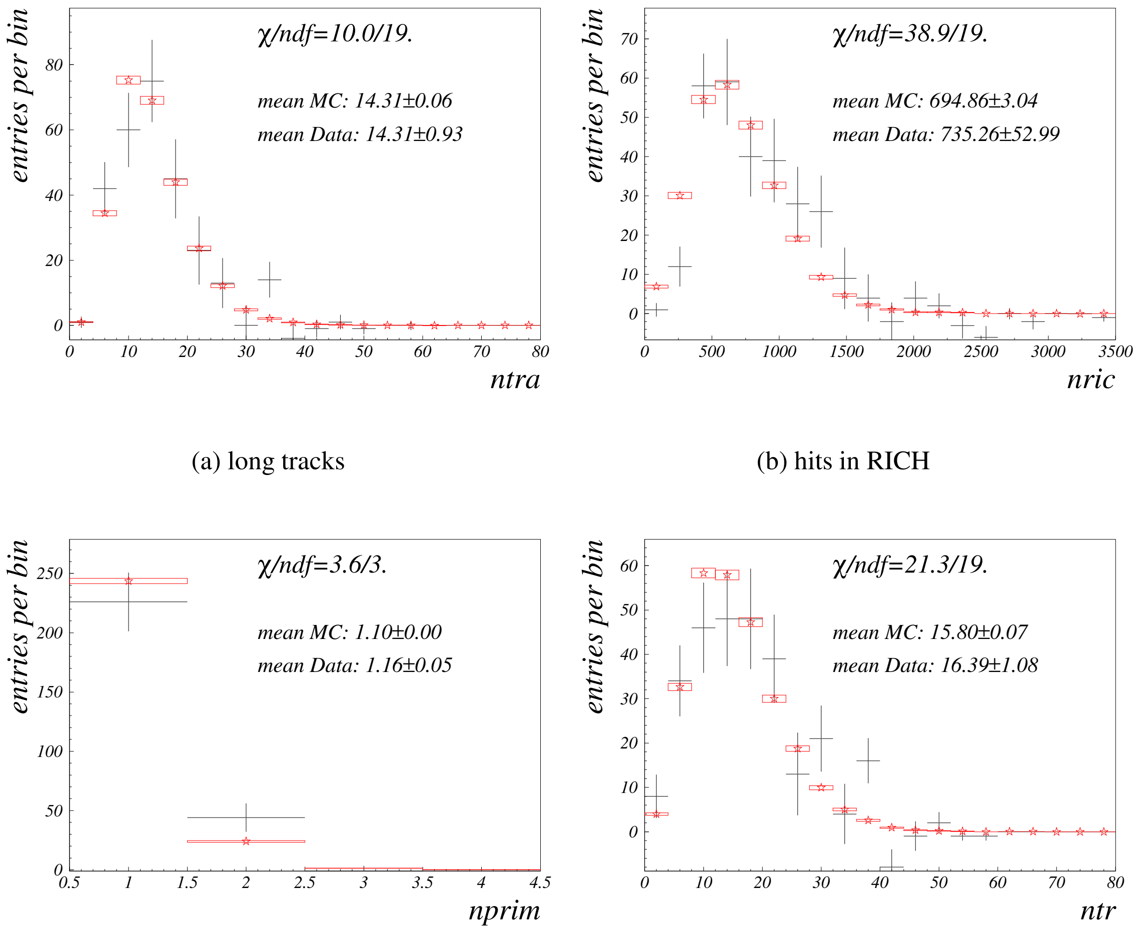

(a) long tracks

(b) hits in RICH

(c) number of primaries

(d) tracks per primary

Figure 41: Comparison of event multiplicities.

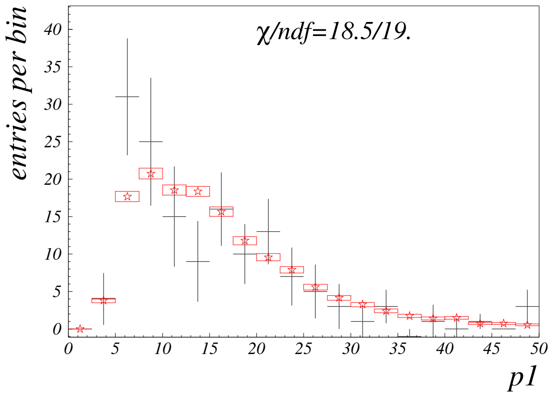

(a) D^+

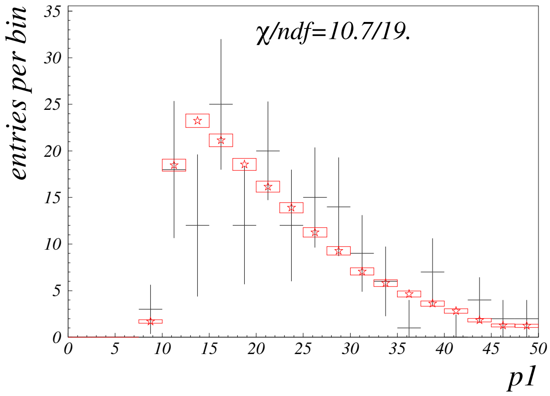

(b) D^0

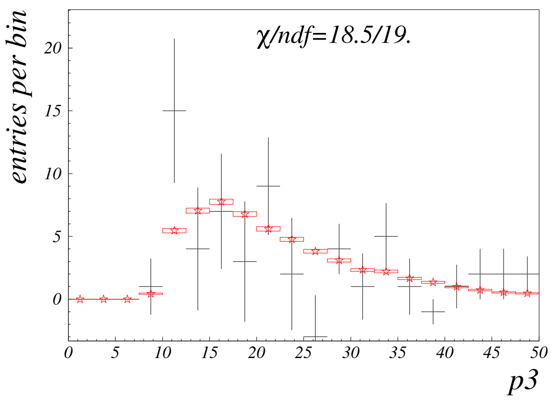

(c) D^{*+}

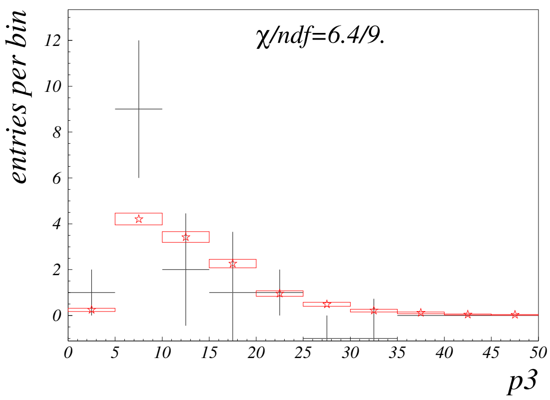

(d) D_s^+

Figure 42: Comparison of momentum distributions of kaons.

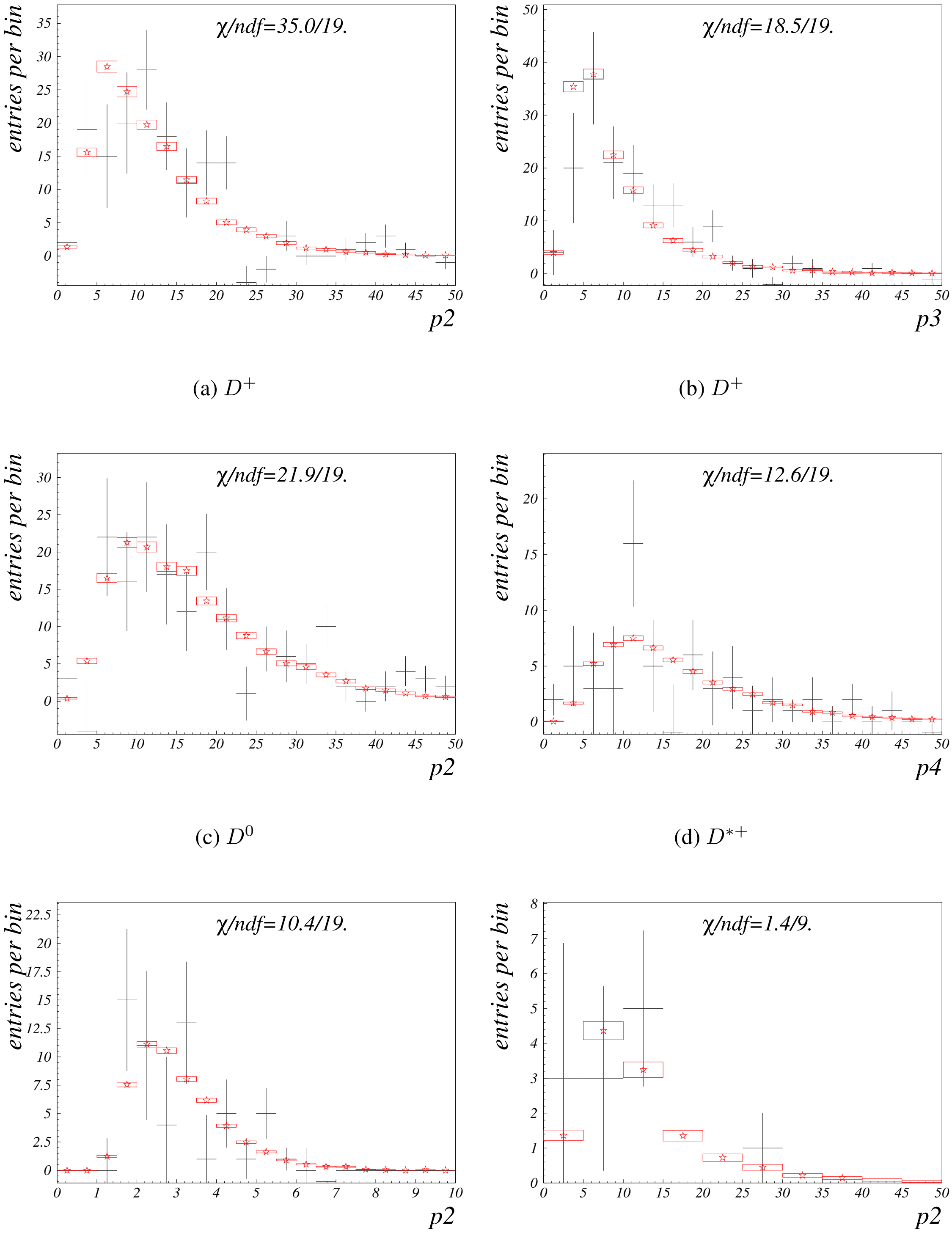

(a) D^+ (b) D^+

(c) D^0 (d) D^{*+}

(e) $D^{*+}\ \pi_{slow}$ (f) D_s^+

Figure 43: Comparison of momentum distributions of pions.

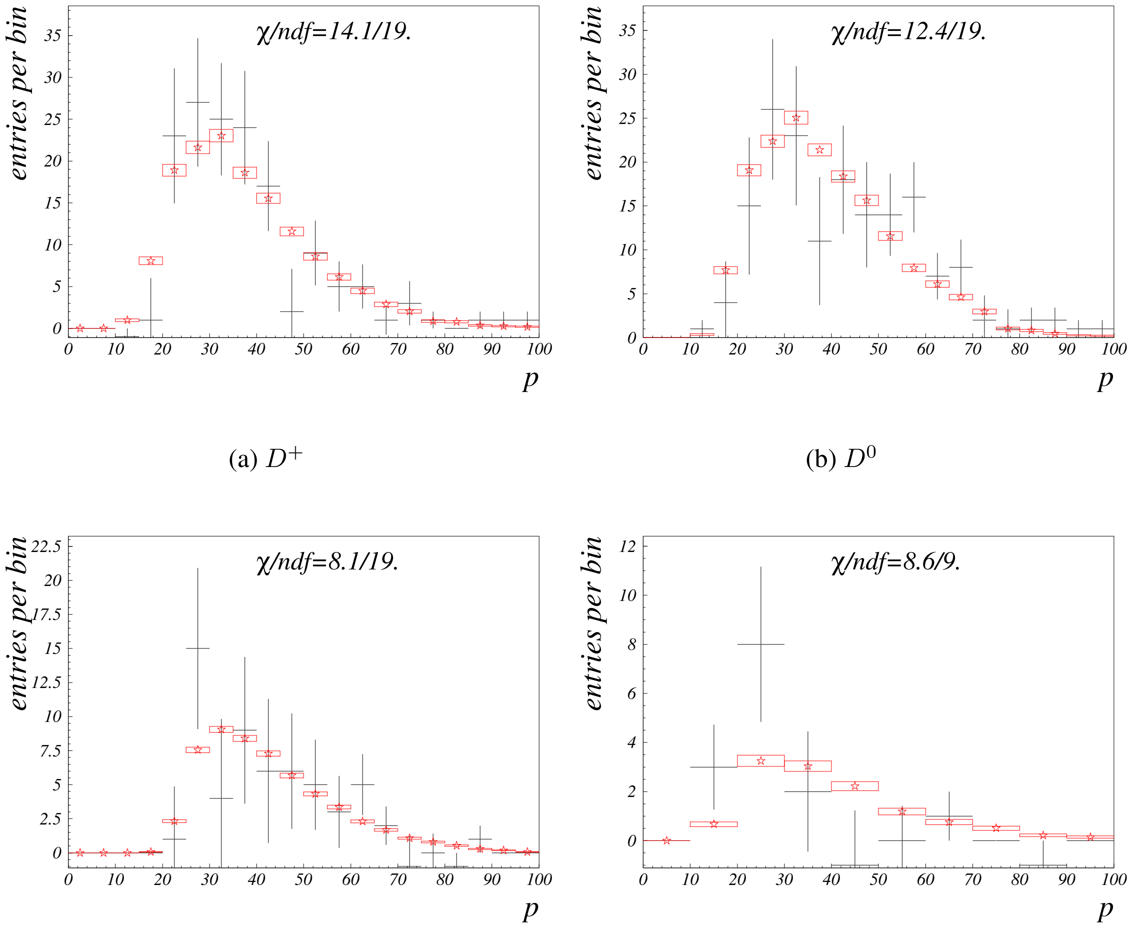

(a) D^+

(b) D^0

(c) D^{*+}

(d) D_s^+

Figure 44: Comparison of momentum distributions of D-mesons.

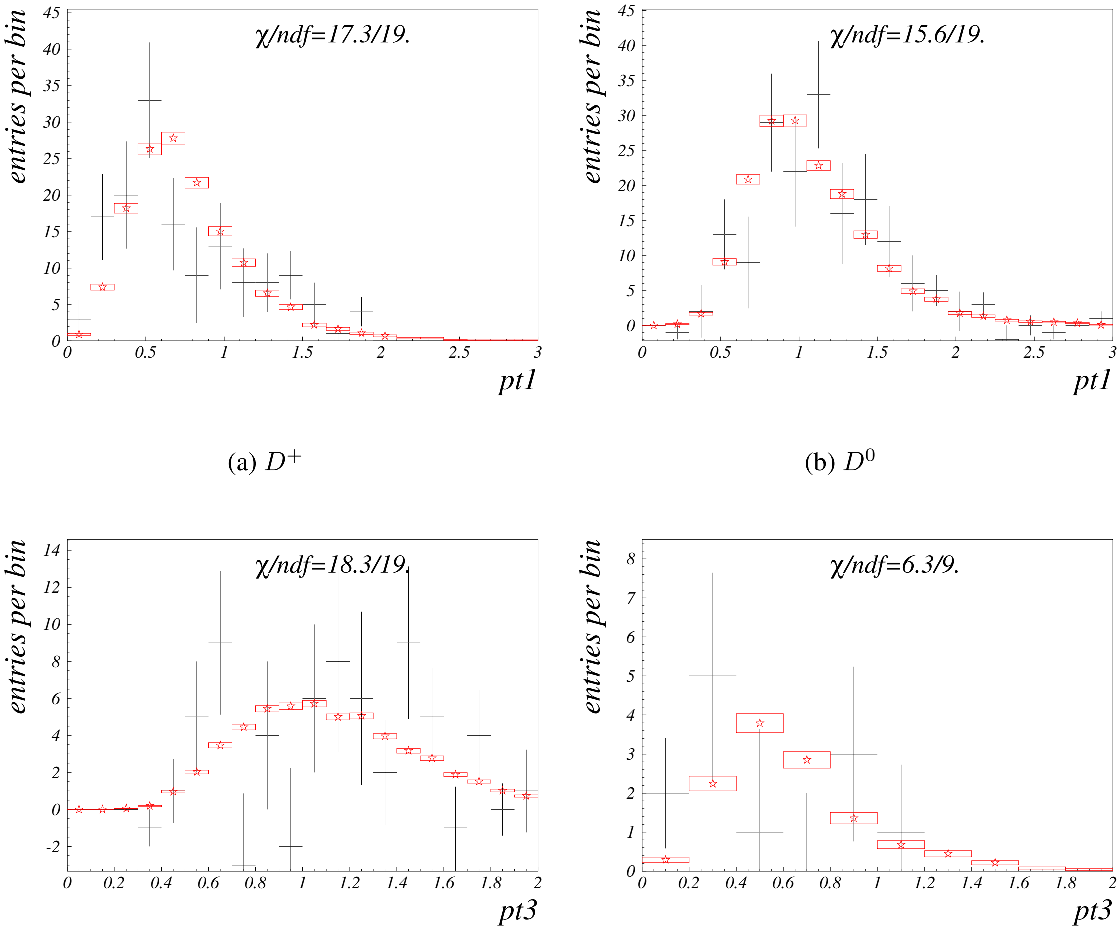

(a) D^+ (b) D^0

(c) D^{*+} (d) D_s^+

Figure 45: Comparison of transversal momentum distributions of kaons.

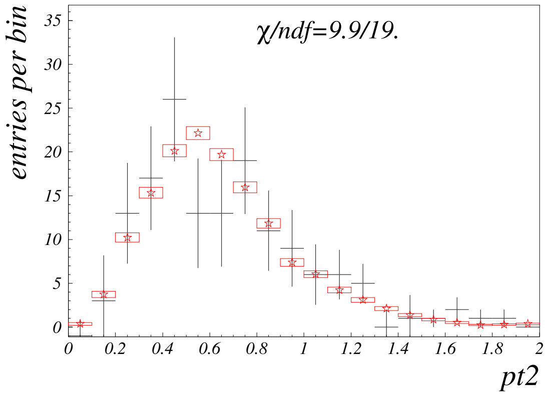

(a) D^+ π_1

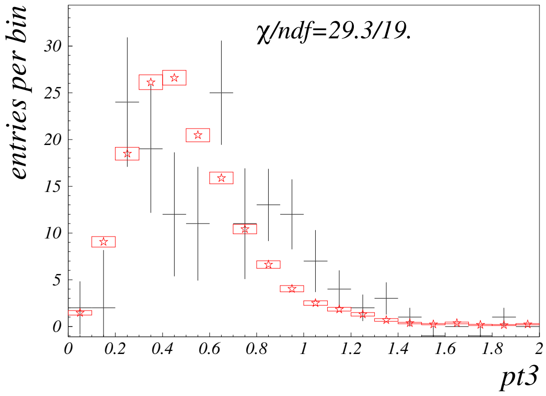

(b) D^+ π_2

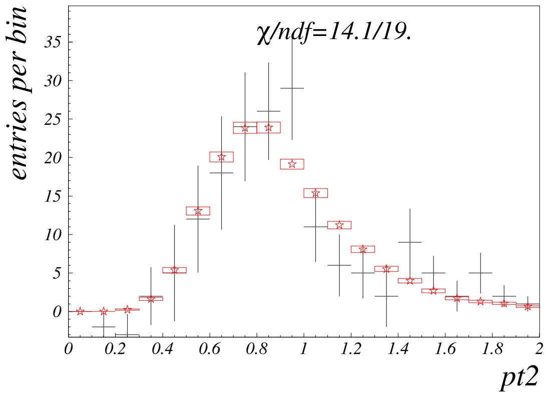

(c) D^0

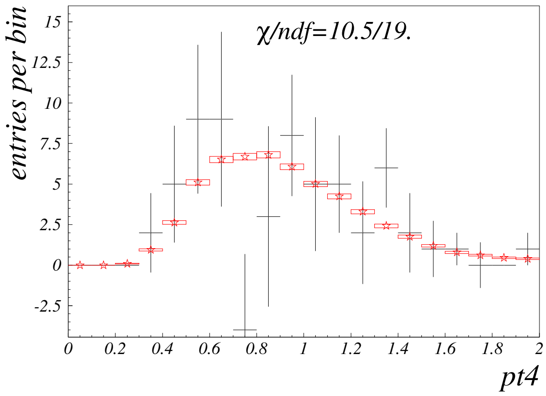

(d) D^{*+}

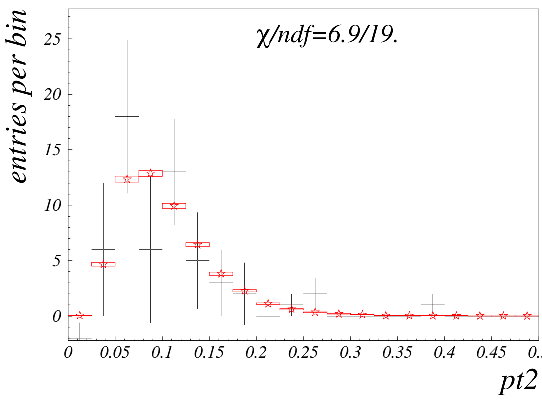

(e) D^{*+} π_{slow}

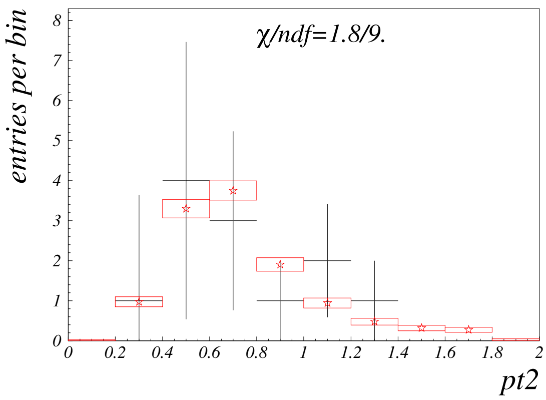

(f) D_s^+

Figure 46: Comparison of transversal momentum distributions of pions.

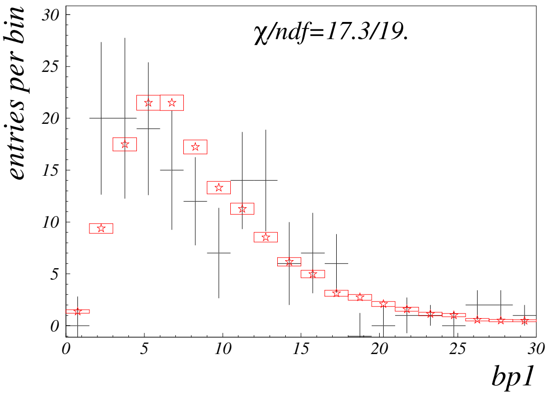

(a) D^+

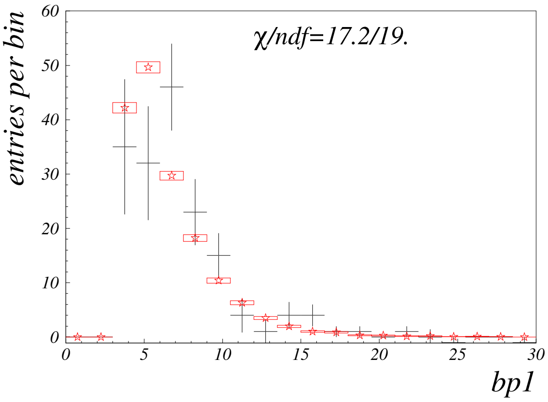

(b) D^0

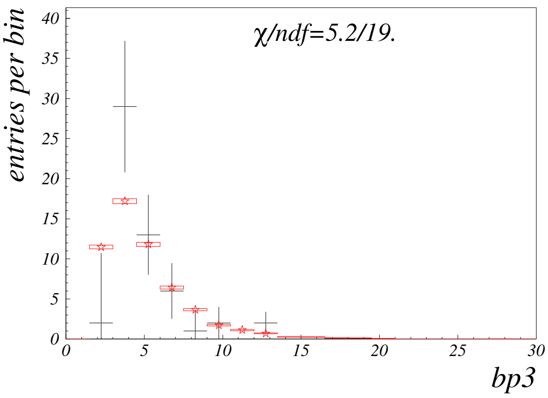

(c) D^{*+}

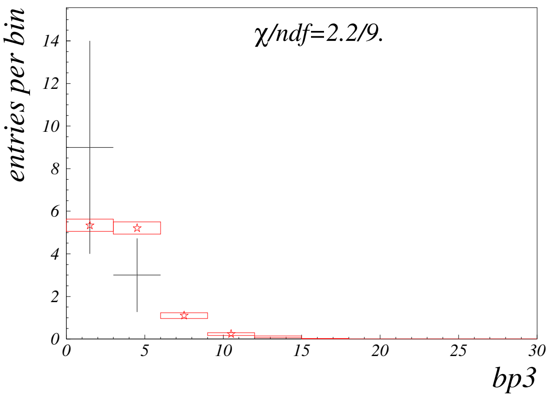

(d) D_s^+

Figure 47: Comparison of impact parameter significance distributions of kaons.

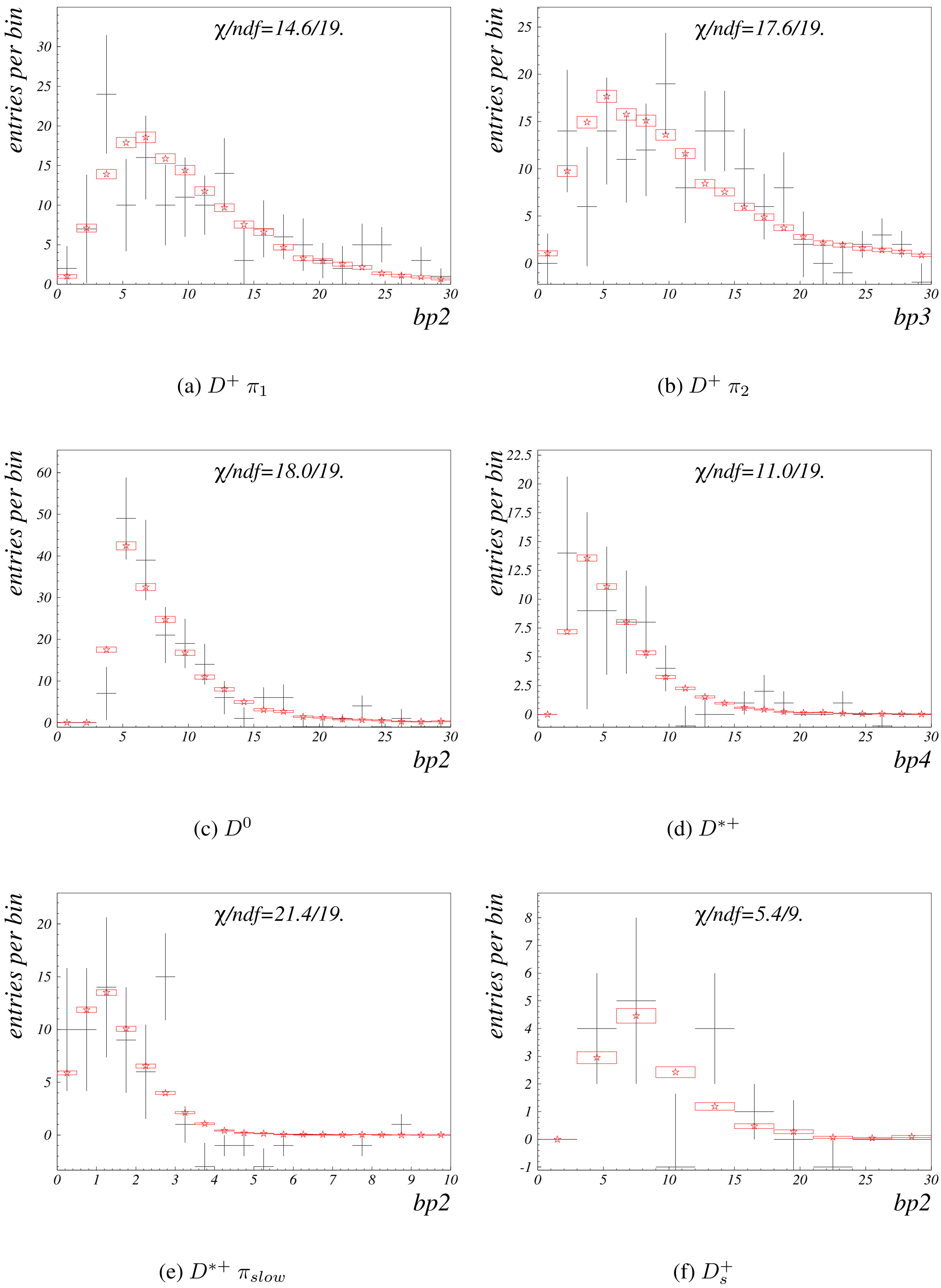

(a) D^+ π_1

(b) D^+ π_2

(c) D^0

(d) D^{*+}

(e) D^{*+} π_{slow}

(f) D_s^+

Figure 48: Comparison of impact parameter significance distributions of pions.

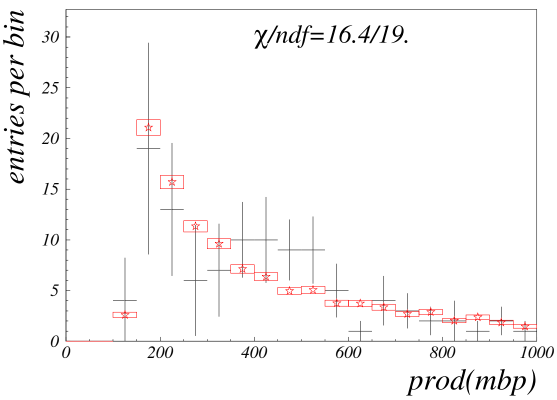

(a) D^+ prod(mbp)

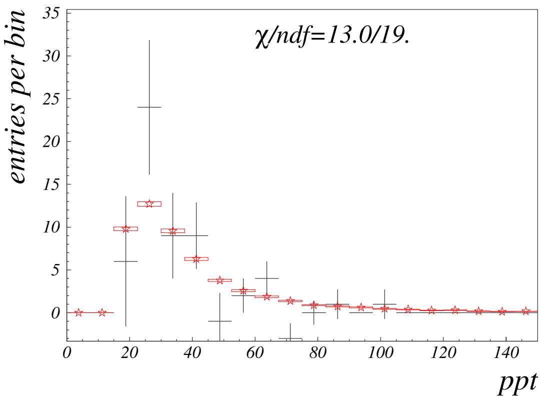

(b) D^{*+} ppt

Figure 49: Comparison of product of impact parameter significances (a) and momentum dependent p_T-cut (b).

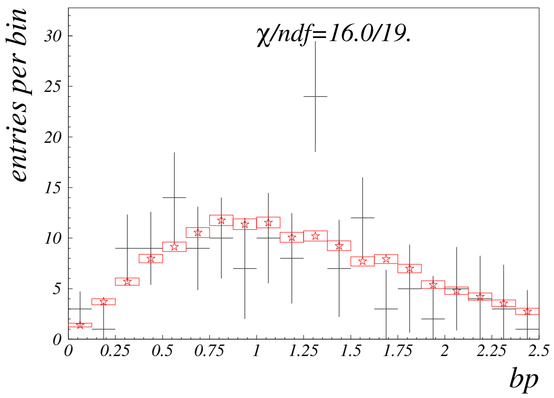

(a) D^+

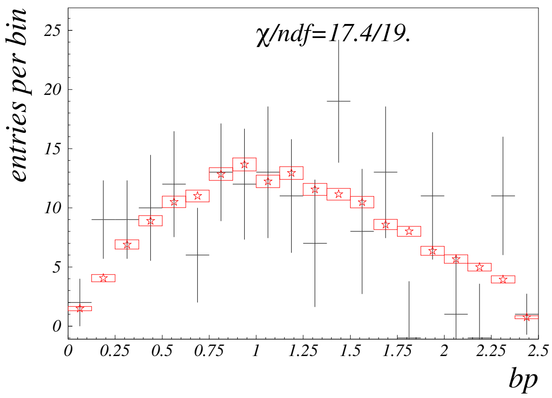

(b) D^0

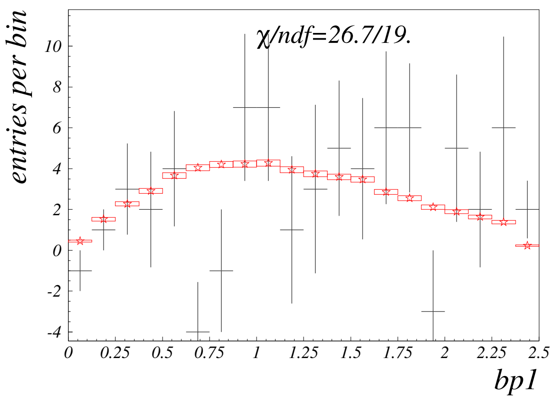

(c) D^0 from D^{*+}

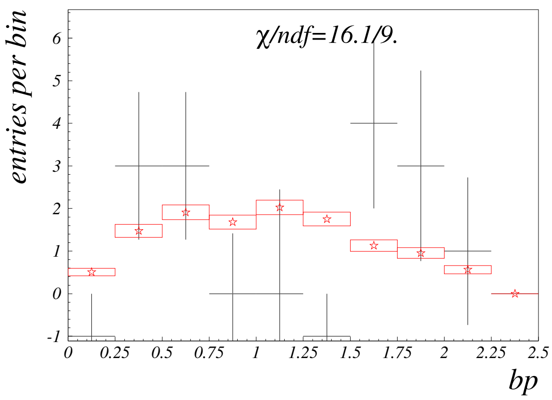

(d) D_s^+

Figure 50: Comparison of impact parameter significance distributions of D mesons.

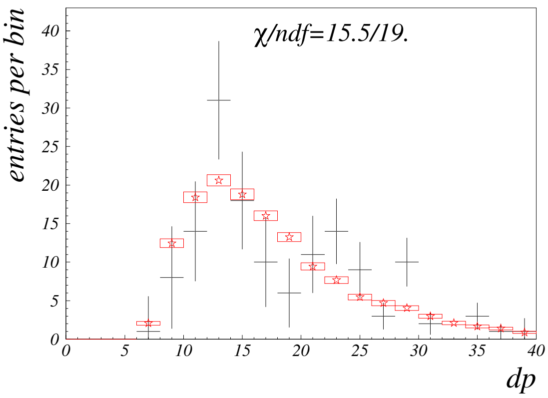

(a) D^+

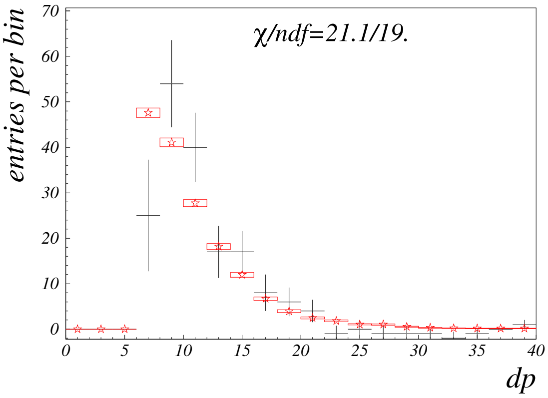

(b) D^0

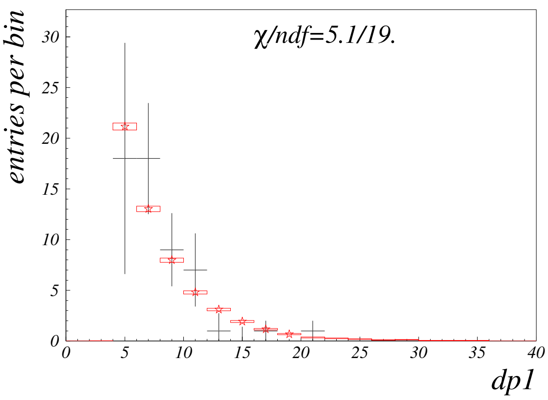

(c) D^0 from D^{*+}

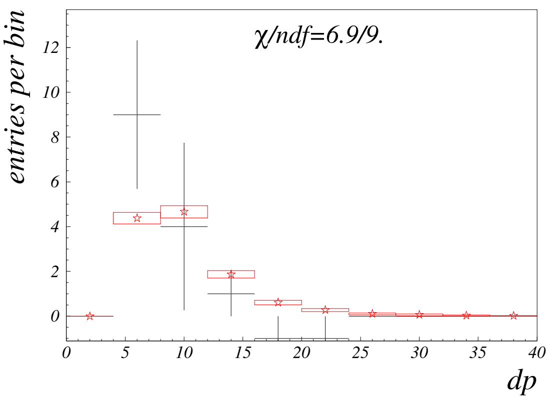

(d) D_s^+

Figure 51: Comparison of distance significance distributions of D mesons.

References

[1] C. Lourenco, H. Woehri, CERN-EP/2003-xxx, januar 2003.

[2] M. Aguilar-Benitez *et al.* [LEBC-EHS Collaboration], Phys. Lett. B **135**, 237 (1984).

[3] M. Aguilar-Benitez *et al.* [LEBC-EHS Collaboration], Z. Phys. C **40**, 321 (1988).

[4] R. Ammar *et al.*, Phys. Rev. Lett. **61**, 2185 (1988).

[5] K. Kodama *et al.* [Fermilab E653 Collaboration], Phys. Lett. B **263**, 573 (1991).

[6] G. A. Alves *et al.* [E769 Collaboration], Phys. Rev. Lett. **77**, 2388 (1996) [Erratum-ibid. **81**, 1537 (1998)].

[7] M. J. Leitch *et al.* [E789 Collaboration],

[8] M. Starič "How to combine different wires", Hera B Week Jan. 2005, Oral presentation

[9] A. Frixione, Heavy Quark Production, hep-ph/9702287, Sep 1997

[10] E. M. Aitala *et al.* [E791 Collaboration], Phys. Lett. B **462**, 225 (1999) [arXiv:hep-ex/9906034].

[11] A. F. Wallace, FERMILAB-THESIS-1997-29

[12] L. Gladilin, "Charm Hadron Production Fractions", hep-ex/9912064, Dez 1999